A NEW MACRO-SCALE HYDROLOGIC PROCESSES SIMULATOR FOR DEPRESSION-DOMINATED COLD CLIMATE REGIONS

A Dissertation
Submitted to the Graduate Faculty
of the
North Dakota State University
of Agriculture and Applied Science

By

Mohsen Tahmasebi Nasab

In Partial Fulfillment of the Requirements
for the Degree of
DOCTOR OF PHILOSOPHY

Major Department:
Civil and Environmental Engineering

July 2019

Fargo, North Dakota

North Dakota State University
Graduate School

Title

A NEW MACRO-SCALE HYDROLOGIC PROCESSES SIMULATOR FOR DEPRESSION-DOMINATED COLD CLIMATE REGIONS

By

Mohsen Tahmasebi Nasab

The Supervisory Committee certifies that this ***disquisition*** complies with North Dakota State University's regulations and meets the accepted standards for the degree of

DOCTOR OF PHILOSOPHY

SUPERVISORY COMMITTEE:

Dr. Xuefeng Chu
Chair

Dr. G. Padmanabhan

Dr. Zhulu Lin

Dr. Stephanie Day

Approved:

July 22, 2019
Date

Dr. David Steward
Department Chair

ABSTRACT

The primary objectives of this dissertation research are to (1) improve the understanding of macro-scale hydrologic processes in cold climate regions, (2) improve macro-scale representation and modeling of depression-dominated areas, and (3) improve land use variations in macro-scale hydrologic models. To achieve the objectives, (1) a Macro-Scale Hydrologic Processes Simulator (Macro-HyProS) is developed and tested in the Red River of the North Basin (RRB), (2) the impacts of sub-daily temperature fluctuations around the freezing temperature on snowmelt simulations are evaluated by using a hybrid temperature index method (HTIM), and (3) the effects of two high-resolution gridded temperature datasets on magnitude and distribution of snowmelt are assessed in the Missouri River Basin (MRB). Macro-HyProS is a grid-based daily hydrologic model that uses a unique LEGO-fashion horizontal layout to account for the within-grid heterogeneity of land use. The model incorporates five vertical bands, each of which simulates different hydrologic processes. Eventually, a grid-to-grid routing method is used to estimate outlet discharge. The simulation results from the first study accentuated the significance of frozen ground condition on the generation of surface runoff in the RRB. It was found that the concurrent occurrence of frozen ground condition, snowmelt events, and early spring rainfalls in the RRB made the basin prone to frequent spring floods. In addition, it was demonstrated that the abundant surface depressions across the RRB regulate the release of surface runoff and streamflow discharge. Results from the second study revealed that the HTIM improved the representation of temperature variations in snow models. It was found that the daily snowmelt simulations were significantly affected by the sub-daily temperature fluctuations, while the monthly and annual snowmelt results were less prone to such changes. Lastly, results from the third study indicated that although different temperature datasets captured the spatial and temporal patterns of snowmelt in the MRB, the quantities of the simulated snowmelt were different on the western side of the basin with complex topographical features.

ACKNOWLEDGEMENTS

The winding road to a doctorate brings about a life-changing experience that profoundly transforms you. I am fortunate to have shared this road with great mentors, talented students, and loving friends along the way. I would like to express my sincere gratitude to Dr. Xuefeng Chu for his impeccable leadership, infinite patience, and whole-hearted support. I am forever indebted to Dr. Chu for teaching me his professionalism and preparing me for my future career. I would like to acknowledge my committee members: Dr. Day, Dr. Lin, and Dr. Padmanabhan who provided guidance, passion, and support throughout this incredible experience. Their passion was contagious and made me even more passionate about learning and teaching.

I am extending many thanks to my friends in the hydrologic modeling group at NDSU. Thank you, Kendall Grimm, for being such a great friend. I will never forget all the days we spent in the lab on modeling, writing, reporting our MAJOR findings, and coming up with materials for the episodes of "Fun with Hydrology"! Many thanks to my friends Ning Wang, Hadi Bazrkar, and Lan Zeng for putting up with me even on days when I did not have a cup of coffee in the morning!

Thank you, Carissa Botton, for your support, caring, understanding, and listening to me raving about hydrologic modeling and life! Your words of encouragement motivated me to complete this dissertation on time, and you make me a better human being. I am extremely grateful to my loving parents and sister, who pushed me to challenge myself and expand my zone of comfort. Thank you for your unconditional love and sacrifices.

Today when I am at the end of the road to my doctorate, I better understand that learning is a lifelong process and never ends. This degree only paves the way for me and leads to many other exciting roads, in which I will be serving the community that I am living in. Without the help of my family, mentors, friends, and the Fargo-Moorhead community; this was simply impossible.

DEDICATION

To Mother Earth,

as a small token of my appreciation for you!

TABLE OF CONTENTS

LIST OF TABLES

LIST OF FIGURES

LIST OF ABBREVIATIONS

T_{AVE} .....Daily average temperature

C_{HI} .....Heat island effect coefficient

C_{FC} .....Forest canopy effect coefficient

RET .....Reference evapotranspiration

λ.....Latent heat flux

R_e.....Extraterrestrial radiation

K_1 .....Scaling factor

K_2.....Temperature threshold

STG_{SV} .....Short vegetation canopy storage

$RAIN_{CAN}$ .....Rainfall on canopy

$INTC_{CAN}$.....Canopy interception

FVC.....Fractional vegetation cover

$RAIN$.....Total rainfall

LAI.....Leaf area index

$MXSTG_{CAN}$ .....The maximum canopy storage

STG_{EX} .....Excess storage

$MXSTG_{RES}$.....The maximum residue storage

RM .....Residue mass

$INTC_{FRC}$ .....Rainfall interception by the forest canopy

CR_C .....Critical rainfall to saturate forest canopy

ρ .....The ratio of the mean evaporation rate to the mean rainfall rate

ε.....The fraction of truck evaporation

$INTC_{SNO}$.....Snow interception

C_{CU}.....Canopy unloading coefficient

SWE_F .....Snow storage water equivalent of the forest canopy

FCS_{MX} .....The maximum forest canopy snow storage

$SNOW$ .....Snowfall

STG_{SV} .....Snowpack water equivalent storage

$SNOW_S$ .....Snowfall after interception

M_A .....Actual snowmelt

C_{SN} .....Snowfall correction factor

M .....Snowmelt

R .....Refreezing

T_{MAX} .....Daily maximum temperature

T_{MIN} .....Daily minimum temperature

Δt_{MLT} .....Effective melt period

Δt_{RFR} .....Effective refreezing period

C_M .....Melt factor

C_F .....Freezing factor

M_R .....Rain-on-snow melt

ROS .....Rainfall on snowpack

AWM .....Available water for melt

MXSPR .....The threshold for snowmelt generation

C_{WR} .....Water retention storage coefficient

STG_{SV} .....Depression storage

$RAIN_S$ .....Rainfall after interception

$RUNF$ .....Surface runoff

$INFL$ .....Infiltration

E .....Evaporation

$CFGI$ .....Continuous frozen ground index

C_{DC} .....Daily decay coefficient

C_{SR} .....Snow reduction coefficient

$SNOD$ .....Depth of snow on the ground

ρ_s .....Snow density

$SPIL$ .....Spilled water out of depressions

C_{DP} .....Decay factor

$MXSTG_{DP}$ .....The maximum depression storage

$MNSTG_{DP}$ .....The minimum spill threshold storage

K_W .....Open water evaporation coefficient

$SEEP$ .....Amount of water seeping from the depressions

STG_{SV} .....Hydraulic conductivity of the sub-surface layer 1

θ_{S1} .....Soil water content of the sub-surface layer 1

SAT_{S1} .....Soil saturated water content of the sub-surface layer 1

STG_{S1} .....Storage of the sub-surface layer 1

ET_{S1} .....Evapotranspiration from the sub-surface layer 1

$PERC_{S1}$ .....Percolation from the sub-surface layer 1

K_{S1}^{*} .....Adjusted hydraulic conductivity for frozen soil

K_{SAT1} .....Saturated hydraulic conductivity of the sub-surface layer 1

θ_{FR} .....Frozen water content

θ_{NFR} .....Non-frozen water content

K_C .....Crop coefficient

$MXPERC_{S1}$ .....Potential percolation from sub-surface layer 1 to sub-surface layer 2

θ_{S2} .....Soil water content of the sub-surface layer 2

SAT_{S2} .....Soil saturated water content of the sub-surface layer 2

$PERC_{S1}$ .....Actual percolation from sub-surface layer 1 to sub-surface layer 2

AWP_{S1} .....Available water for percolation from sub-surface layer 1

FC_{S1} .....Field capacity of sub-surface layer 1

GWR_{S3} .....Groundwater recharge

C_{GW} .....Groundwater delay factor

$PERC_{S2}$.....Actual percolation from sub-surface layer 2 to sub-surface layer 3

STG_{S3} .....Storage of the sub-surface layer 3

BF_{S3} .....Baseflow threshold

C_{RC} .....Recession constant

Q_C .....Contributing flow

A* .....Grid area after removing the lakes

Q.....Outlet discharge

C_{FR} .....Flow recession coefficient

KGE.....Kling-Gupta efficiency

r .....Linear correlation coefficient

α .....The ratio between standard deviation of simulated and observed data

β .....The ratio between the mean simulated and mean observed values

1. GENERAL INTRODUCTION: TOWARDS MACRO-SCALE MODELING

The climate-driven impacts on temperature and precipitation, as well as increasing demands for freshwater, have intensified the stress on water resources, with varying effects on different regions across the world. The United Nations 2018 report on Sustainable Development Goals suggests that if the unsustainable pressures on global water resources keep growing with the current pace, 52% of the world's population and 40% of global grain production will be at risk by the mid-21st century (UN-Water 2018). For example, climate projections predict warmer temperatures in the Northern Great Plains of the United States which lead to earlier snowmelt and directly impact agriculture in the Dakotas, Montana, Wyoming, and Nebraska (Conant et al. 2018). Although climate models can provide variations of precipitation and temperature over time, understanding the regional water quantity and quality issues requires the use of hydrologic models. Hydrologic models are the simplification of the water-cycle systems and help to understand the past, present, and future state of water resources by facilitating the interpretation of different management decisions (Johnston and Smakhtin 2014).

1.1. Evolution of Hydrologic Models

Increasing demands for representing hydrologic processes at different scales have led researchers to classify hydrologic models into three categories of (1) micro-, (2) meso-, and (3) macro-scale models (Chu et al. 2019). The concept of hydrologic modeling at different scales is similar to using web mapping services. In an online map, zoomed-in views are used to find specific locations and features while zoomed-out maps give a holistic view of prominent geographical features of the area. Similarly, while micro-scale models are used to simulate the local hydrologic processes, macro-scale hydrologic models are associated with regional and continental hydrologic processes and provide simulations for areas larger than a few thousand square kilometers (Döll et al. 2008; Liebscher 1993).

Macro-scale hydrologic modeling is a relatively new field of research, which has flourished over the 21st century (Sood and Smakhtin 2015). Figure 1.1 depicts a schematic

timeline of the significant milestones in the evolution of hydrologic models. The initial attempts to develop a hydrologic model are traced back to 1850s when Mulvany (1850) developed the rational method for estimating the time of concentration and peak discharge of a given basin (Beven 2012; Singh 2018). The development of the rational method was followed by many efforts to simulate other hydrologic processes through the 1960s when the computer revolution significantly improved the computation power (Borah and Bera 2003). Crawford and Linsley (1966) developed the Stanford Watershed Model, one of the first hydrologic models to simulate different hydrologic processes, and paved the way for the emergence of many other hydrologic models for decades to come (Figure 1.1).

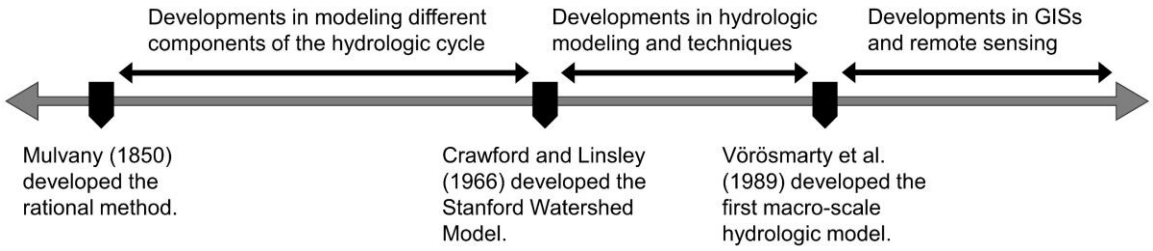

Figure 1.1. Milestones in the evolution of hydrologic models leading to macro-scale hydrologic modeling (GIS: geographic information system).

As one of the initial efforts to substantiate macro-scale hydrologic models, Eagleson (1986) highlighted the necessity of the knowledge of the hydrologic cycle at macro-scale and portrayed a promising future for macro-scale hydrologic models. Specifically, Vörösmarty et al. (1989) developed one of the first macro-scale hydrologic models (Figure 1.1), in which a water balance model was linked to a water transport model to simulate soil moisture, evapotranspiration, and surface runoff in South America. The emergence of Geographic Information Systems (GISs), along with the increasing availability of satellite images and remote sensing data, facilitated pre- and post-processing of meteorological data and led to rapid developments and applications of macro-scale hydrologic models throughout the 21st century.

Several studies have compared different macro-scale hydrologic models based on their capabilities, features, structures, and ability to capture the variations in hydrologic processes

(Gudmundsson et al. 2012; Kauffeldt et al. 2016; Sood and Smakhtin 2015). Sood and Smakhtin (2015) reviewed the capabilities of twelve macro-scale models and discussed general limitations of macro-scale modeling, including uncertainties in hydrologic modeling, incorporation of remotely sensed data, and scaling issues (Sood and Smakhtin 2015). Similarly, Kauffeldt et al. (2016) reviewed 24 macro-scale hydrologic models based on their suitability for flood forecasting in Europe and provided guidance on model selection based on a set of criteria.

Macro-scale hydrologic models are commonly classified based on different aspects, including but not limited to their primary objective, integrated processes, the realm of application, structure, and temporal and spatial resolutions. The majority of the macro-scale hydrologic models are developed with the primary objective of simulating spatiotemporal variations of hydrologic processes. However, there are models that provide more specific features and functions. For example, Water-Global Analysis and Prognosis (WaterGap) (Alcamo et al. 2003) takes into account human interventions in forms of water abstractions and dams. In addition, the model-specific objectives directly affect integrated processes and applications. For instance, integration of reservoir management functions in Soil and Water Assessment Tool (SWAT) (Arnold et al. 1998) enables its application to a wide variety of agricultural water supply and demand problems. Other fields of application of macro-scale hydrologic models include but not limited to floods and droughts, water quality assessment, land-use change, and groundwater depletion (Abbaspour et al. 2015; Nijssen et al. 2001; Wada et al. 2010).

To simulate hydrologic processes, different macro-scale models incorporate two spatial discretization approaches (i.e., grid-based and sub-basin-based), each of which has unique advantages and disadvantages (Chu et al. 2019). Grid-based models such as Spatial Processes in Hydrology (SPHY) (Terink et al. 2015) can easily incorporate available grid-based satellite image products such as Leaf Area Index (LAI). On the other hand, sub-basin-based models such as Hydrological Predictions for the Environment (HYPE) (Lindström et al. 2010) can use different station-based data (e.g., precipitation or temperature) into different sub-basins. In addition to

the model structure, the temporal and spatial resolutions of different models vary depending on the input data requirements and model-specific recommendations. The temporal resolution of the majority of macro-scale hydrologic models is daily or larger, depending on the recommendations of the model developers. For example, Arnell (1999) suggested that since monthly runoff shows lower sensitivity to the calibrated routing parameters, a monthly resolution for Macro-scale Probability-Distributed Moisture (Macro-PDM) (Arnell 1999) generates better outputs. The spatial resolution of different models depends on the availability of input data. However, there are some model-specific recommendations on spatial resolution. For example, Variable Infiltration Capacity (VIC) (Liang et al. 1994) simulates land surface processes for grid resolution larger than 1 km, and WaterGap performs its computations with the spatial resolution of 55 km.

1.2. Research Gaps

Due to the extent and magnitude of the climate-driven changes across the world, macro-scale hydrologic models are becoming increasingly popular. However, there are only a few macro-scale models to simulate hydrologic processes in depression-dominated cold climate regions. Specifically, cold climate regions are distinguished by their cold and lingering winters, in which the land surface is covered by a thick snowpack layer for several months, leading to a frozen-ground condition and consequently spring floods. For example, the Red River of the North Basin (RRB) is a typical cold climate basin that encounters frequent spring floods as a result of its cold climate, spring snowmelt as well as its unique topography (Lin et al. 2015). Figure 1.2 portrays an illustrative example of how the RRB functions in early springs. Two snapshots of the Red River on 1st Avenue Bridge in Fargo during the 2019 spring flood and variations of soil temperature with depth on March 21st and April 8th are depicted in Figure 1.2a-d. In the 20-day period from March 21st to April 8th, the hourly air temperatures were constantly fluctuating around the freezing temperature, creating a susceptible environment for the generation of snowmelt. However, the top layers of the soil (top 100 cm) were fully or partially

frozen (Figure 1.2b and Figure 1.2d), affecting infiltration and surface runoff generation. The frozen soil condition, together with other variables such as flat topography, snowmelt, ice jams, and precipitation over the basin, led to the Red River's highest streamflow discharge peak on April 8th, 2019 (549 m^3/s at Fargo, Station ID 05054000) (Figure 1.2c). The 2019 flood is just an example of recurring floods in late-March and early-April period and highlights the impacts of cold climate conditions in the hydrologic response of the RRB.

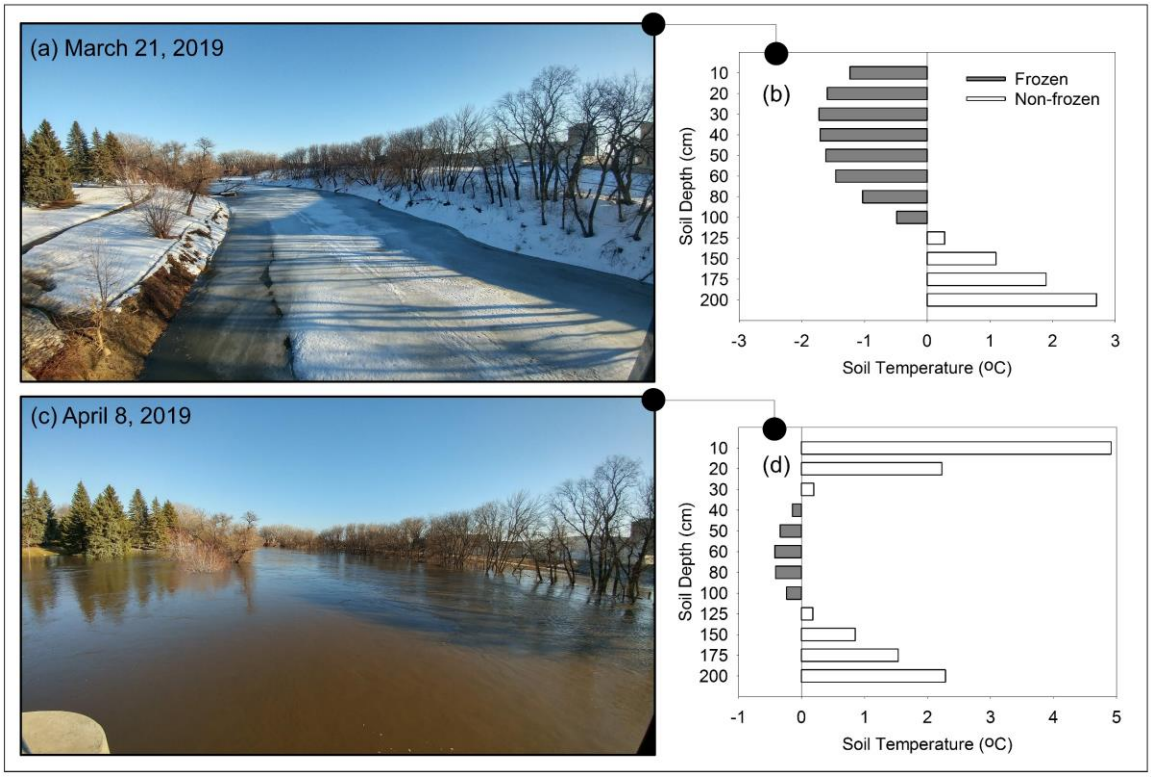

Figure 1.2. Snapshots of the Red River (on 1st Avenue Bridge, Fargo, ND) during the 2019 spring flood and soil temperature variations with depth on (a and b) March 21, 2019 and (c and d) April 8, 2019. Soil temperature data are obtained from North Dakota Agricultural Weather Network (NDAWN 2019) at Fargo Station (Latitude:46.897°, Longitude:-96.812°).

Several studies indicated that models that do not account for cold climate characteristics (e.g., frozen ground and snowmelt) are not able to capture the recurring spring floods (Chu et al. 2019; Tahmasebi Nasab et al. 2018). For example, the majority of macro-scale models take advantage of a simple temperature index method to simulate snowmelt over the basin (e.g., Bergström 1992; Terink et al. 2015). One of the critical simplifying assumptions behind

temperature index methods that restricts their application is that each timestep is represented by a single temperature (i.e., the daily average temperature). However, when sub-daily temperatures fluctuate above or below the freezing temperature, the single-temperature methods cannot provide realistic snowmelt simulations (Žaknić-Ćatović et al. 2018).

In addition to the cold climate conditions, the filling-spilling process associated with depressions in depression-dominated areas is another important process that affects the timing and magnitude of generated surface runoff. Surface depressions are usually considered as "micro-scale" topographic features of a surface. However, depression-dominated areas are characterized by numerous surface depressions that collectively alter and manipulate the "macro-scale" hydrologic processes. The depression-dominated areas act as the "gatekeepers" and are controlled by a filling-spilling process (Tahmasebi Nasab et al. 2017a). Tahmasebi Nasab et al. (2018) investigated the significance of considering depressions in water quality and quantity modeling of RRB. It was found that neglecting the role of surface depressions in the modeling of depression-dominated basins may result in unrealistic surface runoff simulations (Tahmasebi Nasab et al. 2018).

Several "micro-scale" methods and models have been developed to account for the complexities associated with identifying and modeling depressions (Chu et al. 2013; Tahmasebi Nasab et al. 2017b). For example, Chu et al. (2013) developed a micro-scale Puddle-to-Puddle (P2P) hydrologic modeling system which routes water from one depression to another and eventually to the outlet of a surface. P2P uses the Puddle Delineation (PD) algorithm (Chu et al. 2010) that identifies depressions based on topographical features of the surface and provides a variety of characteristics associated with depressions such as maximum depression storage, maximum ponding area, and the hierarchical relationships of depressions. Although the imperative importance of depressions-dominated areas has been emphasized in many studies (e.g., Chu 2015; Chu et al. 2013), the majority of macro-scale models either ignore depressions

or employ lumped and simplistic approaches to simulate their effects on the outlet streamflow discharge.

1.3. Objectives and Tasks

Given the significance of macro-scale modeling in depression-dominated cold climate regions, the primary objectives of this dissertation research are threefold:

- to improve the understanding of macro-scale hydrologic processes in cold climate regions,
- to improve the macro-scale representation and modeling of depression-dominated regions, and
- to improve the land use and land cover representation in macro-scale hydrologic models.

Achieving these objectives requires three specific tasks: (1) to develop a Macro-Scale Hydrologic Processes Simulator (Macro-HyProS), tailored for cold-climate conditions and depression-dominated areas; (2) to test Macro-HyProS by coupling it with downscaled satellite-based meteorological datasets to facilitate large-scale modeling; and (3) to investigate the impacts of micro-topography and spatiotemporal scales on the macro-scale modeling. The simulation results are presented in forms of maps and graphs to highlight the unique features of Macro-HyProS and provide insight into the future applications of the model.

1.4. Organization of the Dissertation

The contents of this dissertation are organized into five chapters. Chapter 1 provides a general introduction to the evolution of hydrologic models and developments towards macro-scale hydrologic modeling. Notably, the limitations of macro-scale hydrologic models in depression-dominated cold climate regions are presented, which provide a basis for the specific objectives and tasks of the dissertation.

Chapter 2 introduces a new Macro-scale Hydrologic Processes Simulator (Macro-HyProS) which is tailored for cold climate regions and depression-dominated terrains. Macro-

HyProS is a grid-based hydrologic model of a unique LEGO-fashion structure to deal with hydrologic complexities associated with depression-dominated cold climate regions. In addition to presenting the methodologies, the capabilities of Macro-HyProS in describing the spatiotemporal variations of hydrologic processes are tested in the Red River of the North Basin.

Chapter 3 evaluates the impacts of sub-daily temperature fluctuations around the freezing temperature (i.e., 0^{o}C) on the quantity and spatial distribution of snowmelt simulations. Unlike other existing macro-scale models that rely upon a single daily average temperature, the snow model in Macro-HyProS incorporates minimum and maximum temperatures and their occurrence timing within the day in a hybrid temperature index method. The model is applied to the Missouri River Basin to simulate grid-based snowmelt. Simulation results are compared with the snowmelt data from the SNOw Data Assimilation System (SNODAS).

Chapter 4 assesses the influences of using two different high-resolution gridded temperature datasets on macro-scale snowmelt simulations in the Missouri River Basin. Specifically, temperature datasets from Parameter-elevation Relationships on Independent Slopes Model (PRISM) and Topography Weather (TopoWx) are utilized to simulate snowmelt for two representative flood and drought years. The impacts of the two datasets on the quantity and distribution of snowmelt are evaluated by applying the model in the Missouri River Basin, which possesses a unique complex topography.

Lastly, Chapter 5 provides a summary of the conducted studies and highlights specific conclusions and implications. In addition, future research directions and potential improvements to Macro-HyProS are briefly discussed.

1.5. References

Abbaspour, K. C., Rouholahnejad, E., Vaghefi, S., Srinivasan, R., Yang, H., and Kløve, B. (2015). "A continental-scale hydrology and water quality model for Europe: Calibration and

uncertainty of a high-resolution large-scale SWAT model." *Journal of Hydrology*, Elsevier, 524, 733–752.

Alcamo, J., Döll, P., Henrichs, T., Kaspar, F., Lehner, B., Rösch, T., and Siebert, S. (2003). "Development and testing of the WaterGAP 2 global model of water use and availability." *Hydrological Sciences Journal*, Taylor & Francis, 48(3), 317–337.

Arnell, N. . (1999). "A simple water balance model for the simulation of streamflow over a large geographic domain." *Journal of Hydrology*, Elsevier, 217(3–4), 314–335.

Arnold, J. G., Srinivasan, R., Muttiah, R. S., and Williams, J. R. (1998). "Large Area Hydrologic Modeling and Assessment Part I: Model Development." *Journal of the American Water Resources Association*, Blackwell Publishing Ltd, 34(1), 73–89.

Bergström, S. (1992). *The HBV model: Its structure and applications*. Swedish Meteorological and Hydrological Institute, Norrköping, Sweden.

Beven, K. J. (2012). *Rainfall-runoff modelling: the primer*. John Wiley & Sons.

Borah, D. K., and Bera, M. (2003). "Watershed-scale hydrologic and nonpoint-source pollution models: Review of mathematical bases." *Transactions of the ASAE*, 46(6), 1553–1566.

Chu, X. (2015). "Delineation of Pothole-Dominated Wetlands and Modeling of Their Threshold Behaviors." *Journal of Hydrologic Engineering*, American Society of Civil Engineers, D5015003.

Chu, X., Lin, Z., Tahmasebi Nasab, M., Zeng, L., Grimm, K., Bazrkar, M. H., Wang, N., Liu, X., Zhang, X., and Zheng, H. (2019). "Macro-scale grid-based and subbasin-based hydrologic modeling: joint simulation and cross-calibration." *Journal of Hydroinformatics*, 21(1), 77–91.

Chu, X., Yang, J., Chi, Y., and Zhang, J. (2013). "Dynamic puddle delineation and modeling of puddle-to-puddle filling-spilling-merging-splitting overland flow processes." *Water Resources Research*, 49(6), 3825–3829.

Chu, X., Zhang, J., Chi, Y., and Yang, J. (2010). "An Improved Method for Watershed Delineation and Computation of Surface Depression Storage." *Watershed Management 2010*, American Society of Civil Engineers, Reston, VA, 1113–1122.

Conant, R., Kluck, D., Anderson, M., Badger, A., Boustead, B. M., Derner, J., Farris, L., Hayes, M., Livneh, B., McNeeley, S., Peck, D., Shulski, M., and Small, V. (2018). "Northern Great Plains." *Impacts, Risks, and Adaptation in the United States: Fourth National Climate Assessment, Volume II*, K. E. Reidmiller, D.R., C.W. Avery, D.R. Easterling and and B. C. S. Kunkel, K.L.M. Lewis, T.K. Maycock, eds., U.S. Global Change Research Program, Washington, DC, USA, 941–986.

Crawford, N. H., and Linsley, R. K. (1966). *Digital simulation in hydrology: Stanford Watershed Model IV*. Palo Alto, Calif.

Döll, P., Berkhoff, K., Bormann, H., Fohrer, N., Gerten, D., Hagemann, S., and Krol, M. (2008). "Advances and visions in large-scale hydrological modelling: findings from the 11th Workshop on Large-Scale Hydrological Modelling." *Adv. Geosci*, 18, 51–61.

Eagleson, P. S. (1986). "The emergence of global-scale hydrology." *Water Resources Research*, 22(9S), 6S-14S.

Gudmundsson, L., Tallaksen, L. M., Stahl, K., Clark, D. B., Dumont, E., Hagemann, S., Bertrand, N., Gerten, D., Heinke, J., Hanasaki, N., Voss, F., and Koirala, S. (2012). "Comparing Large-Scale Hydrological Model Simulations to Observed Runoff Percentiles in Europe." *Journal of Hydrometeorology*, 13(2), 604–620.

Johnston, R., and Smakhtin, V. (2014). "Hydrological Modeling of Large River Basins: How Much is Enough?" *Water Resources Management*, Springer Netherlands, 28(10), 2695–2730.

Kauffeldt, A., Wetterhall, F., Pappenberger, F., Salamon, P., and Thielen, J. (2016). "Technical review of large-scale hydrological models for implementation in operational flood

forecasting schemes on continental level." *Environmental Modelling and Software*, Elsevier Ltd, 75, 68–76.

Liang, X., Lettenmaier, D. P., Wood, E. F., and Burges, S. J. (1994). "A simple hydrologically based model of land surface water and energy fluxes for general circulation models." *Journal of Geophysical Research*, 99(D7), 14415.

Liebscher, H. J. (1993). "Hydrology for the water management of large river basins." *Hydrological Sciences Journal*, Taylor & Francis Group, 38(1), 1–13.

Lin, Z., Anar, M. J., and Zheng, H. (2015). "Hydrologic and water-quality impacts of agricultural land use changes incurred from bioenergy policies." *Journal of Hydrology*, 525, 429–440.

Lindström, G., Pers, C., Rosberg, J., Strömqvist, J., and Arheimer, B. (2010). "Development and testing of the HYPE (Hydrological Predictions for the Environment) water quality model for different spatial scales." *Hydrology Research*, 41(3–4).

Mulvany, T. J. (1850). "On the use of self-registering rain and flood gauges." *Transactions of the Institution of Civil Engineers of Ireland*, 4(2), 1–8.

NDAWN. (2019). "NDAWN - North Dakota Agricultural Weather Network." <https://ndawn.ndsu.nodak.edu/> (Jun. 11, 2019).

Nijssen, B., O'Donnell, G. M., Lettenmaier, D. P., Lohmann, D., Wood, E. F., Nijssen, B., O'Donnell, G. M., Lettenmaier, D. P., Lohmann, D., and Wood, E. F. (2001). "Predicting the Discharge of Global Rivers." *Journal of Climate*, 14(15), 3307–3323.

Singh, V. P. (2018). "Hydrologic modeling: progress and future directions." *Geoscience Letters*, Nature Publishing Group, 5(1), 15.

Sood, A., and Smakhtin, V. (2015). "Global hydrological models: a review." *Hydrological Sciences Journal*, Taylor & Francis, 60(4), 549–565.

Tahmasebi Nasab, M., Grimm, K., Bazrkar, M., Zeng, L., Shabani, A., Zhang, X., and Chu, X. (2018). "SWAT Modeling of Non-Point Source Pollution in Depression-Dominated Basins

under Varying Hydroclimatic Conditions." *International Journal of Environmental Research and Public Health 2018, Vol. 15, Page 2492*, 15(11), 2492.

Tahmasebi Nasab, M., Singh, V., and Chu, X. (2017a). "SWAT Modeling for Depression-Dominated Areas: How Do Depressions Manipulate Hydrologic Modeling?" *Water*, Multidisciplinary Digital Publishing Institute, 9(1), 58.

Tahmasebi Nasab, M., Zhang, J., and Chu, X. (2017b). "A New Depression -Dominated Delineation (D-cubed) Method for Improved Watershed Modeling." *Hydrological Processes*, 31(19), 3364–3378.

Terink, W., Lutz, A. F., Simons, G. W. H., Immerzeel, W. W., and Droogers, P. (2015). "SPHY v2.0: Spatial Processes in HYdrology." *Geoscientific Model Development*, 8(7), 2009–2034.

UN-Water. (2018). "SDG 6 Synthesis Report 2018 on Water and Sanitation." *United Nations*, <http://www.unwater.org/publication_categories/sdg-6-synthesis-report-2018-on-water-and-sanitation/> (Feb. 27, 2019).

Vörösmarty, C. J., Moore, B., Grace, A. L., Gildea, M. P., Melillo, J. M., Peterson, B. J., Rastetter, E. B., and Steudler, P. A. (1989). "Continental scale models of water balance and fluvial transport: An application to South America." *Global Biogeochemical Cycles*, 3(3), 241–265.

Wada, Y., van Beek, L. P. H., van Kempen, C. M., Reckman, J. W. T. M., Vasak, S., and Bierkens, M. F. P. (2010). "Global depletion of groundwater resources." *Geophysical Research Letters*, John Wiley & Sons, Ltd, 37(20).

Žaknić-Ćatović, A., Howard, K. W. F., and Ćatović, Z. (2018). "Modification of the degree-day formula for diurnal meltwater generation and refreezing." *Theoretical and Applied Climatology*, 131(3–4), 1157–1171.

2. MACRO-HYPROS: A NEW MACRO-SCALE HYDROLOGIC PROCESSES SIMULATOR FOR DEPRESSION-DOMINATED COLD CLIMATE REGIONS[1]

2.1. Abstract

This study introduces a new Macro-scale Hydrologic Processes Simulator (Macro-HyProS), tailored for cold climate regions and depression-dominated terrains. Macro-HyProS is a grid-based hydrologic model of a unique structure to deal with hydrologic complexities in depression-dominated cold climate regions. The model runs on a daily time step and incorporates a LEGO-fashion horizontal layout to account for sub-grid land use heterogeneity. On the vertical layout, each grid consists of different bands, each of which is responsible for simulating specific hydrologic processes. Macro-HyProS employs improved methodologies to account for snow accumulation and ablation, depressions, and frozen ground condition. The Red River of the North Basin (RRB) was selected to highlight the capabilities of Macro-HyProS in describing the spatiotemporal complexities associated with depression-dominated cold climate regions. Results indicated that the model provided a satisfactory performance, having the Nash–Sutcliffe efficiency coefficients of 0.56 and 0.72 in the calibration and validation periods, respectively. The modeling results accentuated the impacts of frozen ground, snowmelt, and depressions in the generation of surface runoff over the basin. On average, the RRB experienced 145 days of frozen or partially frozen ground conditions per year, which coincided with early spring rainfall and snowmelt events. Due to the widespread frozen ground conditions over the basin, up to 60% of the generated snowmelt on specific days contributed to surface runoff, whereas infiltration had a smaller portion. Also, the results revealed that the depression-dominated areas acted as “regulators” of surface runoff, particularly in early springs. Macro-

[1] The material in this chapter was co-authored by Mohsen Tahmasebi Nasab and Dr. Xuefeng Chu. Mohsen Tahmasebi Nasab had primary responsibility for developing the new analysis procedure and modeling of the system. Mohsen Tahmasebi Nasab was the primary developer of the conclusions that are advanced here. Mohsen Tahmasebi Nasab also drafted and revised all versions of this chapter. Dr. Xuefeng Chu served as proofreader and checked analysis conducted by Mohsen Tahmasebi Nasab.

HyProS provides spatiotemporal simulations of various hydrologic processes to facilitate a better understanding of macro-scale hydrologic trends.

2.2. Introduction

The idea of hydrologic modeling at different spatial scales (i.e., micro, meso, and macro) is comparable to using web mapping services. In an online map, zoomed-in views are used to find specific locations and features while zoomed-out maps give a holistic view of prominent geographical features of the area. Similarly, micro-scale hydrologic models are used to investigate the local hydrologic process, such as filling, spilling, and merging of surface depressions (Chu et al. 2013). On the other hand, macro-scale hydrologic models are associated with regional and continental hydrologic processes and provide large-scale simulations for areas larger than a few thousand square kilometers (Chu et al. 2019; Döll et al. 2008).

Macro-scale hydrologic modeling is a relatively new field of research, which has flourished over the 21st century (Sood and Smakhtin 2015). As one of the initial efforts to substantiate macro-scale models, Eagleson (1986) highlighted the necessity of the knowledge of the hydrologic cycle at a macro scale and portrayed a promising future for macro-scale hydrologic models, suggesting that the future of hydrology is intertwined with macro-scale hydrologic models. Vörösmarty et al. (1989) developed one of the first macro-scale hydrologic models, in which a water balance model was linked to a water flow model to simulate soil moisture, evapotranspiration, and surface runoff in South America. Although before the 21st century, the macro-scale models were considered as “exotic” siblings of catchment models (Döll et al. 2008), large-scale climate-driven changes have led to rapid developments and applications of macro-scale hydrologic models throughout the 21st century. The emergence of the Geographic Information System (GIS), along with the increasing availability of satellite images and remote sensing data, facilitated pre- and post-processing of meteorological and hydrological data and applications of macro-scale hydrologic models in different study areas. The applications of macro-scale hydrologic models around the world have indicated that they are useful tools for a

variety of subjects such as impacts of climate-driven changes on water resources (Arnell and Gosling 2013), flood and drought return period analysis (Lehner et al. 2006), and hydrologic implications of human activities (Syvitski et al. 2005).

There are several studies with the primary goal of evaluating different macro-scale hydrologic models based on their capabilities, features, structures, and abilities to capture the variations in hydrologic processes (Gudmundsson et al. 2012; Kauffeldt et al. 2016; Sood and Smakhtin 2015). For example, Sood and Smakhtin (2015) highlighted the capabilities and limitations of twelve macro-scale models and discussed general limitations of macro-scale modeling, including the uncertainties in hydrologic modeling, incorporation of remotely sensed data, and scaling issues. Similarly, Kauffeldt et al. (2016) reviewed 24 macro-scale hydrologic models based on their suitability for flood forecasting in Europe and provided guidance on model selection based on a set of criteria. The selected criteria such as input data requirement, flexibility to grid structure, flexibility in resolution, and possibility of calibration using suitable tools were chosen to accentuate the implementation of hydrologic models on a macro scale (Kauffeldt et al. 2016). It was concluded that although these criteria were subjective to the specific applications of hydrologic models, they could serve as an initial step in the model selection for operational flood forecasting schemes (Kauffeldt et al. 2016).

Macro-scale hydrologic models can be classified from different aspects such as their (1) primary objective(s), (2) integrated processes, (3) area of application (e.g., impacts of land use change), (4) structure, and (5) temporal and spatial resolutions. Although the majority of the macro-scale hydrologic models have been developed with the primary objective of simulating spatial and temporal variations of hydrologic processes, some possess more specific features and functions. For example, the Water-Global Analysis and Prognosis (WaterGap) (Alcamo et al. 2003) takes into account human interventions in forms of water abstractions and dams; and the Variable Infiltration Capacity (VIC) (Liang et al. 1994) considers sub-grid heterogeneity through statistical distributions. Also, the model-specific objectives directly affect the integrated

processes and applications of the models. For instance, the integration of reservoir management functions in the Soil and Water Assessment Tool (SWAT) (Arnold et al. 1998) enables its application to a wide range of agricultural water supply and demand problems.

To simulate hydrologic processes, macro-scale models generally incorporate two spatial discretization structures: (1) grid-based and (2) subbasin-based, each of which has unique advantages and disadvantages (Chu et al. 2019). Grid-based models such as Spatial Processes in Hydrology (SPHY) (Terink et al. 2015) can easily take advantage of available gridded satellite image products such as Leaf Area Index (LAI). On the other hand, subbasin-based models such as Hydrological Predictions for the Environment (HYPE) (Lindström et al. 2010) can incorporate station-based observations (e.g., precipitation and temperature) into different subbasins. The spatial resolution of different models depends on the availability of input data. However, there are some model-specific recommendations on spatial resolution. For example, VIC simulates land surface processes for grids larger than 1 km, while WaterGap performs its simulations with a spatial resolution of 55 km.

Although macro-scale hydrologic models are becoming increasingly popular, there are only a few macro-scale models for cold climate regions, such as Ecological Model for Applied Geophysics (ECOMAG) (Motovilov et al. 1999) developed for the northern hemisphere climate processes land-surface experiment (NOPEX). Motovilov (2016) used ECOMAG to simulate snow water equivalent for the macro-scale Volga basin over a period from 2001 to 2011. Results indicated a good agreement between the simulated and observed time series of total snow water equivalent over the basin (Motovilov 2016). The cold climate regions are characterized by their long and cold winters, in which snow covers the land surface for several months, leading to a frozen ground condition and consequently spring floods. The Red River of the North Basin (RRB) is a typical example of the cold climate regions, which experiences frequent spring floods as a result of its frozen ground condition, early spring snowmelt, as well as its unique flat topography (Lin et al. 2015). Several studies have suggested that hydrologic models that do not

account for cold climate characteristics (e.g., frozen soil and snowmelt) are not able to capture the recurring spring floods in the RRB (Chu et al. 2019; Tahmasebi Nasab et al. 2018). In addition to the cold climate condition, the filling-spilling mechanism of depressions in depression-dominated areas dominates the timing and magnitude of generated surface runoff. Depression-dominated areas are typified by numerous surface depressions that collectively alter the macro-scale hydrologic processes. Such depressions act as the "gatekeepers," controlled by the filling-spilling process. Although some methods and models have been developed to identify and model the dynamics of depressions and their hierarchical relationships (e.g., Chu et al., 2013; Tahmasebi Nasab et al., 2017b), the majority of these models are mainly applied to micro-scale simulations (Tahmasebi Nasab et al. 2017a). To point out the correlation between spatial scales and the delineated characteristics of depressions, Tahmasebi Nasab et al. (2017a) performed scale analyses of 70 different digital elevation model (DEM) resolutions, ranging from 2 m to 105 m, for a depression-dominated site in the Prairie Pothole Region of North Dakota. They identified a "threshold resolution" and showed that hydrologic modeling results were highly influenced by using DEM resolutions coarser than the threshold resolution.

In this study, a Macro-scale Hydrologic Processes Simulator (Macro-HyProS) is developed with the primary objective of modeling hydrologic processes in depression-dominated cold climate regions. Macro-HyProS is a grid-based hydrologic model that runs on a daily time step and incorporates a novel LEGO-fashion layout to account for sub-grid heterogeneity and land use change. In addition to the novel horizontal layout, the model utilizes widely available meteorological datasets, delineated micro-topographic features, and improved methodologies to account for the influences of surface depressions and cold-climate conditions on different hydrologic processes such as snowmelt, surface runoff, and infiltration. Macro-HyProS simulates hydrologic processes in five different bands and uses a simple flow routing procedure to estimate streamflow discharge. To deal with the complexities associated with depression-dominated cold climate regions, Macro-HyProS uses improved methodologies to

account for depressions, snow accumulation and ablation, and frozen conditions. The RRB, known for its depression-dominated topography and cold-climate features, is selected as a testing example to demonstrate the capabilities of the Macro-HyProS. The simulation results are presented in forms of maps and graphs, highlighting the unique features of Macro-HyProS and providing guidance for future applications of the model.

2.3. Methodology

2.3.1. Model Structure

In Macro-HyProS, a surface is discretized into a user-defined number of square grids, and simulation is implemented in a grid-based fashion (Figure 2.1). Selecting a proper grid resolution is a function of available input datasets, spatial scales, and the incorporated methodologies (Chu et al. 2019; Oubeidillah et al. 2014). However, since Macro-HyProS is a macro-scale hydrologic model, the spatial resolution of larger than 1 km is recommended for simulating different hydrologic processes. The resolution greater than 1 km has also been suggested by other macro-scale hydrologic models such as VIC (Liang et al. 1994). Most macro-scale hydrologic models neglect the within-grid heterogeneity of coarse resolution grids and regard each grid as a homogeneous unit; however, within-grid variations of land use and land cover can alter different hydrologic processes such as surface runoff generation. Macro-HyProS incorporates a LEGO-fashion layout for each grid to account for within-grid heterogeneity. Particularly, a set of RGB (Red, Green, and Blue) building blocks sit on top of a uniform LEGO plate, representing land use variations within a grid (Figure 2.1). The Red, Green, and Blue Blocks denote developed, vegetated, and wetted areas within a plate, respectively, and can be defined based on the available land use maps.

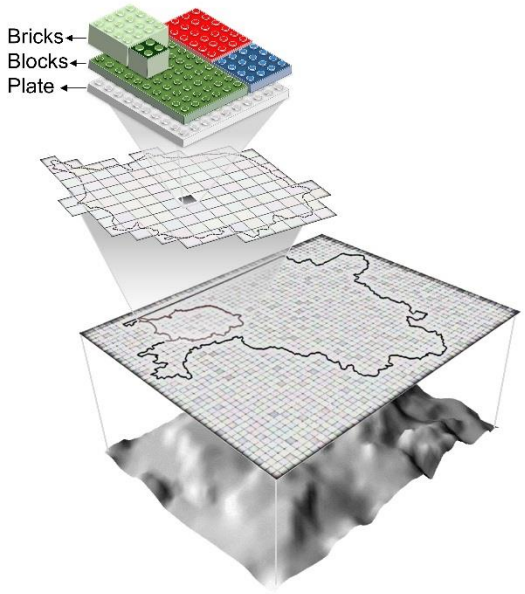

Figure 2.1. Horizontal structure of Macro-HyProS: a LEGO-fashion RGB (Red, Green, and Blue) block layout, in which Red Block represents the developed area, Green Block represents the vegetated area, and Blue Block represents the wetted area.

In addition to the building blocks, different bricks can be placed on top of the RGB Blocks to further account for land use details (Figure 2.1). For example, multiple bricks sitting on top of the Green Block represent different crops and vegetation types (e.g., cereals or sugar crops). Macro-HyProS simulates 14 bricks, listed in Table 2.1, out of which eleven are on top of the Green Block, two are on top of the Blue Block, and one is on top of the Red Block. The crop classification presented in Table 2.1 is based on the Food and Agriculture Organization (FAO) Indicative Crop Classification version 1.1 (FAO Statistical Development Series-15 2017). Although the geographic locations and orientations of different brick types are not taken into account, the coverage percentage of each brick over a grid can be calculated using the zonal statistics tools in GISs. Different parameters are then assigned to each brick and hydrologic processes are calculated for each brick separately. It should be noted that depending on the specific characteristics of a study area, the user can modify and change brick parameters for different regions. The LEGO-fashion layout allows the model to simulate continuous land use changes at a sub-grid scale, which can affect different hydrologic processes such as interception

or surface runoff generation. When hydrologic processes are simulated for all bricks within a grid, a weighted average method is used to calculate hydrologic processes for the grid and consider the degrees of importance of bricks. As an example, Figure 2.2 depicts the land use variations in 2006 and 2007 over a sample grid of 4×4 km² in the RRB (UTM coordinates: 5,206,174 m, 737,859 m), based on the Cropland Data Layer (CDL) database (Boryan et al. 2011). A visual comparison between Figures 2.2a and 2.2b indicates that the majority of the grid is covered by oilseed crops in 2006 and cereals in 2007. Although this is a subtle change for a 4×4 km² grid, the collective land use changes can impact different hydrologic processes at a macro scale, which are simulated in Macro-HyProS through the LEGO-fashion modeling structure.

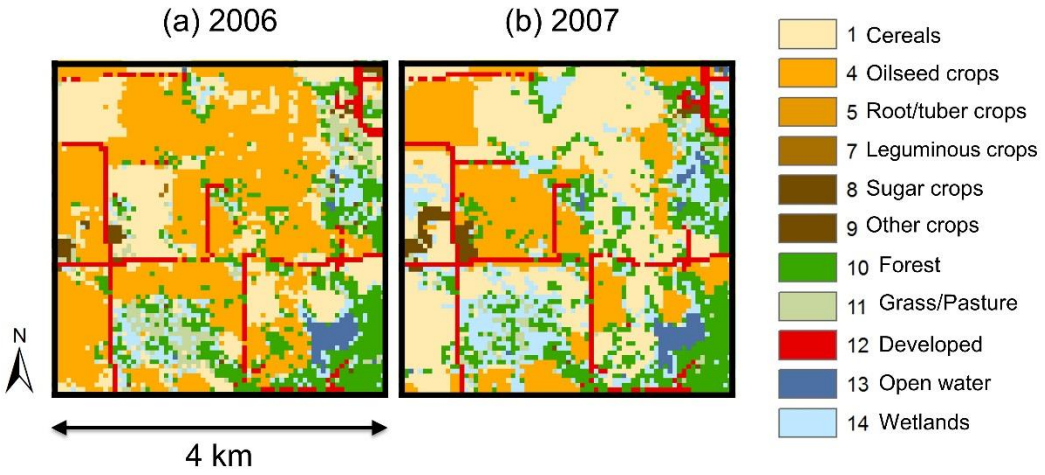

Figure 2.2. Agricultural land use change in a sample grid in the Red River of the North Basin (RRB) based on the Cropland Data Layer (CDL) database for 2006 and 2007 (UTM coordinates of the grid center: 5,206,174 m, 737,859 m).

In addition to the LEGO-fashion horizontal structure, Macro-HyProS accounts for five stratified vertical bands (i.e., Atmosphere, Vegetation, Snow, Surface, and Sub-surface Bands) in the modeling. Figure 2.3 presents a simplified flow diagram of Macro-HyProS illustrating its workflow and the order of the bands in the program. The model was programmed by using the Intel® Fortran (Intel 2019) and Python 2.7 (Python 2010). Since Macro-HyProS reads inputs and prints outputs in a TXT format, the ArcGIS ArcPy package (Environmental Systems

Research Institute 2014) was used to facilitate pre- and post-processing of the GIS data. Specifically, processes such as data preparation, data analysis, conversion, and map automation for input and output files are performed using the ArcPy package within Python 2.7. The primary function of the pre-processing programs is to prepare input data in a TXT format for Macro-HyProS (Figure 2.3). For example, a pre-processing program calculates the coverage percentage of different bricks on top of each grid by analyzing land use maps using a zonal histogram function. The prepared input data are used by the model to simulate different hydrologic processes within three loops, including the brick, grid, and time loops (Figure 2.3). The relationships between different bands and descriptions of different hydrologic processes simulated by the model within each band are detailed in Section 2.2. Eventually, flow routing is implemented and a set of post-processing programs are used for visualization purposes.

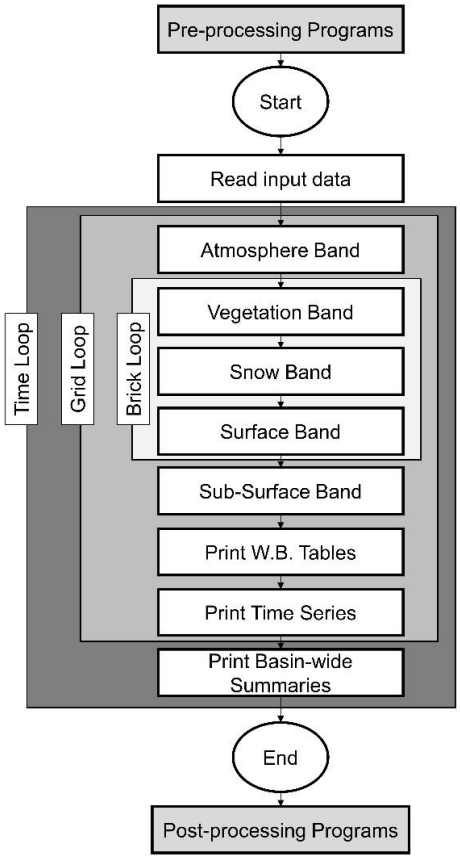

Figure 2.3. Simplified flow diagram of Macro-HyProS (W.B. denotes water balance).

2.3.2. Macro-HyProS Bands: How Are Hydrologic Processes Simulated?

2.3.2.1. Atmosphere Band

Three main functions of the Atmosphere Band in Macro-HyProS are to (1) separate rainfall from snowfall based on the precipitation input, (2) modify the average temperature for specific bricks (optional), and (3) estimate the daily reference evapotranspiration (RET) for each grid.

2.3.2.1.1. Precipitation Separation

The majority of macro-scale hydrologic models use a single threshold temperature to distinguish rainfall from snowfall. However, some models provide more refinements to the single threshold temperature approach. For example, users have an option to input rainfall and snowfall time series in HYPE (Lindström et al. 2010). In addition, in HYPE and HBV96 (Lindström et al. 1997), the single threshold temperature approach is replaced by a temperature interval around the threshold temperature to allow the simultaneous occurrence of rainfall and snowfall (i.e., mixed rainfall and snowfall). Macro-HyProS employs a user-defined transitional temperature range (TTR) to determine rainfall, snowfall, and mixed rainfall and snowfall (Tahmasebi Nasab and Chu 2019a). Figure 2.4 shows a simplified illustration of the separation process: (1) rainfall for $T_{AVE} \geq TT_{MAX}$, (2) snowfall for $T_{AVE} \leq TT_{MIN}$, and (3) mixed rainfall and snowfall for $TT_{MIN} < T_{AVE} < TT_{MAX}$. A linear relationship is assumed for the transition of snowfall and rainfall from TT_{MIN} to TT_{MAX}.

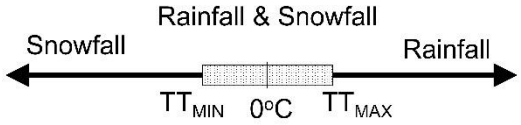

Figure 2.4. Precipitation separation: (1) rainfall, (2) snowfall, and (3) mixed rainfall and snowfall (TT_{MIN} and TT_{MAX} are the minimum and maximum threshold temperatures).

2.3.2.1.2. Average Temperature Adjustment

T_{AVE} in Macro-HyProS represents an average temperature over a grid; however, the temperature in different bricks can vary from the average grid temperature. For example,

developed areas may create urban heat islands, which lead to higher temperatures in towns, cities, or developed regions (Oke 1973). In addition to urban heat islands, it has been observed that forest canopies play a moderating role in the below canopy temperature by decreasing the daily maximum temperature and increasing the daily minimum temperature (Von Arx et al. 2012). To account for the impacts of heat islands in the developed regions and temperature variations under forest canopies, Macro-HyProS provides an option to adjust T_{AVE} for the Developed and Forest Bricks based on two coefficients in the following equation:

$$T_{AVE}(t,g,k) = \begin{cases} C_{HI} \times T_{AVE}(t,g) & Developed\ Brick \\ C_{FC} \times T_{AVE}(t,g) & Forest\ Brick \end{cases} \quad (2.1)$$

in which $T_{AVE}(t, g, k)$ is the average temperature for time t, grid g, and brick k; and the two coefficients C_{HI} and C_{FC} represent the heat island effect and the forest canopy effect, respectively. When C_{HI} and C_{FC} are equal to 1, T_{AVE} is not changed and when C_{HI} and C_{FC} are less/more than 1, T_{AVE} is adjusted.

2.3.2.1.3. Reference Evapotranspiration (RET)

Different macro-scale hydrologic models tend to employ (1) the Penman-Monteith method (and its variants), (2) simple temperature-based methods, (3) user-specified time series, or (4) other methods to estimate RET. For example, evapotranspiration in the VIC model (Liang et al. 1994) is estimated by using the Penman-Monteith equation (Monteith 1965), which requires the details on vapor pressure deficient, radiation, and many other variables. Another group of models do not limit users to a specific RET relationship and provide multiple options for calculating RET. HYPE (Lindström et al. 2010) can simulate reference evapotranspiration by using different methods with varying levels of complexities: (1) modified Jensen-Haise/McGuiness (Oudin et al. 2005), (2) Hargreaves and Samani (Hargreaves and Samani 1985), (3) Priestley and Taylor's (1972), and (4) FAO Penman-Monteith (Allen et al. 1998).

In addition to allowing the users to prepare the RET time series as a model input, Macro-HyProS also offers three different RET computation options: (1) a simplified form of the

standard FAO Penman-Monteith method (Valiantzas, 2013), (2) a two-factor model (Oudin et al., 2005), and (3) Hargreaves and Samani (1985) equation. These options facilitate the selection of a suitable RET scheme based on the study area characteristics and availability of input data. Different RET computation options have various levels of complexity and input data requirements. Oudin et al. (2005) suggested that the models relying on solar radiation and mean daily temperature are as efficient as more sophisticated and data-demanding models and can be used in hydrologic models. Oudin et al. (2005) also suggested a simple two-factor RET model, which has been incorporated in Macro-HyProS:

$$RET = \begin{cases} \frac{R_e}{\lambda} \times \frac{T_{AVE}(t,g,k) + K_2}{K_1} & if\ T_{AVE} + K_2 > 0 \\ 0 & if\ T_{AVE} + K_2 \leq 0 \end{cases} \quad (2.2)$$

where λ is the latent heat flux (2.45 MJ m^{-2} day^{-1}), R_e corresponds to the extraterrestrial radiation (MJ m^{-2} day^{-1}), and K_1 and K_2 respectively are a scaling factor and a temperature threshold ranging from 90-115 and 5-6.

2.3.2.2. Vegetation Band

The Vegetation Band is responsible for computing the interception losses by plants. The macro-scale hydrologic models commonly employ a simple bucket approach to simulate interception losses. For example, SPHY (Terink et al. 2015) incorporates a time series of normalized difference vegetation index (NDVI) in a dynamic vegetation module to provide estimates of leaf area index (LAI) and maximum canopy storage. Eventually, the interception is calculated as a function of the stored water on the canopy and the atmospheric evaporation demand (Terink et al. 2015). HBV-96 incorporates a simple storage model only for forested areas (Lindström et al. 1994, 1997). In the storage model used in HBV-96, the maximum canopy storage of the forest is assumed to be constant during the year (Lindström et al. 1994). However, the majority of hydrologic models account for variable LAI during the year (e.g., SPHY and VIC).

Several studies have suggested that interception losses vary depending on the types of vegetation and precipitation characteristics (Kozak et al. 2007; Maidment 1993). Therefore,

Macro-HyProS accounts for rainfall and snowfall interception for (1) short vegetation (i.e., crops and residues) and (2) tall vegetation (i.e., forests). It should be noted that in each grid, all bricks within the Green Block except for the Forest Brick are considered as short vegetation bricks (Table 2.1). Particularly, rainfall interception is simulated for both short and tall vegetation bricks; however, snow interception is estimated only for high vegetation bricks, assuming negligible snow interception by short-vegetation areas.

Table 2.1. Descriptions of different bricks considered in the LEGO-fashion layout of Macro-HyProS based on the Food and Agriculture Organization (FAO) Indicative Crop Classification version 1.1.

Block	Brick #	Brick Name
Green	1	Cereals
	2	Vegetables and melons
	3	Fruit and nuts
	4	Oilseed crops and oleaginous fruits
	5	Root/tuber crops with high starch or inulin content
	6	Stimulant, spice and aromatic crops
	7	Leguminous crops
	8	Sugar crops
	9	Other crops
	10	Forest
	11	Grass/Pasture
Red	12	Developed
Blue	13	Lakes
	14	Depressions

2.3.2.2.1. Rainfall Interception by Short Vegetation

The significance of intercepted water by different crops has been highlighted in numerous studies (e.g., Baver, 1939; Kontorshchikov and Eremina, 1963; Lull, 1964). Lull (1964) showed that the interception losses accounted for 36%, 16%, and 15% of the total rainfall throughout the growing season for wheat, corn, and soybean, respectively. To account for the rainfall interception by short vegetation, Macro-HyProS uses a time-varying LAI-based method to compute the rainfall interception losses by crops during the growing season. In addition, the

rainfall interception losses by crop residues can be optionally simulated during the post-harvest period.

The water balance equation for the short vegetation bricks can be expressed as:

$$STG_{SV}(t,g,k) = STG_{SV}(t-1,g,k) + RAIN_{CAN}(t,g,k) - INTC_{CAN}(t,g,k) \quad (2.3)$$

where STG_{SV} is the short vegetation canopy storage (mm), $INTC_{CAN}$ is the incremental canopy interception (mm), and $RAIN_{CAN}$ is the incremental rainfall on the canopy (mm) that is estimated based on the time series of fractional vegetation cover (FVC):

$$RAIN_{CAN}(t,g,k) = FVC(t,g,k) \times RAIN(t,g,k) \quad (2.4)$$

where RAIN is the total incremental rainfall (mm), and FVC is the ratio of the vertical projection area of vegetation (leaves, stems, and branches) on the ground to the total vegetation area and is estimated based on LAI using an exponential relationship (Liang and Li 2012):

$$FVC(t,g,k) = 1 - e^{-0.5\,LAI(t,g,k)} \quad (2.5)$$

In Macro-HyProS, the growing season is divided into three periods, representing three different plant growth stages (Figure 2.5). The LAI values obtained from the literature (e.g., Mengel et al., 2001; Sellers et al., 1996) represent plants in their fully developed condition (i.e., maximum LAI). The LAI values for the two other stages are approximated based on two linear relationships (Figure 2.5). It is assumed that LAI increases linearly from the beginning of the growing season until reaching a plateau (maximum LAI) and then decreases linearly to the end of the growing season.

A simple storage method is used to account for the maximum canopy storage, in which the dynamic maximum canopy storage is approximated based on the estimated LAI time series (Von Hoyningen-Huene 1981):

$$MXSTG_{CAN}(t,g,k) = 0.935 + 0.498 \times LAI - 0.00575 \times LAI^2 \quad (2.6)$$

where $MXSTG_{CAN}$ is the maximum canopy storage (mm). The amount of water beyond $MXSTG_{CAN}$ is defined as the excess storage (STG_{EX}) and is expressed as:

$$STG_{EX}(t,g,k) = Max[0, STG_{SV} - MXSTG_{CAN}] \quad (2.7)$$

When the excess storage is removed from STG_{SV}, $INTC_{CAN}$ (mm) is then calculated by:

$$INTC_{CAN}(t,g,k) = Min[STG_{SV}, ATED] \quad (2.8)$$

where ATED is the atmospheric demand for open water evaporation and ATED = 1.5RET is suggested (Allen et al. 1998), assuming that $INTC_{CAN}$ is evaporated by the end of each day.

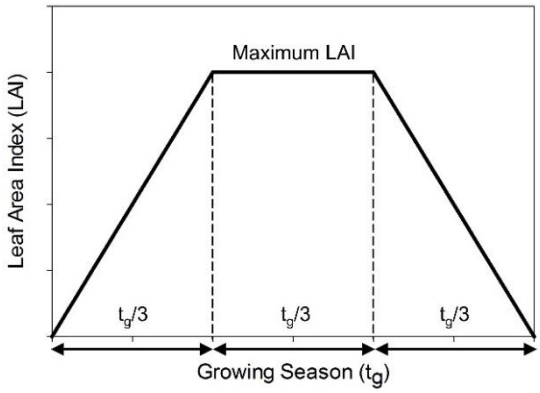

Figure 2.5. Leaf area index (LAI) variations throughout the growing season (t_g) in Macro-HyProS.

In addition to the interception by the canopy, different studies suggest that the rainfall interception losses by the crop residues are also a significant portion of the total rainfall (e.g., Mohamoud and Ewing, 1990; Savabi and Stott, 1994). As an option, a similar approach is used in Macro-HyProS to simulate the interception by crop residues for a user-defined period following the crop harvest. However, the maximum residue storage ($MXSTG_{RES}$) is approximated as a function of the total residue mass (Kozak et al. 2007; Savabi and Stott 1994):

$$MXSTG_{RES}(t,g,k) = \begin{cases} 346\,RM(t,g,k) - 10.5\,RM^2(t,g,k) & if\ corn \\ 370\,RM(t,g,k) - 11\,RM^2(t,g,k) & if\ soybean \\ 627\,RM(t,g,k) - 37.3\,RM^2(t,g,k) & if\ wheat \end{cases} \quad (2.9)$$

where RM (kg ha^{-1}) is the residue mass for corn, soybean, and wheat. Similarly, a generic empirical equation is employed to estimate $MXSTG_{RES}$ for other crops (Kozak et al. 2007).

2.3.2.2.2. Rainfall and Snowfall Interception by Tall Vegetation

The modified Gash model (Valente et al., 1997) was utilized in Macro-HyProS to estimate rainfall interception and evaporation for the forest canopy and trunks. The Gash model and its

variants are commonly used at a daily time step, assuming each day as a separate event (Miralles et al. 2010). In other words, the forest canopy is assumed to dry up completely between events (Carlyle-Moses and Gash 2011; Miralles et al. 2010; Valente et al. 1997). The rainfall interception losses from the forest canopy and tree trunks for each time step are estimated based on two critical rainfall values: the amount of rainfall to saturate the (1) forest canopy (CR_C); and (2) trunks (CR_T) (Valente et al. 1997):

$$INTC_{FRC}(t,g,k) = \begin{cases} FVC \times RAIN & RAIN < CR_C \\ FVC \times [CR_C + \rho \times (1-\varepsilon) \times (RAIN - CR_C)] & RAIN \geq CR_C \end{cases} \quad (2.10)$$

where $INTC_{FRC}$ is the amount of rainfall interception by the forest canopy (mm), ρ is a ratio of the mean evaporation rate to the mean rainfall rate for the saturated canopy condition, and ε is the fraction of trunk evaporation (0.02) (Miralles et al. 2010; Valente et al. 1997). In addition to the rainfall interception by the forest canopy, a similar equation by Valente et al. (1997) is used to estimate the amount of rainfall interception by tree trunks.

Moreover, Macro-HyProS uses a simple bucket approach to estimate snow interception and storage in forest canopies (Tahmasebi Nasab and Chu 2019a). Snow interception by tall vegetation is estimated by (Hedstrom and Pomeroy 1998; Pomeroy et al. 1998):

$$INTC_{SNO}(t,g,k) = C_{CU} \times [FCS_{MX} - SWE_F(t-1,g,k)]\left(1 - e^{-\frac{FVC \times SNOW(t,g,k)}{FCS_{MX}}}\right) \quad (2.11)$$

where $INTC_{SNO}$ is the amount of snow interception (mm), SNOW is the snowfall (mm of water equivalent), C_{CU} is a canopy unloading coefficient (~0.7), SWE_F is the snow storage water equivalent of the forest canopy (mm), and FCS_{MX} is the maximum forest canopy snow storage (mm). FCS_{MX} is usually estimated by using LAI and snow density (Pomeroy et al. 1998; Schmidt and Gluns 1991). Snowmelt from the forest canopy storage (M_F) is then simulated by using a standard temperature index method (Liston et al. 2006) based on daily average temperature and a constant melting factor.

2.3.2.3. Snow Band

Snowmelt is one of the significant elements of the annual streamflow in many cold climate regions around the world. In the western United States and Canada, for example, 50%-80% of the total streamflow is fed by the snowmelt contributions (Stewart et al. 2004). Traditionally, the majority of the available hydrologic models take advantage of either (1) energy balance methods (EBMs) or (2) temperature index methods (TIMs) (Leavesley 1989). EBMs require a wide variety of either simulated or observed meteorological datasets such as solar radiation, temperature, and wind speed, while TIMs simulate snowmelt using a single average temperature. The simplicity of TIMs has led to their popularity in macro-scale hydrologic models. WaterGap, HBV, SWAT, and SPHY are among macro-scale hydrologic models using TIMs in different forms (Alcamo et al. 2003; Arnold et al. 1998; Bergström 1992; Terink et al. 2015).

The Snow Band in Macro-HyProS simulates (1) snowpack water equivalent storage, (2) snowmelt, (3) rain-on-snow melt, and (4) refrozen meltwater. The simulated processes in the Snow Band are elaborated in detail by Tahmasebi Nasab and Chu (2019a, 2019b) and are summarized here. The Snow Band water balance equation can be expressed as:

$$STG_{SN}(t,g,k) = STG_{SN}(t-1,g,k) + C_{SN} \times SNOW_S(t,g,k) - M_A(t,g,k) \quad (2.12)$$

where STG_{SN} (mm) is the snowpack water equivalent storage, $SNOW_S$ is the snowfall (mm) after interception, M_A is the actual snowmelt (mm), and C_{SN} is a snowfall correction factor that varies within a range of 0.7-1.6 (Anderson 2002) and accounts for the losses from sublimation and redistribution (Anderson 2006).

Macro-HyProS incorporates a hybrid TIM (HTIM) (Tahmasebi Nasab and Chu, 2019a) to simulate daily snowmelt and refreezing. Different studies have indicated that when sub-daily temperatures fluctuate above or below the freezing temperature, the single-temperature TIM may fail to provide realistic snowmelt simulations (Tahmasebi Nasab and Chu 2019a; Žaknić-Ćatović et al. 2018). Therefore, Tahmasebi Nasab and Chu (2019a) proposed the modified

macro-scale HTIM to account for the effect of sub-daily temperature fluctuation around the freezing temperature. The proposed methodology employs daily maximum and minimum temperatures (T_{MAX} and T_{MIN}) and their occurrence timing to complement the original TIM, which is solely based on T_{AVE}. The daily snowmelt and refreezing can be respectively expressed as (Tahmasebi Nasab and Chu 2019a):

$$M(t,g,k) = \begin{cases} C_M \times T_{AVE}(t,g,k) \times \Delta t & T_{MIN} > 0 \;\&\; T_{MAX} > 0 \\ C_M \times \dfrac{T_{MAX}(t,g,k)}{2} \times \Delta t_{MLT} & T_{MIN} \le 0 \;\&\; T_{MAX} > 0 \end{cases} \tag{2.13}$$

$$R(t,g,k) = \begin{cases} C_F \times T_{AVE}(t,g,k) \times \Delta t & T_{MIN} \le 0 \;\&\; T_{MAX} \le 0 \\ C_F \times \dfrac{T_{MIN}(t,g,k)}{2} \times \Delta t_{RFR} & T_{MIN} \le 0 \;\&\; T_{MAX} > 0 \end{cases} \tag{2.14}$$

where M and R are the snowmelt (mm) and refreezing (mm), respectively; C_M and C_F are the melting and freezing factors (mm $^oC^{-1}$ day^{-1}); T_{AVE} is the daily average temperature (^oC) over time step Δt (day), T_{MAX} and T_{MIN} are the daily maximum and minimum temperatures (^oC), and Δt_{MLT} and Δt_{FRZ} are the effective melt and refreezing times and represent the fraction of the day in which the temperature is higher or lower than zero, respectively. The seasonal variations of C_M are also modeled by using a sinusoidal function (Fontaine et al. 2002; Neitsch et al. 2011) that considers the maximum and minimum melting factors (C_{MX} and C_{MN}) for different bricks. Specific values for bricks can be obtained from the existing literature (Anderson 2006; Neitsch et al. 2011).

The meltwater resulting from a rain-on-snow event, M_R (mm), is calculated only when there is a snowpack on the ground and precipitation is in the form of rainfall or mixed rainfall and snowfall. When precipitation occurs in the form of mixed rainfall and snowfall, the snowpack is first updated, followed by M_R calculations. Assuming that the snowpack surface temperature is 0 ^oC and the rainfall temperature is equal to T_{AVE} (Qi et al. 2017), M_R can be estimated by:

$$M_R(t,g,k) = 0.0126 \times T_{AVE}(t,g,k) \times ROS(t,g,k) \tag{2.15}$$

in which ROS is the amount of rainfall on snowpack (mm).

The amount of actual snowmelt (M_A) is estimated based on the total available water for melt, AWM (mm), and the maximum snowpack water retention storage, MXSPR (mm), as follows:

$$M_A(t,g,k) = Max[0,(AWM - MXSPR)] \quad (2.16)$$

in which AWM is the summation of meltwater from different sources (M_F, M_R, and M) minus the refrozen meltwater (R); MXSPR is a threshold for snowmelt generation. The snowpack water retention storage (SPR) retains meltwater until reaching MXSPR. In other words, MXSPR is a threshold to delay the generation of snowmelt. The water stored in SPR can refreeze when the temperature is below 0 ^oC, and MXSPR is computed as a fraction of snowpack water equivalent storage, STG_{SN} (mm):

$$MXSPR(t,g,k) = C_{WR} \times STG_{SN} \quad (2.17)$$

where C_{WR} is the coefficient of water retention storage, having a suggested value of 0.1 (Bergström 1992).

2.3.2.4. Surface Band

Macro-scale hydrologic models use different methodologies with varying levels of complexity to simulate surface runoff and infiltration. For example, SPHY uses a simple saturation excess surface runoff generation method in which surface runoff is a function of the water content and the saturated water content of the first layer of the soil (Terink et al. 2015). The VIC model employs the variable infiltration curve (VIC) scheme from the Xinanjiang model (Zhao et al. 1980) to simulate the generation of surface runoff. Although surface runoff is generated from the topmost soil layer in the Xinanjiang model, the VIC model assumes that surface runoff can be generated from the two upper soil layers when the soil storage exceeds the soil storage capacity (Liang et al. 1994).

The Surface Band water balance equation in Macro-HyProS can be expressed as:

$$STG_{DP}(t,g,k) = STG_{DP}(t-1,g,k) + RAIN_S(t,g,k) + M_A(t,g,k) - RUNF(t,g,k) - INFL(t,g,k) - E(t,g,k) \quad (2.18)$$

where STG_{DP} (mm) is the depression storage, $RAIN_S$ is the rainfall (mm) after interception, M_A is the actual melt (mm), RUNF is the generated surface runoff (mm), INFL is the infiltration (mm), and E is the evaporation (mm).

Macro-HyProS uses the SCS-CN method (USDA 1986) to simulate surface runoff and infiltration. The simplicity of the CN method makes it popular (Verma et al. 2017). However, the original CN method has some limitations. For example, it is only suitable for event-based hydrologic modeling. Therefore, over the course of the last four decades, a wide variety of enhancements have been proposed to improve its applicability (e.g., Ajmal et al., 2015; Michel et al., 2005; Neitsch et al., 2011). It has been shown that different factors are responsible for the CN variations, among which the antecedent moisture condition (AMC), soil type, land use, and slope are more pronounced (Verma et al. 2017).

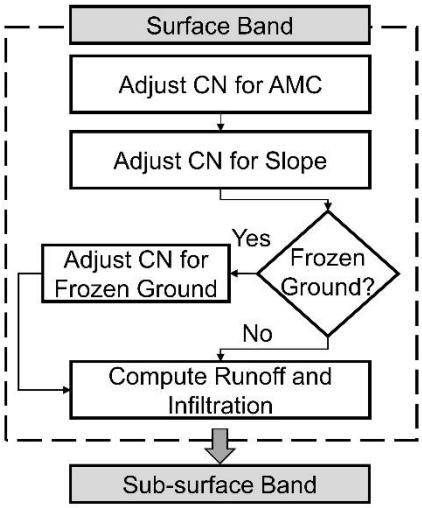

Figure 2.6. Simplified flow diagram of the Surface Band in Macro-HyProS.

The original CN values for each brick are determined based on the soil type and land use. Figure 2.6 shows a simplified flow diagram of the Surface Band's workflow. Before using the CN method for surface runoff simulation, the original CN values for different bricks are modified based on AMC, slope, and frozen ground condition (Figure 2.6). Macro-HyProS employs the

modification procedure by Neitsch et al. (2011) to adjust the CN values based on soil water content. To account for the grid-to-grid slope variations, Macro-HyProS offers three different CN adjustment options (Ajmal et al. 2016; Huang et al. 2006; Sharpley and Williams 1990) listed in Table 2.2. These three different equations provide the option of adjusting CN based on specific topographic features. In this study, the equation by Sharpley and Williams (1990) was used to adjust CN values.

Table 2.2. Slope (α) (m/m) adjusted curve number (CN_α) equations employed by Macro-HyProS (CN_1 and CN_3 are the CNs for antecedent moisture condition (AMC) I and III, respectively) (α represents the average slope of each grid).

Adjusted CN (CNα)	**Reference**
$CN_\alpha = \frac{1}{3}(CN_3 - CN_1)(1 - 2e^{-13.86\times\alpha}) + CN$	Sharpley and Williams (1990)
$CN_\alpha = CN\left(\frac{322.79 + 15.63 \times \alpha}{\alpha + 323.52}\right)$	Huang et al. (2006)
$CN_\alpha = CN\left(\frac{1.927 \times \alpha + 2.1327}{\alpha + 2.1791}\right)$	Ajmal et al. (2016)

The frozen ground condition is a common phenomenon in cold climate regions, which leads to the formation of the relatively impermeable soil surface and affects the generation of surface runoff. This condition is associated with the consecutive freezing temperature periods and high antecedent moisture condition (Chu et al. 2019). Macro-HyProS uses the continuous frozen ground index (CFGI) (Molnau and Bissell 1983) to calculate and locate the frozen ground condition. CFGI has a positive value, and as it increases, the likelihood of the frozen ground increases too. CFGI in Macro-HyProS is expressed as:

$$CFGI(t,g,k) = C_{DC} \times CFGI(t-1,g,k) - T_{AVE} \times e^{-0.4\times C_{SR}\times SNOD(t,g,k)} \quad (2.19)$$

where C_{DC} is a daily decay coefficient that controls the degradation of CFGI over time and takes the value of 0.97 (Molnau and Bissell 1983), and C_{SR} is a snow reduction coefficient (cm^{-1}) to account for the insulation effects of the snowpack. C_{DC} and C_{SR} are calibrated parameters and

their ranges are suggested by Molnau and Bissell (1983). SNOD is the depth of snow on the ground (cm) and is given by:

$$SNOD(t,g,k) = \frac{0.1 \times STG_{SN}}{\rho_s} \tag{2.20}$$

in which STG_{SN} (mm) is the snow water equivalent and ρ_s (g cm^{-3}) is the snow density. It is assumed that the impacts of snow compaction and destructive morphinism are negligible and ρ_s can be calculated solely by a function of average daily temperature (Anderson 2006).

A user-defined CFGI transitional range determines the impacts of frozen ground on the generation of surface runoff (Figure 2.7). For example, Molnau and Bissell (1983) suggested that the CFGI transitional range varies from 56 to 83. If CFGI is smaller than the lower CFGI threshold ($CFGI_{LT}$), the ground is not frozen (Figure 2.7), and the amount of surface runoff simulated by the modified CN model does not change. In contrast, if CFGI is greater than the upper CFGI threshold ($CFGI_{UT}$), the ground is completely frozen (Figure 2.7), and it is assumed that infiltration is minimal and CN is set to CN_{Frozen}. Finally, if CFGI is within the transitional range, the ground is partially frozen and a linear relationship is established between CFGI and CN, in which the CN for $CFGI_{UT}$ is 98.

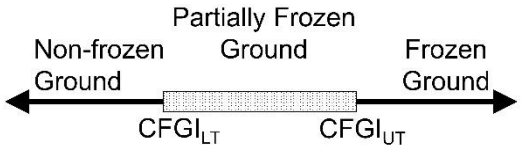

Figure 2.7. Classification of the ground freezing conditions (CFGI is the continuous frozen ground index, $CFGI_{LT}$ and $CFGI_{UT}$ are the lower and upper thresholds of the transitional range).

When surface runoff is calculated for each brick in a grid, an area-weighted approach is used to determine the surface runoff over the grid. This approach is superior to the traditional composite CN approach for estimating surface runoff (Mishra and Singh 2003). Eventually, infiltration into the Sub-surface Band is calculated by subtracting the generated surface runoff from the total input water to the Surface Band (i.e., ground rainfall + actual snowmelt).

2.3.2.4.1. Blue Block: Depressions and Lakes

Depression-dominated areas have a unique undulating topography, giving rise to many surface depressions that are periodically ponded and possess various functions such as flood mitigation, sediment retention, and habitat provision (Tahmasebi Nasab and Chu 2018). Macro-HyProS uses the Depression-dominated Delineation (D-cubed) method (Tahmasebi Nasab et al. 2017c) as a pre-processing tool to identify depressions and quantify their impacts. The D-cubed method provides a variety of features related to surface depressions such as depression storages, puddle levels, ponding areas, and contributing areas. These detailed features can potentially alter micro-scale hydrologic processes (Tahmasebi Nasab et al. 2016). In order to simulate depression-influenced hydrologic processes at a macro scale, Macro-HyProS incorporates the lumped contributing area to depressions and maximum depression storage for each grid. Figure 2.8 depicts a schematic representation of how the D-cubed results are incorporated into each grid as the Depressions Brick. As an example, Figure 2.8a shows the satellite image of a sample grid of 4×4 km² within the RRB (UTM coordinates of the grid center: 5,310,355 m, 501,855 m), in which depressions are mostly concentrated in the southeastern corner of the sample grid. Figure 2.8b indicates the spatial distribution of the contributing area to depressions, resulted from the D-cubed method. In other words, 100% of the generated surface runoff within the delineated contributing area contributes to the depressions. Eventually, the lumped contributing area of the depressions is incorporated into each grid as the Depressions Brick (Figure 2.8c).

The depression storage is updated based on the generated surface runoff at every time step. The amount of water that spills out of depressions is estimated based on two threshold storages: (1) the maximum depression storage ($MXSTG_{DP}$) and (2) the minimum spill threshold storage ($MNSTG_{DP}$):

$$SPIL(t,g,k) = \begin{cases} STG_{DP} - MXSTG_{DP} & STG_{DP} > MXSTG_{DP} \\ C_{DP} \times (STG_{DP} - MNSTG_{DP}) & MNSTG_{DP} < STG_{DP} \leq MXSTG_{DP} \\ 0 & STG_{DP} \leq MNSTG_{DP} \end{cases} \quad (2.21)$$

where SPIL represents the water that spills out of depressions (mm) and contributes to the generated surface runoff, and C_{DP} is a decay factor (0-1) that controls the flow of water out of depressions when they are partially filled. It should be noted that $MXSTG_{DP}$ values of the grids are obtained from the D-cubed surface delineation, and $MNSTG_{DP}$ values are defined as a fraction of $MXSTG_{DP}$ based on the study area.

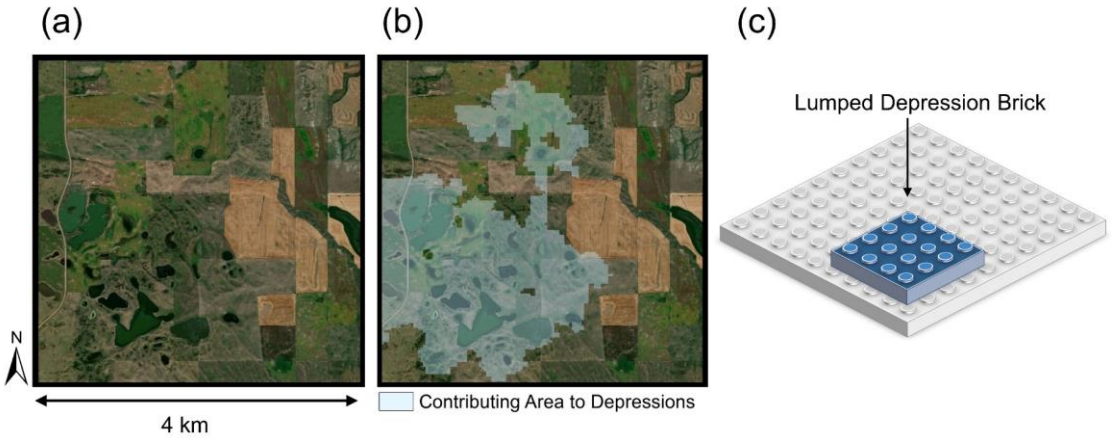

Figure 2.8. Schematic representation of the Depressions Brick in Macro-HyProS for a sample grid in the RRB (UTM coordinates of the grid center: 5,310,355 m, 501,855 m).

The evaporation from the depression storage is estimated based on RET and is expressed as:

$$E(t,g,k) = K_W \times RET(t,g,k) \tag{2.22}$$

in which K_W is the open water evaporation coefficient (Allen et al. 1998).

In addition, the amount of water that moves from the depression storage to the Sub-surface Band, SEEP (mm), is estimated according to the fraction full of the depression storage and the fraction empty of the sub-surface layer:

$$SEEP(t,g,k) = K_{S1} \times \frac{STG_{DP}(t,g,k)}{MXSTG_{DP}} \times (1 - \frac{\theta_{S1}(t-1,g,k)}{SAT_{S1}}) \tag{2.23}$$

where K_{S1} is the hydraulic conductivity of the sub-surface layer 1 (mm/day), θ_{S1} is the soil water content (m^3/m^3) of sub-surface layer 1, and SAT_{S1} is the soil saturated water content (m^3/m^3) of sub-surface layer 1.

It should be noted that the current version of Macro-HyProS does not account for lakes and their impacts on hydrologic processes. Therefore, the lake areas within each grid are obtained from different datasets (e.g., National Wetlands Inventory for the United States lakes) and are removed from the grid area.

2.3.2.5. Sub-surface Band

Macro-scale hydrologic models consider one or more layers to simulate different sub-surface processes. For example, the soil profile is represented by only one layer in WaterGap3 and HBV, whereas VIC, HYPE, and ECOMAG account for three layers of soil (Krysanova and Hattermann 2017). Depending on their physical representation of the soil layers, different models require the use of a varying number of soil parameters and characteristics. While some models require only a few soil parameters (e.g., five parameters in ECOMAG), others may demand more details (e.g., 19 parameters in VIC).

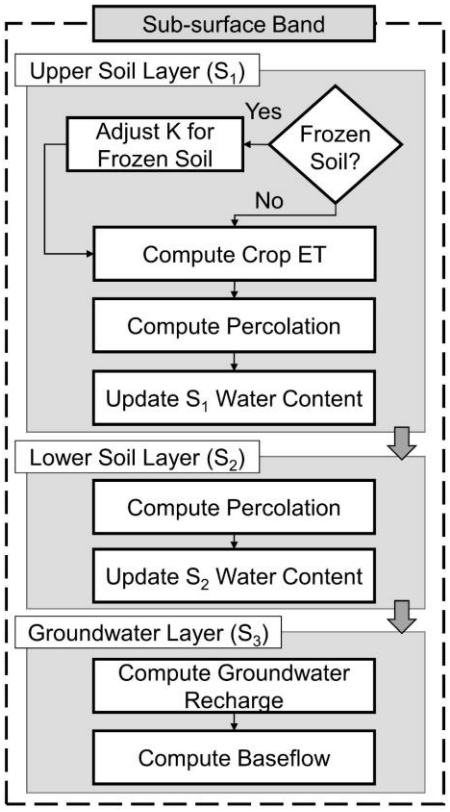

Figure 2.9. Simplified representation of the Sub-surface Band in Macro-HyProS: its three layers and simulated processes.

Sub-surface processes in Macro-HyProS are simulated in three sub-surface layers. Specifically, they schematically embody the sub-surface profile in which an upper soil layer (S_1) is responsible for surface-subsurface interactions and crop specifications, a lower soil layer (S_2) represents deep vadose zone, and an aquifer layer (S_3) controls the generated baseflow. Figure 2.9 illustrates a simplified workflow representation of the Sub-surface Band, its three layers, and the simulated processes. The water balance for layer S_1 can be expressed as:

$$STG_{S1}(t,g) = STG_{S1}(t-1,g) + INFL(t,g) - ET_{S1}(t,g) - PERC_{S1}(t,g) \quad (2.24)$$

where STG_{S1} is the storage of S_1 (mm), ET_{S1} is the evapotranspiration (mm) from S_1, and $PERC_{S1}$ is the percolation from S_1 to S_2 (mm).

In order to compute the percolation from S_1 to S_2, the unsaturated hydraulic conductivity (K_{S1}) is adjusted based on the frozen soil condition of a user-defined portion of layer S_1 (FRD), which represents the topsoil. Similar to what was described for the determination of the frozen ground in Surface Band (Figure 2.7), a continuous frozen soil index (CFSI) is used to determine the frozen soil condition. Particularly, two CFSI thresholds regulate the topsoil freezing condition: the upper threshold $CFSI_{UT}$, beyond which the topsoil is considered to be fully frozen and the lower threshold $CFSI_{LT}$, below which the topsoil is in a non-frozen condition. Also, the CFSI values between $CFSI_{LT}$ and $CFSI_{UT}$ are considered to be partially frozen. The adjusted K_{S1} for the frozen soil condition is then estimated by:

$$K_{S1}^{*} = \begin{cases} 0 & CFSI \geq CFSI_{UP} \\ 10^{-C_I \theta_{FR}} \times K_{SAT1} \times \left(\frac{\theta_{NFR}}{SAT_{S1}}\right)^{3+2\times b} & CFSI_{LT} < CFSI < CFSI_{UP} \\ K_{S1} & CFSI \leq CFSI_{LT} \end{cases} \quad (2.25)$$

in which K^{*}_{S1} is the adjusted hydraulic conductivity. If soil is partially frozen, an adjustment relationship (Jame and Norum, 1980) is employed, where K_{SAT1} is the saturated hydraulic conductivity (m/s), SAT_{S1} is the saturated water content, θ_{FR} and θ_{NFR} are the soil frozen and non-frozen water contents, C_I is an empirical factor that accounts for the impedance of ice (Shoop and Bigl 1997), and b is the Clapp-Hornberger constant (Jame and Norum 1980). The

frozen water content for partially frozen soils (i.e., θ_{FR}) is estimated by using a linear relationship that uses $CFSI_{LT}$ and $CFSI_{UT}$ to determine the frozen fraction.

The evapotranspiration is calculated based on the specific crop coefficients (K_C) for different plants during their growth stages (Allen et al. 1998):

$$ET_{S1}(t,g,k) = K_C(t,g,k) \times RET(t,g,k) \tag{2.26}$$

where ET_{S1} is the evapotranspiration (mm). ET_{S1} is first removed from a user-defined effective evapotranspiration depth (ETD), defined as a fraction of the upper soil layer's thickness. If ET_{S1} is greater than the available water in ETD, ET_{S1} is then removed from the rest of layer S_1.

The potential amount of percolation from S_1 to S_2 is estimated by using a function of the soil hydraulic conductivity, the fraction full of layer S_1, and fraction empty of layer S_2 (Bennett 1998):

$$MXPERC_{S1}(t,g) = K_{S1} \times \frac{\theta_{S1}(t,g)}{SAT_{S1}} \times (1 - \frac{\theta_{S2}(t-1,g)}{SAT_{S2}}) \tag{2.27}$$

where $MXPERC_{S1}$ is the potential percolation (mm) from S_1 to S_2, K_{S1} is the hydraulic conductivity (mm/day) of S_1, θ_{S1} and θ_{S2} are water contents of S_1 and S_2, and SAT_{S1} and SAT_{S2} are the saturated water contents of S_1 and S_2.

The actual percolation from S_1 to S_2 is then estimated based on the amount of available water for percolation and $MXPERC_{S1}$:

$$PERC_{S1}(t,g) = Min[MXPERC_{S1}, AWP_{S1}] \tag{2.28}$$

where AWP_{S1} is the available water for percolation (mm), which is calculated by the field capacity of S_1 (FC_{S1}):

$$AWP_{S1}(t,g) = \begin{cases} \theta_{S1} - FC_{S1} & \theta_{S1} > FC_{S1} \\ 0 & \theta_{S1} \leq FC_{S1} \end{cases} \tag{2.29}$$

The water balance equation used for layer S_2 is similar to the one for layer S_1. However, evapotranspiration from layer S_2 is assumed negligible. In addition, the percolation from S_2 to S_3 is estimated by using a similar set of equations used for determining the percolation from S_1 to S_2. When the percolation from S_2 to S_3 (i.e., $PERC_{S2}$) is computed, the groundwater recharge is

estimated by using an exponential relationship developed by Venetis (1969). This simple relationship has also been successfully used in different models, such as SWAT and SPHY:

$$GWR_{S3}(t,g) = \left(1 - e^{-\frac{1}{C_{GW}}}\right) \times PERC_{S2}(t,g) + e^{-\frac{1}{C_{GW}}} \times GWR_{S3}(t-1,g) \quad (2.30)$$

where GWR_{S3} is the groundwater recharge (mm) and C_{GW} is the delay factor (day). The water balance equation for S_3 (i.e., groundwater layer) is then expressed as:

$$STG_{S3}(t,g) = STG_{S3}(t-1,g) + GWR_{S3}(t,g) - BF_{S3}(t,g) \quad (2.31)$$

in which STG_{S3} is the storage of layer S_3 (mm), and BF_{S3} is the baseflow (mm), which is estimated based on a baseflow threshold (BF_{TH}) and a recession constant coefficient (C_{RC}) (Neitsch et al. 2011):

$$BF_{S3}(t,g) = \begin{cases} 0 & STG_{S3} \geq BF_{TH} \\ BF_{S3}(t-1,g) \times e^{-C_{RC}} + GWR_{S3}(t,g) \times (1 - e^{-C_{RC}}) & STG_{S3} < BF_{TH} \end{cases} \quad (2.32)$$

2.3.2.6. Flow Routing

Flow routing involves simulating water movement through the entire drainage network to the outlet of a watershed. The St. Venant equations offer a theoretical basis for flow routing; however, they require a variety of input data that are not usually available, especially for macro-scale modeling. Therefore, macro-scale hydrologic models typically employ simple routing methods that only account for flood wave delay and attenuation (Paiva et al. 2011). Similar to other macro-scale hydrologic models (e.g., VIC), Macro-HyProS performs a streamflow routing procedure after hydrologic processes are simulated for the entire simulation period. In other words, streamflow routing is performed separately from the simulation of hydrologic processes. When different processes are simulated, the contributing components to streamflow (i.e., surface runoff and baseflow) are summed up for each time step. This step generates a time series of matrices that account for the total contributing water from each grid:

$$Q_C(t,g) = 0.001 \times [RUNF(t,g) + BF_{S3}(t,g)] \times A^* \quad (2.33)$$

where Q_C is the grid-specific contributing flow (m^3) and A^* is the grid area after removing the lakes.

Macro-HyProS uses a simple routing method to route the grid-specific contributing flow to a user-defined outlet. The user-defined outlet is employed to determine the boundaries of the basin based on the input DEM. Specifically, a flow direction matrix of the study area is first computed to determine the direction of flow in a given grid. Then, the flow accumulation matrix of the study area is calculated which is a cumulative count of the number of grids draining into the downstream grid. The drainage network and the basin boundaries are eventually determined by employing the computed flow direction and flow accumulation matrices. In Macro-HyProS, a set of post-processing programs and the ArcPy package are used to route Q_C, employing flow direction and flow accumulation matrixes of the surface. Eventually, a linear reservoir routing method is used to account for the delay of flow from different grids to the outlet. This method has been incorporated and tested in SPHY and is expressed as (Terink et al. 2015):

$$Q(t) = (1 - C_{FR}) \times Q(t) + C_{FR} \times Q(t-1) \tag{2.34}$$

where Q is the discharge (m^3/s) at the outlet, and C_{FR} is a flow recession coefficient (0-1). It has been suggested that smaller C_{FR} values correspond to the faster basin response, whereas larger values represent the slower basin response (Terink et al. 2015).

2.3.3. Testing of Macro-HyProS in the RRB

The Red River of the North drains parts of Minnesota and Dakotas in the United States and flows into Lake Winnipeg in Canada. The RRB covers an area of 116,500 km^2, out of which 103,600 km^2 is within the United States (Figure 2.10a) (Red River Basin Board 2000). The annual average precipitation and temperature of the RRB are 500 mm and 4.3 ^oC, respectively (Jin et al. 2008), and the basin slope varies from 0.04 to 0.25 m/km. The majority of the RRB is within the Prairie Pothole Region that is featured with many depression-dominated areas and flat topography. The basin's topography can be divided into three elevation classes: (1) low, (2) moderate, and (3) high (Figure 2.10b), where the low-elevation Class 1 corresponds to the Red

River Valley, a prolific agricultural region in the northern United States. The agricultural areas dominate the RRB. Specifically, nearly 60% of the basin is covered by cultivated croplands, whereas only 4.5% of the basin is covered by developed areas (Figure 2.10c) (Tahmasebi Nasab et al. 2018).

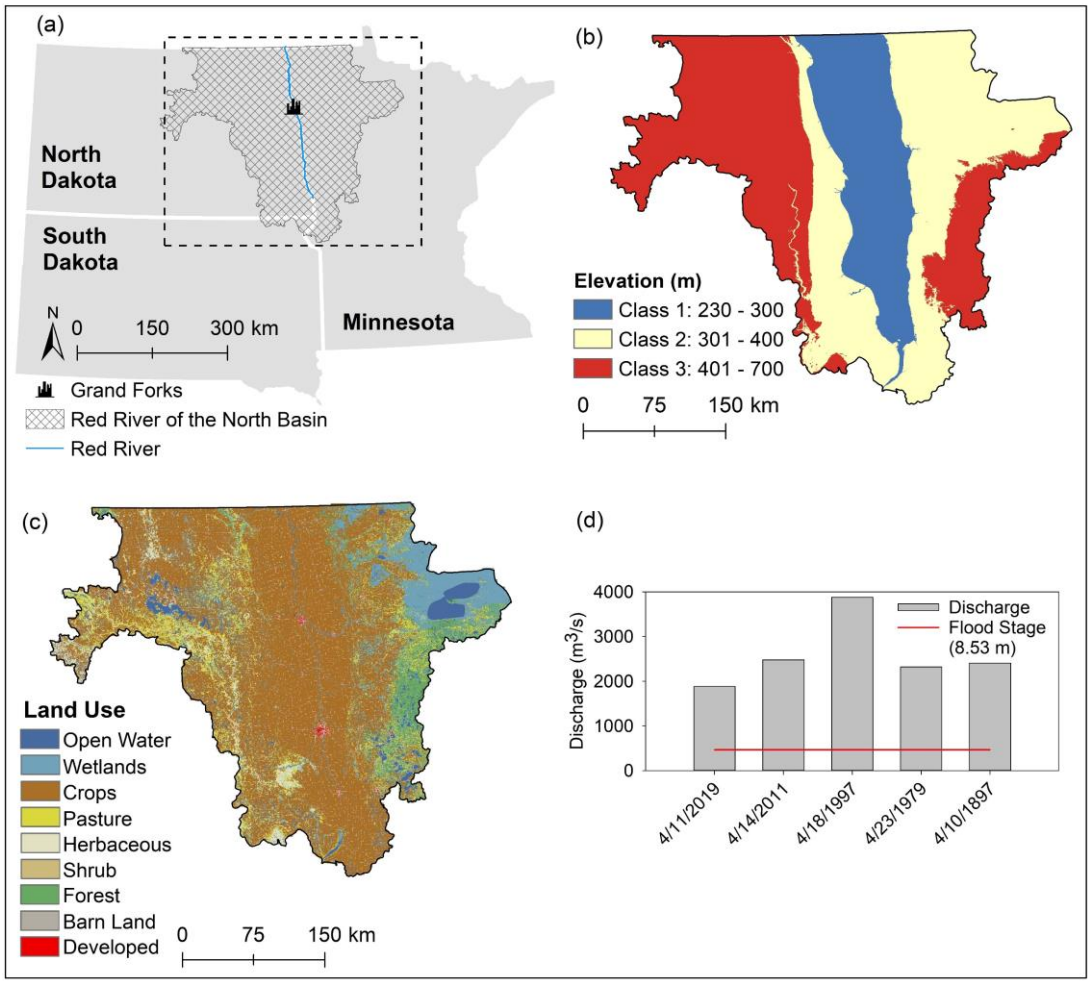

Figure 2.10. (a) Geographical location of the RRB (U.S. portion); (b) topographical variations, (c) land use variations, and (d) selected record-breaking floods.

The RRB possesses unique hydro-topographical features, which make it prone to the occurrence of frequent spring floods. In addition to its flat topography in the Red River Valley, RRB is categorized as a cold climate region having lingering cold winters. A combination of freezing temperatures and thick snowpack give rise to the frozen ground condition that lasts up to the spring when snow begins to melt. The concurring snowmelt and early spring rainfalls lead

to frequent floods in the RRB. Figure 2.10d highlights some of the record-breaking floods in the RRB at the United States Geological Survey (USGS) Grand Forks Station (station ID: 05082500), including the recent 2019 flood. The high snowfall during the winter of 1996-97 (96 inches of snow were recorded in Grand Forks) as well as the occurrence of a blizzard on April 5-6, 1997, led to the worst flooding in the RRB in more than 100 years (USGS 2019a). This trend has been repeating for many years in which the months of March and April play a significant role in the spring flooding condition (Figure 2.10d). The reoccurrence of the spring floods pinpoints the significance of the cold climate processes in the basin. Therefore, the RRB was selected for this study to highlight the capabilities of Macro-HyProS for depression-dominated, cold climate regions.

2.3.4. Model Setup and Input Data

The RRB (the U.S. portion, as shown in Figure 2.10a) was discretized into 6,351 grids of 4×4 km^2, and different hydrologic processes were simulated for each grid. Table 2.3 lists the major input data obtained from different sources. A 30-m digital elevation model (DEM) was obtained from the National Elevation Dataset (USGS 2019b) and was used for the D-cubed surface delineation (Tahmasebi Nasab et al. 2017c). The daily streamflow dataset at the Grand Forks station was also obtained from the USGS (2019c) for a selected 5-year period. The Cropland Data Layer (CDL) database (Boryan et al. 2011) (~30-m resolution) was used for the land use distribution and brick specification within each grid. Different meteorological data such as daily precipitation and daily temperature were obtained from the Parameter-elevation Regressions on Independent Slopes Model (PRISM) (Daly et al. 2008), and the Climate Forecast System Reanalysis (CFSR) (Fuka et al. 2012). The soil type data were extracted from the United States Department of Agriculture STATSGO2 database (NRCS 2018) using Soil Data Viewer 6.2 (Natural Resources Conservation Service 2015), which is a GIS extension to extract sub-surface information from STATSGO2 database. Also, different soil hydraulic parameters were obtained from the existing literature. Particularly, Chu et al. (2019) compiled different soil parameters for

use in a hydrologic model from different sources (e.g., Carsel et al. 1998; Maidment 1993; Rawls et al. 1982; Rawls and Brakensiek 1983). Other input data, such as LAI and crop-specific information, were also obtained from the existing literature as shown in Table 2.3.

Table 2.3. Input data and their sources utilized in Macro-HyProS (CDL: Cropland Data Layer, PRISM: Parameter-elevation Regressions on Independent Slopes Model, and CSFR: Climate Forecast System Reanalysis).

Dataset	Source	Reference
Digital Elevation Model	National Elevation Dataset	USGS (2019b)
Red River Discharge	USGS Water Data	USGS (2019c)
Land Use Distribution	CDL	Boryan et al. (2011)
Precipitation	PRISM	Daly et al. (2008)
Temperature	PRISM	Daly et al. (2008)
Solar Radiation	CFSR	Fuka et al. (2014)
Soil Type Distribution	USDA	NRCS (2018)
Soil Hydraulic Parameters	Literature	Chu et al. (2019)
Leaf Area Index	Literature	Sellers et al. (1996)
Crop Information	Literature	Allen et al. (1998)

A 5-year simulation period from 2003 to 2007 (1826 days) was selected, out of which 2003 was used as a warm-up period, 2004 and 2005 were used for model calibration, and 2006 and 2007 were utilized for model validation. Since the main objective of this study is to present the structure, methodology, and development of Macro-HyProS, the model parameters are manually calibrated and automated optimization schemes are not employed. The methods for simulating hydrologic processes in each band were meticulously selected to ensure the existence of adequate guidelines for initializing the model parameters in different regions. The parameters employed in Macro-HyProS and their acceptable variations were explained in Section 2.2 based on the existing literature. Table 2.4 lists the Macro-HyProS parameters for different bands, including their descriptions, spatial scales, and the calibration values/ranges. The Project for Intercomparison of Land surface Parameterization Schemes (PILPS) suggested that the calibration of macro-scale models against observed discharges improved the performance of the models (Wood et al. 1998). Hence, the Macro-HyProS results were compared against the observed discharges at the Grand Forks station (Figure 2.10a).

Table 2.4. Parameters used in different bands of Macro-HyProS.

Band	Parameter	Unit	Description	Spatial Scale	Value
Atmosphere	TT_{MAX}	^oC	Upper bound of TTR	Grid	5
	TT_{MIN}	^oC	Lower bound of TTR	Grid	1
	C_{HI}	-	Heat island effect coefficient	Brick	1
	C_{FC}	-	Forest canopy effect coefficient	Brick	1
	K_1	-	Scaling factor	Grid	5
	K_2	^oC	Temperature threshold	Grid	100
Vegetation	ρ	-	The ratio of mean evaporation rate to mean rainfall rate for saturated canopy condition	Basin	0.2
	ε	-	Fraction of trunk evaporation	Basin	0.02
	C_{CU}	-	Forest canopy unloading coefficient	Basin	0.7
	NGS	day	Growing season length	Basin	95
Snow	C_{SN}	-	Snowfall correction factor	Grid	0.96
	C_F	mm $^oC^{-1}$ day^{-1}	Freezing factor	Grid	0.05
	C_{MX}	mm $^oC^{-1}$ day^{-1}	Maximum melting factor	Brick	0.5-8
	C_{MN}	mm $^oC^{-1}$ day^{-1}	Minimum melting factor	Brick	0.2-3
	C_{WR}	-	Water retention storage coefficient	Basin	0.1
Surface	CN	-	Curve Number	Brick	58-98
	λ	-	Initial abstraction coefficient	Basin	0.15
	C_{DC}	-	Daily frozen ground decay coefficient	Basin	0.97
	C_{SR} *	cm^{-1}	Snow reduction coefficient	Grid	0.5, 0.08
	$CFGI_{LT}$	-	Lower CFGI threshold	Grid	56
	$CFGI_{UT}$	-	Upper CFGI threshold	Grid	83
	CN_{Frozen}	-	Frozen ground CN	Grid	98
	C_{DP}	-	Decay factor depressions	Grid	0.5
	K_w	-	Open water evaporation coefficient	Basin	0.7
Sub-surface	FRD	mm	Frozen ground depth	Grid	40
	$CFSI_{LT}$	-	Lower CFSI threshold	Grid	56
	$CFSI_{UT}$	-	Upper CFSI threshold	Grid	83
	b	-	Clapp-Hornberger constant	Grid	4.05-11.4
	K_C		Crop-specific evapotranspiration coefficient	Brick	0.3-1
	C_{GW}	day	Groundwater delay factor	Basin	10
	C_{RC}	day^{-1}	Baseflow recession constant	Basin	0.015
	ETD	mm	Effective evapotranspiration depth	Grid	2000

* Two values are used for temperatures higher and lower than the freezing temperature

In addition to the graphical comparisons, the model performance was evaluated by using the Nash-Sutcliffe efficiency coefficient (NSE) and following the recommended criterion for satisfactory performance for daily time steps (NSE > 0.5) (Moriasi et al. 2007, 2015). In addition to NSE, the model performance was evaluated by using the Kling-Gupta efficiency (KGE) (Gupta et al. 2009), which has been widely used to evaluate the performance of macro-scale hydrologic models (e.g., Beck et al., 2016) and facilitate the assessment of different components of the

performance of hydrologic models such as timing, magnitude, and variability (Gupta et al. 2009):

$$KGE = 1 - \sqrt{(r-1)^2 + (\alpha-1)^2 + (\beta-1)^2} \quad (2.35)$$

where r is the linear correlation coefficient between the simulated and observed values, α is a ratio between the standard deviation of the simulated and observed data to measure the relative variability of simulations, and β is a ratio between the mean simulated and observed values to represent the bias in simulations (Gupta et al. 2009). KGE ranges from $-\infty$ to 1, in which KGE = 1.0 represents the perfect match. Following Rogelis et al. (2016), the model performance can be classified into poor (KGE < 0), intermediate (0.5 < KGE < 0.75), and good (KGE > 0.75).

2.4. Results and Discussion

Figure 2.11 depicts the daily, monthly, and yearly graphical comparisons between the simulated and observed discharges (m^3/s) at the Grand Forks gauging station. A visual assessment for the daily discharges (Figure 2.11a) indicates that Macro-HyProS provided a comparable estimation of the streamflow variations in both cold and warm months. The NSE coefficients for the calibration and validation periods were 0.56 and 0.72, respectively, indicating satisfactory model performance (Moriasi et al. 2007, 2015). In addition to NSE, KGE values for the calibration and validation periods were 0.59 and 0.57, respectively, falling into the intermediate model performance group. Further statistical analysis of the entire simulation period indicated that the model was able to estimate 65% of the variability of streamflow discharge (α) as well as a linear correlation coefficient (r) of 0.75, suggesting a positive strong linear relationship between the simulated and observed discharge values. Although the model was able to successfully simulate the variations in the discharge patterns during low- and high-flow periods, it underestimated the peak discharge values. This can be attributed to the hydroclimatic nuances between different years throughout the simulation period and their impacts on the calibration process. For example, ~50% of the average precipitation over the basin in March 2006 occurred in the last five days of March and led to the highest observed peak

discharge, which was nearly two times higher than the peak discharge values in 2004 and 2005. Since the model was calibrated for 2004 and 2005, it might not capture the peak discharge in 2006. In addition to the daily discharge, Figure 2.11b illustrates a graphical comparison between the monthly simulated and observed discharges, indicating that the model provided satisfactory monthly results (R^2=0.81). However, it slightly underestimated low discharges and overestimated high discharges. For the annual average discharges, the average error percentage between the observed and simulated values is less than 15% (Figure 2.11c).

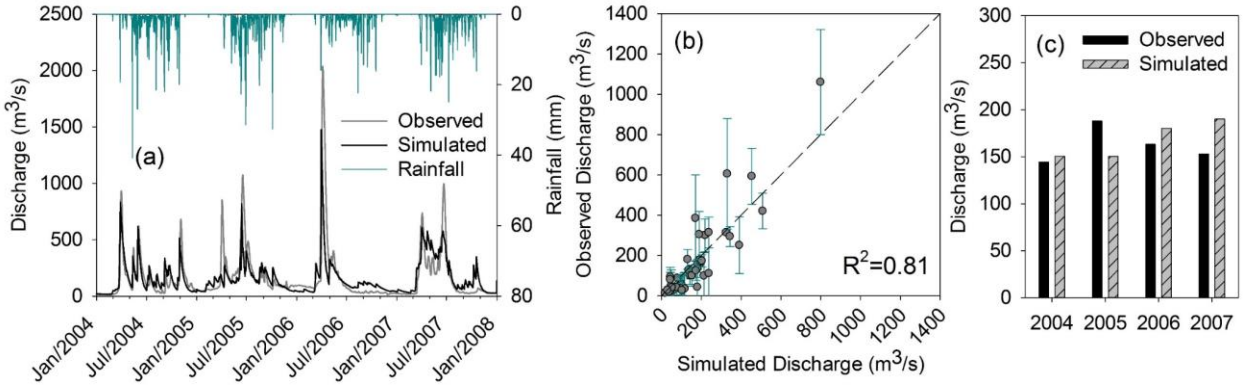

Figure 2.11. Comparison of the observed and simulated discharges at the Grand Forks gauging station (station ID: 05082500): (a) daily discharge, (b) monthly discharge (the error bars are the absolute difference between simulated and observed values), and (c) mean annual discharge (R^2 denotes the coefficient of determination).

2.4.1. How Does the Cold Climate Condition Alter Hydrologic Processes?

Figure 2.12a demonstrates the impacts of frozen ground on the generation of surface runoff in the RRB throughout the simulation period. The results from the CFGI method in Macro-HyProS can be used to determine the frozen ground condition (i.e., frozen, partially frozen, and non-frozen) and its spatial distribution. The results indicated that 2004, 2005, 2006, and 2007 respectively experienced 65, 43, 0, and 82 days in which the entire basin's ground (6,351 grids) was frozen. In addition to the 100% frozen ground condition, the RRB experienced partially frozen grounds in 105, 89, 135, and 63 days in 2004, 2005, 2006, and 2007, respectively. The presence of the frozen and partially frozen ground conditions in the basin played a significant role in the early spring surface runoff generation. Figure 2.12a

indicates that the ending period of the frozen ground condition in each year coincided with the occurrence of a significant amount of surface runoff in the basin. Further analysis revealed that the period from the end of March to early April was crucial for the frozen-ground induced snowmelt runoff in the RRB, which also coincided with the early spring rainfalls. The red box in Figure 2.12a pinpoints a critical four-month period in 2006 (i.e., January to May 2006), in which the frozen ground condition led to the generation of high surface runoff. On January 1st 2006, 77.1% of the basin was covered by the frozen and partially frozen ground; however, this number began to decline right after its peak in January (indicated by the red box in Figure 2.12a). As a consequence of the decline, 26.5% and 14.35% of the basin experienced fully and partially frozen ground, respectively, on March 31st, 2006.

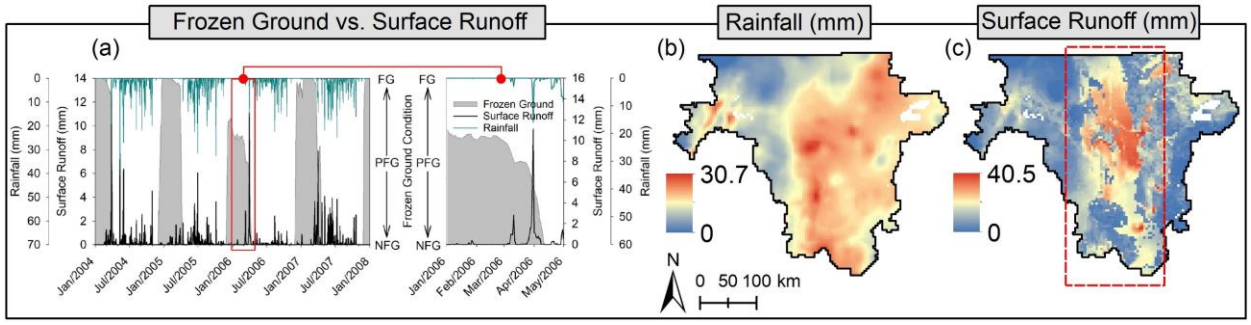

Figure 2.12. Impacts of the frozen ground on the generation of surface runoff in the RRB: (a) simulated frozen ground and surface runoff, (b) rainfall distribution on 3/31/2006, and (c) surface runoff distribution on 3/31/2006 (FG: frozen ground, PFG: partially frozen ground, and NFG: non-frozen ground).

On the same day, the RRB received a significant amount of rainfall (Figure 2.12b) mostly concentrated on the central and eastern parts of the basin, having an average of 15.97 mm. The combination of the frozen ground condition and heavy rainfall, together with the average snowmelt of 4.51 mm on March 31st, 2006 led to the generation of 11.1 mm of surface runoff over the basin (Figure 2.12c). The aforementioned process for 2006 is a typical example of early springs in the RRB, which leads to frequent spring floods with varying levels of severity. Figures 2.12a-c highlight the capability of Macro-HyProS in simulating the spatially-distributed cold climate hydrologic processes that facilitate a better understanding of the basin's dynamics in

early springs. In addition, the spatial distribution of the surface runoff on March 31st, 2006 highlights the high amount of surface runoff generated in the Red River Valley (indicated by the dashed red box in Figure 2.12c). This pattern is in accordance with the soil type distribution of RRB, in which the central region (i.e., Red River Valley) is dominated by finer soil types, causing higher surface runoff and lower infiltration (Chu et al. 2019).

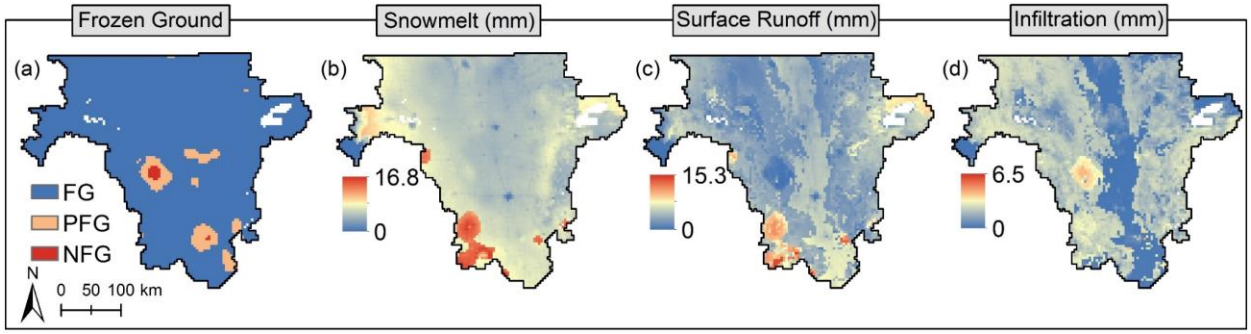

Figure 2.13. Simulation results for 3/13/2007: (a) frozen ground, (b) snowmelt (mm), (c) surface runoff (mm), and (d) infiltration (mm) (FG: frozen ground, PFG: partially frozen ground, and NFG: non-frozen ground).

In addition to early spring rainfall, snowmelt played a critical role in the generation of surface runoff in the RRB. To highlight the significance of snowmelt, Figure 2.13 depicts the simulated frozen ground condition, snowmelt, surface runoff, and infiltration on a sample day (i.e., March 13th, 2007), in which the average temperature across the basin was 3.1 °C with a standard deviation of 1.5 °C. Although the average basin temperature was above the freezing temperature (i.e., 0 °C), the results indicated that 98.4% of the basin (i.e., 6,248 grids out of 6,351 grids) experienced either frozen ground or partially frozen ground conditions (Figure 2.13a). The widespread extent of the frozen ground condition on March 13th, 2007 gave rise to susceptible circumstances for the generation of higher surface runoff. The frozen ground condition also coincided with an average snowmelt of 6.04 mm over the basin (Figure 2.13b), leading to higher surface runoff and lower infiltration (Figure 2.13c and Figure 2.13d). It was noticeable that due to the frozen ground condition over the basin, more than 60% of the generated snowmelt contributed to surface runoff, whereas infiltration had a smaller portion of

the generated snowmelt. The average surface runoff and infiltration simulated for March 13th, 2007 were 3.68 mm and 2.19 mm, respectively, highlighting the importance of snowmelt in the RRB. The pattern of frozen-ground-induced surface runoff depicted in Figure 2.13 is also typical for the RRB, especially on the days when the average temperature is above the freezing temperature, but the frozen ground condition persists.

2.4.2. Impacts of Snow Accumulation and Ablation Processes on Red River Flow

The distribution and magnitude of the snowmelt generated in the RRB have a direct relationship with the available snowpack. The snow accumulation process in the RRB generally begins around late November and early December. The gradual snow accumulation continues until late March and early April when higher than freezing temperatures initiate the snowmelt process throughout the basin. The simulation results showed that the model was able to capture the snow accumulation and ablation processes in different years. Figure 2.14a compares the magnitudes of the simulated snowpack water equivalent (hereafter called snowpack) and snowmelt in the RRB. Figure 2.14a suggests that the peak snowmelt values typically occurred right after the peak snowpack values. Although different years shared a similar snow accumulation and ablation trend, the magnitude of the simulated snowmelt varied from year to year, particularly in late March. These variations can be attributed to the hydroclimatic variations in different years. For example, 2006 accounted for the most amount of snowpack throughout the simulation period, having a maximum of 41.21 mm on March 6th, 2006 when 95.9% of the basin was covered by snow. Figure 2.14b highlights the snowpack-snowmelt dynamics for a 4-month period in 2006 (i.e., January to May 2006), in which the snowpack decreased with the occurrence of snowmelt events. The average temperature in the last five days of March 2006 was ~3 ^{o}C, leading to the highest snowmelt peak. Specifically, the average snowmelt across the basin in a 12-day period from 3/25/2006 to 4/5/2006 was 32.26 mm (Figure 2.14b). The sudden ablation of snowpack and the resulting snowmelt, as well as the

frozen ground condition at the end of March, led to the highest peak discharge (2,033.14 m^3/s) in the Red River at the Grand Forks station on 4/5/2006.

Moreover, the spatially distributed snowpack results confirmed the roles of snow accumulation and ablation processes in the peak discharges in late March and early April. Figure 2.15 shows the comparison of the average simulated snowpack and snowmelt in March when the average temperature was -2.86 ^oC, -4.27 ^oC, -3.55 ^oC, and -2.11 ^oC in 2004, 2005, 2006, and 2007, respectively. A visual comparison of the distributions of snowpack in March for different years reveals that the northern parts of the RRB experienced more snow than the southern parts (Figure 2.15a-d). In addition, Figure 2.15c clearly shows that 2006 had a higher snowpack in March than other years. This is partly attributed to the variations in snowfall in different years. For instance, 2006 received 7.5% more snowfall than 2007, which resulted in a discrepancy of 2.1 mm between the average simulated snowpack values over the basin in the two years. The average snowpack simulated for the RRB in March 2006 was 32.79 mm (corresponding to 3,331 Mm^3 of water), which is 2.1, 3.5, and 1.9 times greater than those in 2004, 2005, and 2007, respectively (Figure 2.15a-d).

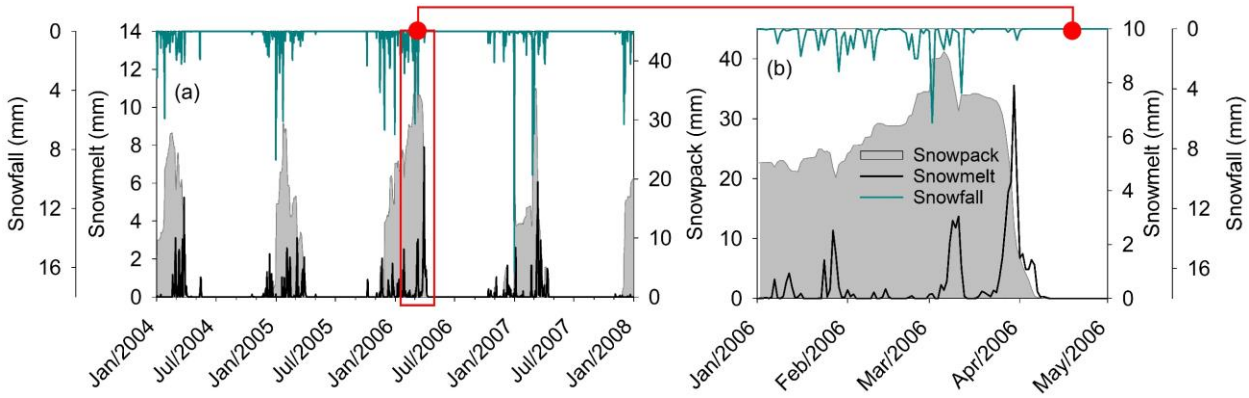

Figure 2.14. (a) Relationship between the simulated snowpack water equivalent (snowpack) and snowmelt in the RRB, (b) snowfall-snowpack-snowmelt dynamics for a 4-month period in 2006 (January - May).

Reasonably, higher snowpack in 2006 affected other hydrologic processes such as snowmelt, surface runoff, and infiltration. Throughout the simulation period, March had the highest snowmelt for all years. Figure 2.15e-h depict the impacts of snowpack in March on the

simulated snowmelt for different years. As expected, March 2006 experienced more snowmelt than other years. High snowmelt values in 2004, 2006, and 2007 were most noticeable in the northern and northwestern sides of the basin (Figure 2.15e, f, and Figure 2.15h), whereas the eastern side of the basin was mainly responsible for the high snowmelt in 2006. The average snowmelt over the basin in March 2006 was 1.3 mm, which is 22%, 94%, and 3.17% higher than the snowmelt in March 2004, 2005, and 2007.

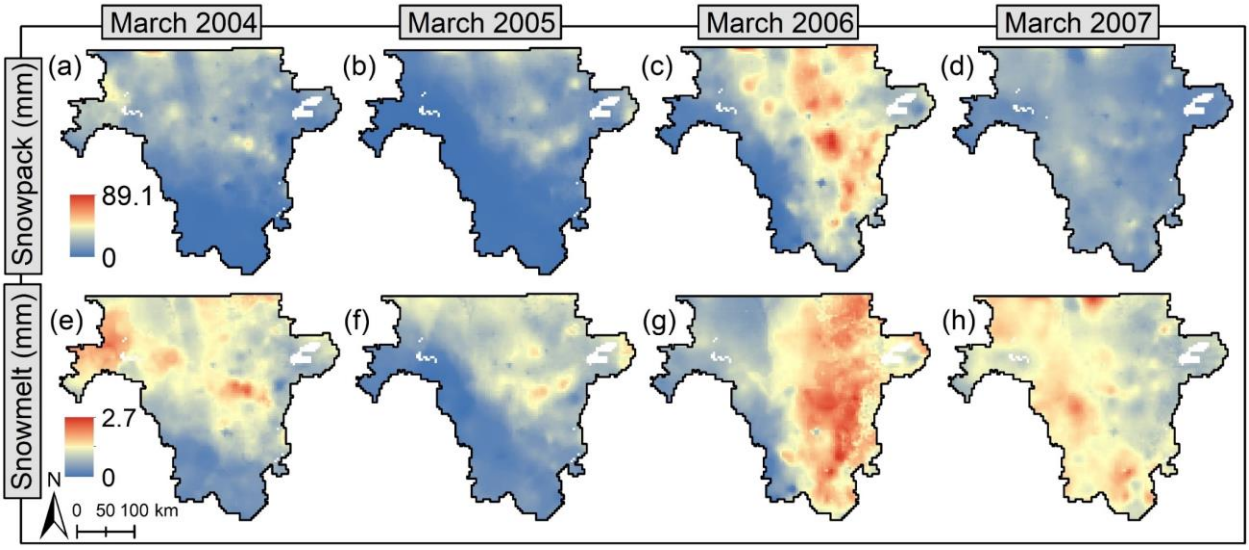

Figure 2.15. Snowpack water equivalent (mm) (snowpack) distribution in March (a) 2004, (b) 2005, (c) 2006, (d) 2007; and snowmelt (mm) distribution in March (e) 2004, (f) 2005, (g) 2006, (h) 2007.

2.4.3. How do Depressions Alter Hydrologic Processes?

Studies have suggested that the abundance of surface depressions in the RRB altered the generation of surface runoff (Tahmasebi Nasab et al. 2018). The simulation results from Macro-HyProS highlighted the critical role of depressions as "regulators," specifically in the early spring period. Figure 2.16a depicts the relationship between the temporal distribution of the depression storage and the generated surface runoff. It can be observed that the highest depression storage in different years occurred in late March and early April. Particularly, the amount of depression storage in the basin peaked on March 28th 2004, March 25th 2005, March 31th 2006, and April 1st 2007, when the basin experienced partially frozen ground, increased

snowmelt, and early spring rainfall (as shown in Figure 2.12). Figure 2.16a also indicates the connection between depression storage and evaporation from the stored water. As expected, the highest evaporation usually occurred in the period from June to August. The magnitude of the simulated evaporation showed a direct relationship to the depression storage. For example, since more water was stored in depressions in 2007, the total simulated evaporation from the ponded water in 2007 was 1.7 times higher than that in 2006.

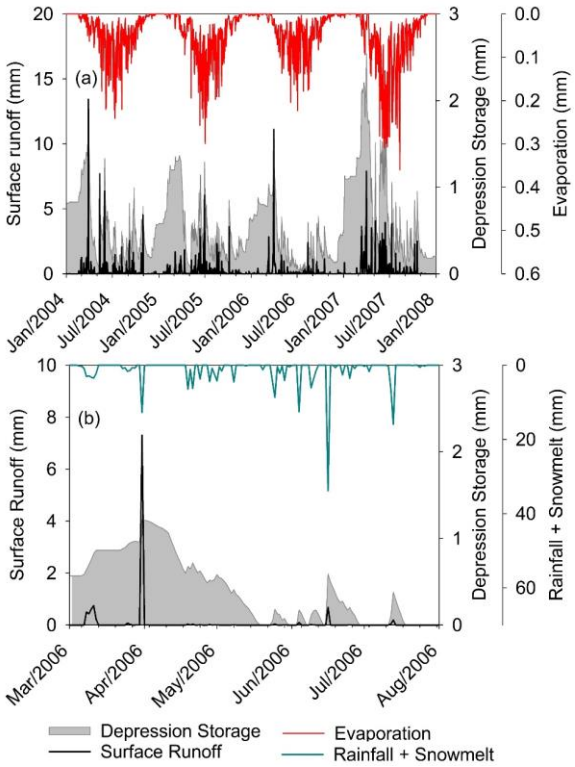

Figure 2.16. Connections between the temporal distribution of depression storage and different hydrologic processes for (a) RRB and (b) sample grid shown in Figure 8.

Figure 2.16b highlights the variations of depression storage over a 5-month period in 2006 (i.e., March-August) for the sample grid in the RRB shown in Figure 2.8. As aforementioned, the majority of depressions in the sample grid are concentrated in the southeastern corner of the grid (Figure 2.8b). Surface delineation results indicated that the maximum depression storage of the grid was 8.7 Mm^3 (corresponding to 5.4 cm of water over the grid) and ~24% of the grid area contributed runoff to the depressions. Since nearly one-

fourth of the basin contributed to depressions, even small rainfall or snowmelt events led to noticeable variations in the depression storage of the grid (Figure 2.16b). The depression storage had an increasing trend up to the end of March when its peak coincided with the peak runoff on 3/31/2006. Afterward, the depression storage followed a declining trend with intermittent fluctuations due to small rainfall events, and completely dried up on 5/19/2006. From this point forward, depressions were only periodically ponded and dried up, depending on the rainfall events (Figure 2.16b).

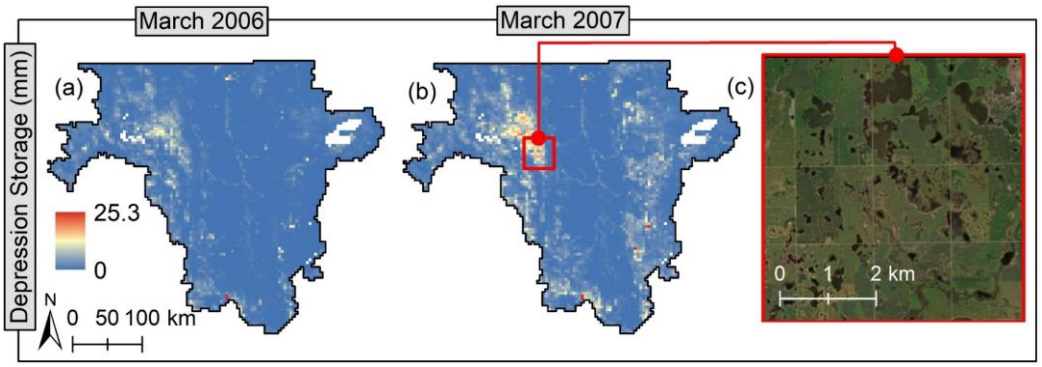

Figure 2.17. Spatial distributions of depression storage in the RRB: (a) March 2006, (b) March 2007, and (c) a satellite imagery of a focused area in the RRB featured with surface depressions.

In addition to the temporal distribution of the depression storage in the RRB, Marco-HyProS also provided spatial variations of the depression storage. Figure 2.17 shows the variations of depression storage in March 2006 and 2007, which had the highest depression storage among other months in these two years. Figures 2.17a and 2.17b indicate that the basin had higher depression storage values in the eastern and western parts, in comparison to the central part. This pattern is in accordance with other studies in the RRB. For example, Tahmasebi Nasab et al. (2018) divided the RRB into 146 subbasins and performed surface delineation to determine the maximum depression storage of the basin. It was observed that the central part of the basin generally accounted for lower depression storage, and depression storage increased from the central part to the eastern and western sides of the basin (Tahmasebi Nasab et al. 2018). Figure 2.17c shows a focused area of the basin that accounted for higher

depression storage in both 2006 and 2007. The satellite image presented in Figure 2.17c confirms the abundance of surface depressions over this focused area. The average depression storage values in the RRB in March 2006 and 2007 were 0.92 mm and 1.84 mm, respectively. The higher depression storage in March 2007 can be directly attributed to 4.89 mm more precipitation than that in March 2006.

2.4.4. Macro-HyProS in Perspective: Contributions, Limitations, and Potentials

Hydrologic modeling at macro-scale basins around the world is becoming increasingly popular to quantify the critical impacts of climate-driven changes on ecological, agricultural, and human behavioral aspects of water resources (Byun et al. 2019). Flexibility to grid structure is one of the important elements of macro-scale hydrologic models (Kauffeldt et al. 2016), enabling the models to take advantage of widely available grid-based reanalysis and earth observation datasets (Rodríguez et al. 2019). In addition to incorporating a grid-based structure, Macro-HyProS uses a novel LEGO-fashion horizontal layout to account for sub-grid heterogeneity based on the land use and land cover maps. The response of macro-scale cold climate basins to the projected warming climate trends are poorly known (Musselman et al. 2017). To provide a holistic understanding of cold-climate conditions through hydrologic simulations, Macro-HyProS incorporates a set of methodologies to simulate frozen ground and snow accumulation and ablation processes. Moreover, it has been shown that the collective effects of surface depressions can manipulate the response of macro-scale basins (Tahmasebi Nasab et al. 2017b, 2018). Therefore, Macro-HyProS utilizes a topography-based approach to account for the influences of surface depressions on macro-scale hydrologic processes such as surface runoff. The consideration of complexities associated with depression-dominated areas and cold climate regions makes the model a proper choice for applications in regions with similar hydro-topographical characteristics.

Although the current version of Macro-HyProS presents a novel structure and improved methodologies to simulate hydrologic processes for depression-dominated and cold climate

regions, improvements are foreseen in processes representation and calibration and evaluation processes. Particularly, the current version of Macro-HyProS incorporates a simple "leaky bucket" approach to simulate sub-surface processes. The merit of this simple approach is the low input data requirements, which makes it suitable for macro-scale models. However, since more spatially distributed datasets are becoming available, improvements in the Macro-HyProS Sub-surface Band can enhance its capabilities to simulate sub-surface processes. Since the major objective of this study was to present the theoretical foundation of the Macro-HyProS, a mechanistic approach was employed to provide a holistic understanding of the model's structure and methodology. However, future long-term applications of Macro-HyProS will center on calibration and evaluation of the model using not only streamflow discharge but also other hydrologic processes such as snowmelt. This multi-process calibration/evaluation will result in a better indication of the model's behavior within different bands.

2.5. Summary and Conclusions

This study presented the theoretical foundation of the Macro-scale Hydrologic Processes Simulator with the primary objective of simulating hydrologic processes in cold climate regions and depression-dominated terrains. Macro-HyProS is a grid-based daily hydrologic model that takes advantage of a unique LEGO-fashion horizontal layout to account for the within-grid variabilities of land use and land cover. Each grid in the model is conceptualized as a LEGO plate, on top of which three Blocks (Red, Green, and Blue - RGB) are placed, representing the developed, vegetated, and wetted areas. Macro-HyProS incorporates five vertical bands (Atmosphere, Vegetation, Snow, Surface, and Sub-surface Bands), each of which simulates different hydrologic processes. To accommodate the complexities associated with the depression-dominated terrains and cold climate regions, the model uses improved methodologies that are developed for macro-scale modeling of hydrologic processes. Eventually, a simple routing method is used to compute the outlet discharge. The model was applied to the Red River of the North Basin, which is characterized by its cold climate and depression-

dominated topography, for a 4-year period (1,461 daily time steps) from January 1st 2004 to December 31st 2007. The simulated hydrograph was compared against the observed one and the model performance was evaluated. Moreover, the capabilities of the model in simulating the spatiotemporal variations and trends of different hydrologic processes were showcased in forms of temporally and spatially distributed results.

The simulated discharges were in good agreement with the observed data, having the Nash–Sutcliffe efficiency coefficient of 0.56 and 0.72 for the calibration and validation periods, respectively. The modeling results indicated that the RRB experienced frozen or partially frozen ground conditions on an average of 145 days per year (i.e., 40% of the year). The frozen ground condition often coincided with the early spring rainfall and snowmelt events and altered the magnitude and distribution of the generated surface runoff and infiltration. It was demonstrated that the period between late March and early April was a critical one for the frozen-ground-induced spring floods across the simulation period. Also, the results indicated that the snow accumulation and ablation, synchronized with the frozen or partially frozen ground condition, produced peak discharge in the Red River. The snowmelt analysis suggested that up to 60% of the generated snowmelt contributed to surface runoff due to the widespread frozen ground condition. Macro-HyProS employed macro-scale methodologies to account for the lumped impacts of depressions and their contributing areas within each grid. The results revealed that the depression-dominated areas within the RRB acted as surface runoff regulators, specifically in the periods when a high amount of surface runoff was generated (i.e., late March and early April).

The modeling results from Macro-HyProS accentuated the significance of considering the unique cold-climate processes and the dominated role of surface depressions in hydrologic modeling. By using the improved methodologies and a unique LEGO-fashion layout, Macro-HyProS provides a better understanding and representation of macro-scale hydrologic processes. Although the current version of Macro-HyProS resulted in satisfactory simulations in

the RRB, further model applications in other macro-scale basins are necessary to test different features of the model. Also, long-term model evaluation and sensitivity analysis of the model parameters are foreseen to provide a clear understanding of different bands, used to simulate hydrologic processes.

2.6. References

Ajmal, M., Waseem, M., Ahn, J.-H., and Kim, T.-W. (2016). "Runoff Estimation Using the NRCS Slope-Adjusted Curve Number in Mountainous Watersheds." *Journal of Irrigation and Drainage Engineering*, 142(4), 04016002.

Ajmal, M., Waseem, M., Wi, S., and Kim, T.-W. (2015). "Evolution of a parsimonious rainfall–runoff model using soil moisture proxies." *Journal of Hydrology*, Elsevier, 530, 623–633.

Alcamo, J., Döll, P., Henrichs, T., Kaspar, F., Lehner, B., Rösch, T., and Siebert, S. (2003). "Development and testing of the WaterGAP 2 global model of water use and availability." *Hydrological Sciences Journal*, Taylor & Francis, 48(3), 317–337.

Allen, R. G., Pereira, L. S., Raes, D., and Smith, M. (1998). *Crop evapotranspiration: guidelines for computing crop water requirements. FAO Paper 56*. Food and Agriculture Organization of the United Nations, Rome.

Anderson, E. (2002). *Calibration of Conceptual Hydrologic Models for Use in River Forecasting*. National Oceanic and Atmospheric Administration, National Weather Service Hydrology Laboratory, Silver Spring, MD.

Anderson, E. (2006). *Snow accumulation and ablation model—SNOW-17*. National Oceanic and Atmospheric Administration, National Weather Service Hydrology Laboratory, Silver Spring, MD.

Arnell, N. W., and Gosling, S. N. (2013). "The impacts of climate change on river flow regimes at the global scale." *Journal of Hydrology*, Elsevier, 486, 351–364.

Arnold, J. G., Srinivasan, R., Muttiah, R. S., and Williams, J. R. (1998). "Large Area Hydrologic Modeling and Assessment Part I: Model Development." *Journal of the American Water Resources Association*, Blackwell Publishing Ltd, 34(1), 73–89.

Von Arx, G., Dobbertin, M., and Rebetez, M. (2012). "Spatio-temporal effects of forest canopy on understory microclimate in a long-term experiment in Switzerland." *Agricultural and Forest Meteorology*, 166–167, 144–155.

Baver, L. D. (1939). "Ewald Wollny—A Pioneer in Soil and Water Conservation Research 1." *Soil Science Society of America Journal*, Soil Science Society of America, 330–333.

Beck, H. E., van Dijk, A. I. J. M., de Roo, A., Miralles, D. G., McVicar, T. R., Schellekens, J., and Bruijnzeel, L. A. (2016). "Global-scale regionalization of hydrologic model parameters." *Water Resources Research*, Blackwell Publishing Ltd, 52(5), 3599–3622.

Bennett, T. (1998). "Development and application of a continuous soil moisture accounting algorithm for the Hydrologic Engineering Center Hydrologic Modeling System (HEC-HMS)." M.S. Thesis, Dept of Civil and Environmental Engineering, University of California, Davis.

Bergström, S. (1992). *The HBV model: Its structure and applications*. Swedish Meteorological and Hydrological Institute, Norrköping, Sweden.

Boryan, C., Yang, Z., Mueller, R., and Craig, M. (2011). "Monitoring US agriculture: the US Department of Agriculture, National Agricultural Statistics Service, Cropland Data Layer Program." *Geocarto International*, Taylor & Francis , 26(5), 341–358.

Byun, K., Chiu, C. M., and Hamlet, A. F. (2019). "Effects of 21st century climate change on seasonal flow regimes and hydrologic extremes over the Midwest and Great Lakes region of the US." *Science of the Total Environment*, Elsevier B.V., 650, 1261–1277.

Carlyle-Moses, D. E., and Gash, J. H. C. (2011). "Rainfall Interception Loss by Forest Canopies." *Forest Hydrology and Biogeochemistry*, D. Levia, D. Carlyle-Moses, and T. Tanaka, eds., Springer, Dordrecht, 407–423.

Carsel, R. F., Imhoff, J. C., Hummel, P. R., Cheplick, J. M., and Donigian, A. S. (1998). "PRZM-3: A model for predicting pesticide and nitrogen fate in the crop root and unsaturated soil zones; Users Manual for Release 3.0." *US EPA*.

Chu, X., Lin, Z., Tahmasebi Nasab, M., Zeng, L., Grimm, K., Bazrkar, M. H., Wang, N., Liu, X., Zhang, X., and Zheng, H. (2019). "Macro-scale grid-based and subbasin-based hydrologic modeling: joint simulation and cross-calibration." *Journal of Hydroinformatics*, 21(1), 77–91.

Chu, X., Yang, J., Chi, Y., and Zhang, J. (2013). "Dynamic puddle delineation and modeling of puddle-to-puddle filling-spilling-merging-splitting overland flow processes." *Water Resources Research*, 49(6), 3825–3829.

Daly, C., Halbleib, M., Smith, J. I., Gibson, W. P., Doggett, M. K., Taylor, G. H., Curtis, J., and Pasteris, P. P. (2008). "Physiographically sensitive mapping of climatological temperature and precipitation across the conterminous United States." *International Journal of Climatology*, John Wiley & Sons, Ltd, 28(15), 2031–2064.

Döll, P., Berkhoff, K., Bormann, H., Fohrer, N., Gerten, D., Hagemann, S., and Krol, M. (2008). "Advances and visions in large-scale hydrological modelling: findings from the 11th Workshop on Large-Scale Hydrological Modelling." *Adv. Geosci*, 18, 51–61.

Eagleson, P. S. (1986). "The emergence of global-scale hydrology." *Water Resources Research*, 22(9S), 6S-14S.

Environmental Systems Research Institute (ESRI). (2014). *ArcGIS Desktop. Environmental Systems Research Institute*, Redlands, CA, USA.

FAO Statistical Development Series-15. (2017). *World Programme of the Census of Agriculture 2020, Volume I: Programme, concepts and definitions*.

Fontaine, T. A., Cruickshank, T. S., Arnold, J. G., and Hotchkiss, R. H. (2002). "Development of a snowfall–snowmelt routine for mountainous terrain for the soil water assessment tool (SWAT)." *Journal of Hydrology*, Elsevier, 262(1–4), 209–223.

Fuka, D. R., Easton, Z. M., Brooks, E. S., Boll, J., Steenhuis, T. S., and Walter, M. T. (2012). "A Simple Process-Based Snowmelt Routine to Model Spatially Distributed Snow Depth and Snowmelt in the SWAT Model [1]." *JAWRA Journal of the American Water Resources Association*, Wiley/Blackwell (10.1111), 48(6), 1151–1161.

Gudmundsson, L., Tallaksen, L. M., Stahl, K., Clark, D. B., Dumont, E., Hagemann, S., Bertrand, N., Gerten, D., Heinke, J., Hanasaki, N., Voss, F., and Koirala, S. (2012). "Comparing Large-Scale Hydrological Model Simulations to Observed Runoff Percentiles in Europe." *Journal of Hydrometeorology*, 13(2), 604–620.

Gupta, H. V., Kling, H., Yilmaz, K. K., and Martinez, G. F. (2009). "Decomposition of the mean squared error and NSE performance criteria: Implications for improving hydrological modelling." *Journal of Hydrology*, 377(1–2), 80–91.

Hargreaves, G. H., and Samani, Z. A. (1985). "Reference crop evapotranspiration from temperature." *Appl. Eng. Agric*, 1(2), 96–99.

Hedstrom, N. R., and Pomeroy, J. W. (1998). "Measurements and modelling of snow interception in the boreal forest." *Hydrological Processes*, Wiley-Blackwell, 12(10–11), 1611–1625.

Von Hoyningen-Huene, J. (1981). *Die Interzeption des Niederschlags in landwirtschaftlichen Pflanzenbeständen*. Arbeitsbericht DeutscherVerband fur Wasserwirtschaft und Kulturbau, DVWK, Braunschwig,Germany.

Huang, M., Gallichand, J., Wang, Z., and Goulet, M. (2006). "A modification to the Soil Conservation Service curve number method for steep slopes in the Loess Plateau of China." *Hydrological Processes*, Wiley-Blackwell, 20(3), 579–589.

Intel. (2019). "Intel® Fortran Compiler Release Notes and New Features." <https://software.intel.com/en-us/articles/intel-fortran-compiler-release-notes> (Sep. 19, 2018).

Jame, Y.-W., and Norum, D. I. (1980). “Heat and mass transfer in a freezing unsaturated porous medium.” *Water Resources Research*, John Wiley & Sons, Ltd, 16(4), 811–819.

Jin, C. X., Sands, G. R., Kandel, H. J., Wiersma, J. H., and Hansen, B. J. (2008). “Influence of Subsurface Drainage on Soil Temperature in a Cold Climate.” *Journal of Irrigation and Drainage Engineering*, 134(1), 83–88.

Kauffeldt, A., Wetterhall, F., Pappenberger, F., Salamon, P., and Thielen, J. (2016). “Technical review of large-scale hydrological models for implementation in operational flood forecasting schemes on continental level.” *Environmental Modelling and Software*, Elsevier Ltd, 75, 68–76.

Kontorshchikov, A. S., and Eremina, K. A. (1963). “Interception of precipitation by spring wheat during the growing season.” *Soviet Hydrology*, 2, 400–409.

Kozak, J. A., Ahuja, L. R., Green, T. R., and Ma, L. (2007). “Modelling crop canopy and residue rainfall interception effects on soil hydrological components for semi-arid agriculture.” *Hydrological Processes*, John Wiley & Sons, Ltd., 21(2), 229–241.

Krysanova, V., and Hattermann, F. F. (2017). “Intercomparison of climate change impacts in 12 large river basins: overview of methods and summary of results.” *Climatic Change*, Springer Netherlands, 141(3), 363–379.

Leavesley, G. H. (1989). “Problems of snowmelt runoff modelling for a variety of physiographic and climatic conditions.” *Hydrological Sciences Journal*, 34(6), 617–634.

Lehner, B., Döll, P., Alcamo, J., Henrichs, T., and Kaspar, F. (2006). “Estimating the Impact of Global Change on Flood and Drought Risks in Europe: A Continental, Integrated Analysis.” *Climatic Change*, Kluwer Academic Publishers, 75(3), 273–299.

Liang, S., and Li, X. (2012). “Fractional Vegetation Cover.” *Advanced Remote Sensing*, Shunlin Liang and Xiaowen Li, eds., Elsevier, 415–438.

Liang, X., Lettenmaier, D. P., Wood, E. F., and Burges, S. J. (1994). “A simple hydrologically based model of land surface water and energy fluxes for general circulation models.” *Journal of Geophysical Research*, 99(D7), 14415.

Lin, Z., Anar, M. J., and Zheng, H. (2015). “Hydrologic and water-quality impacts of agricultural land use changes incurred from bioenergy policies.” *Journal of Hydrology*, 525, 429–440.

Lindström, G., Gardelin, M., and Persson, M. (1994). *Conceptual modelling of evapotranspiration for simulations of climate change effects*. Swedish Meteorological and Hydrological Institute. Norrköping, Sweden.

Lindström, G., Johansson, B., Persson, M., Gardelin, M., and Bergström, S. (1997). “Development and test of the distributed HBV-96 hydrological model.” *Journal of Hydrology*, Elsevier, 201(1–4), 272–288.

Lindström, G., Pers, C., Rosberg, J., Strömqvist, J., and Arheimer, B. (2010). “Development and testing of the HYPE (Hydrological Predictions for the Environment) water quality model for different spatial scales.” *Hydrology Research*, 41(3–4).

Liston, G. E., Elder, K., Liston, G. E., and Elder, K. (2006). “A Distributed Snow-Evolution Modeling System (SnowModel).” *Journal of Hydrometeorology*, 7(6), 1259–1276.

Lull, H. W. (1964). “Ecological and silvicultural aspects.” *Handbook of Applied Hydrology*, V. Te Chow, ed., McGraw-Hill, New York, NY.

Maidment, D. R. (1993). *Handbook of hydrology*. McGraw-Hill, New York.

Mengel, K., Kirkby, E. A., Kosegarten, H., and Appel, T. (2001). “Plant Growth and Crop Production.” *Principles of Plant Nutrition*, Springer Netherlands, Dordrecht, 243–335.

Michel, C., Andréassian, V., and Perrin, C. (2005). “Soil Conservation Service Curve Number method: How to mend a wrong soil moisture accounting procedure?” *Water Resources Research*, Wiley-Blackwell, 41(2).

Miralles, D. G., Gash, J. H., Holmes, T. R. H., de Jeu, R. A. M., and Dolman, A. J. (2010). "Global canopy interception from satellite observations." *Journal of Geophysical Research*, 115(D16), D16122.

Mishra, S. K., and Singh, V. P. (2003). *Soil Conservation Service Curve Number (SCS-CN) Methodology*. Water Science and Technology Library, Springer Netherlands, Dordrecht.

Mohamoud, Y. M., and Ewing, L. K. (1990). "Rainfall interception by corn and soybean residue." *Transactions of the ASAE*, American Society of Agricultural and Biological Engineers, 33(2), 0507–0511.

Molnau, M., and Bissell, V. (1983). "A continuous frozen ground index for flood forecasting." *Proceedings of the 51st Annual Western Snow Conference*, Vancouver, Washington.

Monteith, J. L. (1965). "Evaporation and the Environment in the State and Movement of Water in Living Organisms." *Proceedings of the Society for Experimental Biology, Symposium No. 19*, Cambridge University Press, Cambridge, 205–234.

Moriasi, D. N., Arnold, J. G., Van Liew, M. W., Bingner, R. L., Harmel, R. D., and Veith, T. L. (2007). "Model evaluation guidelines for systematic quantification of accuracy in watershed simulations." *Transactions of the ASABE*, American society of agricultural and biological engineers, 50(3), 885–900.

Moriasi, D. N., Zeckoski, R. W., Arnold, J. G., Baffaut, C., Malone, R. W., Daggupati, P., Guzman, J. A., Saraswat, D., Yuan, Y., Wilson, B. . N., Shirmohammadi, A., and Douglas-Mankin, K. R. (2015). "Hydrologic and Water Quality Models: Key Calibration and Validation Topics." *Transactions of the ASABE*, American Society of Agricultural and Biological Engineers, 58(6), 1609–1618.

Motovilov, Y. G. (2016). "Hydrological simulation of river basins at different spatial scales: 2. test results." *Water Resources*, 43(5), 743–753.

Motovilov, Y. G., Gottschalk, L., Engeland, K., and Belokurov, A. (1999). *ECOMAG: Regional model of hydrological cycle. Application to the NOPEX region*. Oslo, Norway.

Musselman, K. N., Clark, M. P., Liu, C., Ikeda, K., and Rasmussen, R. (2017). “Slower snowmelt in a warmer world.” *Nature Climate Change*, Nature Publishing Group, 7(3), 214–219.

Natural Resources Conservation Service. (2015). “Soil Data Viewer 6.2 User Guide.” <https://www.nrcs.usda.gov/Internet/FSE_DOCUMENTS/nrcs142p2_052432.pdf> (Oct. 11, 2019).

Neitsch, S., Arnold, J., Kiniry, J., and Williams, J. (2011). *Soil and Water Assessment Tool (SWAT) theoretical documentation version 2009*. Texas Water Resources Institute, College Station, Texas.

NRCS. (2018). “STATSGO2 Database.” *Natural Resources Conservation Service, United States Department of Agriculture. Web Soil Survey*, <http://websoilsurvey.nrcs.usda.gov/> (Apr. 27, 2018).

Oke, T. R. (1973). “City size and the urban heat island.” *Atmospheric Environment (1967)*, Elsevier, 7(8), 769–779.

Oubeidillah, A. A., Kao, S. C., Ashfaq, M., Naz, B. S., and Tootle, G. (2014). “A large-scale, high-resolution hydrological model parameter data set for climate change impact assessment for the conterminous US.” *Hydrology and Earth System Sciences*, 18(1), 67–84.

Oudin, L., Hervieu, F., Michel, C., Perrin, C., Andréassian, V., Anctil, F., and Loumagne, C. (2005). “Which potential evapotranspiration input for a lumped rainfall–runoff model?: Part 2—Towards a simple and efficient potential evapotranspiration model for rainfall–runoff modelling.” *Journal of Hydrology*, 303(1–4), 290–306.

Paiva, R. C. D., Collischonn, W., and Tucci, C. E. M. (2011). “Large scale hydrologic and hydrodynamic modeling using limited data and a GIS based approach.” *Journal of Hydrology*, 406(3), 170–181.

Pomeroy, J. W., Parviainen, J., Hedstrom, N., and Gray, D. M. (1998). “Coupled modelling of forest snow interception and sublimation.” *Hydrological Processes*, Wiley-Blackwell, 12(15), 2317–2337.

Priestley, C. H. B., and Taylor, R. J. (1972). “On the assessment of surface heat flux and evaporation using large-scale parameters.” *Monthly weather review*, Washington, 100(2), 81–92.

Python. (2010). “Python 2.7.0 Release.” <https://www.python.org/download/releases/2.7/> (Aug. 10, 2018).

Qi, J., Li, S., Jamieson, R., Hebb, D., Xing, Z., and Meng, F.-R. (2017). “Modifying SWAT with an energy balance module to simulate snowmelt for maritime regions.” *Environmental Modelling & Software*, Elsevier, 93, 146–160.

Rawls, W. J., and Brakensiek, D. L. (1983). “A procedure to predict Green and Ampt infiltration parameters.” *Proceedings of the American Society of Agricultural Engineers Conference on Advances in Infiltration*, 102–112.

Rawls, W. J., Brakensiek, D. L., and Saxtonn, K. E. (1982). “Estimation of soil water properties.” *Transactions of the ASAE*, American Society of Agricultural and Biological Engineers, 25(5), 1316–1320.

Red River Basin Board. (2000). *Inventory team report: Hydrology*. *Red River Basin Board, Moorhead MN*.

Rodríguez, E., Sánchez, I., Duque, N., Arboleda, P., Vega, C., Zamora, D., López, P., Kaune, A., Werner, M., García, C., and Burke, S. (2019). “Combined Use of Local and Global Hydro Meteorological Data with Hydrological Models for Water Resources Management in the Magdalena - Cauca Macro Basin – Colombia.” *Water Resources Management*, Springer Science and Business Media LLC.

Rogelis, M. C., Werner, M., Obregón, N., and Wright, N. (2016). “Hydrological model assessment for flood early warning in a tropical high mountain basin.” *Hydrology and Earth System Sciences Discussions*, Copernicus GmbH, 1–36.

Savabi, M. R., and Stott, D. E. (1994). “Plant Residue Impact on Rainfall Interception.” *Transactions of the ASAE*, American Society of Agricultural and Biological Engineers, 37(4), 1093–1098.

Schmidt, R. A., and Gluns, D. R. (1991). “Snowfall interception on branches of three conifer species.” *Canadian Journal of Forest Research*, NRC Research Press Ottawa, Canada, 21(8), 1262–1269.

Sellers, P. J., Randall, D. A., Collatz, G. J., Berry, J. A., Field, C. B., Dazlich, D. A., Zhang, C., Collelo, G. D., Bounoua, L., Sellers, P. J., Randall, D. A., Collatz, G. J., Berry, J. A., Field, C. B., Dazlich, D. A., Zhang, C., Collelo, G. D., and Bounoua, L. (1996). “A Revised Land Surface Parameterization (SiB2) for Atmospheric GCMS. Part I: Model Formulation.” *Journal of Climate*, 9(4), 676–705.

Sharpley, A. N., and Williams, J. R. (1990). *EPIC—Erosion/productivity impact calculator: 1. model documentation*. US Department of Agriculture Technical Bulletin No. 1768. US Government Printing Office, Washington, DC.

Shoop, S. A., and Bigl, S. R. (1997). “Moisture migration during freeze and thaw of unsaturated soils: modeling and large scale experiments.” *Cold Regions Science and Technology*, Elsevier, 25(1), 33–45.

Sood, A., and Smakhtin, V. (2015). “Global hydrological models: a review.” *Hydrological Sciences Journal*, Taylor & Francis, 60(4), 549–565.

Stewart, I. T., Cayan, D. R., and Dettinger, M. D. (2004). “Changes in Snowmelt Runoff Timing in Western North America under a `Business as Usual’ Climate Change Scenario.” *Climatic Change*, Kluwer Academic Publishers, 62(1–3), 217–232.

Syvitski, J. P. M., Vörösmarty, C. J., Kettner, A. J., and Green, P. (2005). “Impact of Humans on the Flux of Terrestrial Sediment to the Global Coastal Ocean.” *Science*, 308(5720), 376–380.

Tahmasebi Nasab, M., and Chu, X. (2018). “Topo-Statistical Analyses of Ponding Area versus Ponding Storage of Depression-Dominated Regions for Macro-Scale Hydrologic Modeling.” *World Environmental and Water Resources Congress 2018*, American Society of Civil Engineers, Reston, VA, 415–424.

Tahmasebi Nasab, M., and Chu, X. (2019a). “Do Sub-daily Temperature Fluctuations around the Freezing Temperature Alter Macro-scale Snowmelt Simulations?” *Journal of Hydrology*, Under Review.

Tahmasebi Nasab, M., and Chu, X. (2019b). “Impacts of High-resolution Gridded Temperature Datasets on Macro-scale Snowmelt Simulations in Missouri River Basin.” *Hydrological Sciences Journal*, Under Review.

Tahmasebi Nasab, M., Grimm, K., Bazrkar, M., Zeng, L., Shabani, A., Zhang, X., and Chu, X. (2018). “SWAT Modeling of Non-Point Source Pollution in Depression-Dominated Basins under Varying Hydroclimatic Conditions.” *International Journal of Environmental Research and Public Health 2018, Vol. 15, Page 2492*, 15(11), 2492.

Tahmasebi Nasab, M., Grimm, K., Wang, N., and Chu, X. (2017a). “Scale Analysis for Depression-Dominated Areas: How Does Threshold Resolution Represent a Surface?” *World Environmental and Water Resources Congress 2017*, American Society of Civil Engineers, Reston, VA, 164–174.

Tahmasebi Nasab, M., Jia, X., and Chu, X. (2016). “Modeling of Subsurface Drainage under Varying Microtopographic, Soil and Rainfall Conditions.” *10th International Drainage Symposium*, J. Strock, ed., American Society of Agricultural and Biological Engineers, Minneapolis, MN, 133–138.

Tahmasebi Nasab, M., Singh, V., and Chu, X. (2017b). “SWAT Modeling for Depression-Dominated Areas: How Do Depressions Manipulate Hydrologic Modeling?” *Water*, Multidisciplinary Digital Publishing Institute, 9(1), 58.

Tahmasebi Nasab, M., Zhang, J., and Chu, X. (2017c). “A New Depression -Dominated Delineation (D-cubed) Method for Improved Watershed Modeling.” *Hydrological Processes*, 31(19), 3364–3378.

Terink, W., Lutz, A. F., Simons, G. W. H., Immerzeel, W. W., and Droogers, P. (2015). “SPHY v2.0: Spatial Processes in HYdrology.” *Geoscientific Model Development*, 8(7), 2009–2034.

USDA. (1986). *Urban hydrology for small watersheds*. Washington, DC: United States Department of Agriculture, Technical Release 55 (TR-55).

USGS. (2019a). “Red River Basin Flooding.” *United States Geological Survey*, <https://www.usgs.gov/centers/dakota-water/science/red-river-basin-flooding?qt-science_center_objects=0#1997> (Mar. 20, 2019).

USGS. (2019b). “USGS NED 1 arc-second 1 x 1 degree ArcGrid DEM.” *U.S. Geological Survey*, <https://viewer.nationalmap.gov/basic/> (Feb. 2, 2018).

USGS. (2019c). “USGS Water Data for the Nation.” <https://waterdata.usgs.gov/nwis> (Apr. 12, 2018).

Valente, F., David, J. S., and Gash, J. H. C. (1997). “Modelling interception loss for two sparse eucalypt and pine forests in central Portugal using reformulated Rutter and Gash analytical models.” *Journal of Hydrology*, Elsevier, 190(1–2), 141–162.

Valiantzas, J. D. (2013). “Simplified forms for the standardized FAO-56 Penman–Monteith reference evapotranspiration using limited weather data.” *Journal of Hydrology*, 505, 13–23.

Venetis, C. (1969). “A study on the recession of unconfined acquifers.” *International Association of Scientific Hydrology. Bulletin*, Taylor & Francis Group, 14(4), 119–125.

Verma, S., Verma, R. K., Mishra, S. K., Singh, A., and Jayaraj, G. K. (2017). “A revisit of NRCS-CN inspired models coupled with RS and GIS for runoff estimation.” *Hydrological Sciences Journal*, Taylor & Francis, 62(12), 1891–1930.

Vörösmarty, C. J., Moore, B., Grace, A. L., Gildea, M. P., Melillo, J. M., Peterson, B. J., Rastetter, E. B., and Steudler, P. A. (1989). "Continental scale models of water balance and fluvial transport: An application to South America." *Global Biogeochemical Cycles*, 3(3), 241–265.

Wood, E. F., Lettenmaier, D. P., Liang, X., Lohmann, D., Boone, A., Chang, S., Chen, F., Dai, Y., Dickinson, R. E., Duan, Q., Ek, M., Gusev, Y. M., Habets, F., Irannejad, P., Koster, R., Mitchel, K. E., Nasonova, O. N., Noilhan, J., Schaake, J., Schlosser, A., Shao, Y., Shmakin, A. B., Verseghy, D., Warrach, K., Wetzel, P., Xue, Y., Yang, Z. L., and Zeng, Q. C. (1998). "The project for intercomparison of land-surface parameterization schemes (PILPS) phase 2(c) Red-Arkansas River basin experiment: 1. Experiment description and summary intercomparisons." *Global and Planetary Change*, 19(1–4), 115–135.

Žaknić-Ćatović, A., Howard, K. W. F., and Ćatović, Z. (2018). "Modification of the degree-day formula for diurnal meltwater generation and refreezing." *Theoretical and Applied Climatology*, 131(3–4), 1157–1171.

Zhao, R., Zuang, Y., Fang, L., Liu, X., and Zhang, Q. (1980). "The Xinanjiang model." *Hydrological Forecasting Proceedings Oxford Symposium*, IAHS-AISH Publ 129, 351–356.

3. IMPACTS OF SUB-DAILY TEMPERATURE FLUCTUATIONS AROUND THE FREEZING TEMPERATURE ON MACRO-SCALE SNOWMELT SIMULATIONS[1]

3.1. Abstract

Climate-driven temperature variations manipulate the snowmelt process and affect various aspects of aquatic and terrestrial life. The objective of this study is to evaluate the impacts of sub-daily temperature fluctuations around the freezing temperature on the quantity and spatial distribution of macro-scale snowmelt simulations (i.e., over macro-scale basins and monthly or annual temporal scales). A macro-scale snow accumulation and ablation model was developed to account for sub-daily temperature fluctuations. Unlike other existing macro-scale models that rely upon a single daily average temperature, the new model incorporates minimum and maximum temperatures and their occurrence timing within the day in a hybrid temperature index method (HTIM). The model was applied to the Missouri River Basin to simulate grid-based snowmelt for water years 2011 and 2012 and compared with the monthly snowmelt data from the SNOw Data Assimilation System (SNODAS), which is a physically-based energy and mass balance snow model. Also, the HTIM was compared with a standard TIM, in which only a daily average temperature was used for snowmelt simulations. The HTIM provided comparable performance to the SNODAS snowmelt data ($R^2 = 0.9$). The modeling results suggested that daily macro-scale snowmelt simulations were notably susceptible to sub-daily temperature fluctuations, and the HTIM can improve the physically-based representation of temperature variations in the snowmelt process. However, monthly and annual snowmelt results indicated less sensitivity to sub-daily temperature fluctuations around the freezing temperature. The difference between the annual simulations by the HTIM and TIM was less than 1%. Results from

[1] The material in this chapter was co-authored by Mohsen Tahmasebi Nasab and Dr. Xuefeng Chu. Mohsen Tahmasebi Nasab had primary responsibility for developing the new analysis procedure and modeling of the system. Mohsen Tahmasebi Nasab was the primary developer of the conclusions that are advanced here. Mohsen Tahmasebi Nasab also drafted and revised all versions of this chapter. Dr. Xuefeng Chu served as proofreader and checked analysis conducted by Mohsen Tahmasebi Nasab.

this study highlight the influence of sub-daily temperature fluctuations on macro-scale snowmelt simulations. The macro-scale snow model developed in this study can also be applied to other basins with similar hydroclimatic characteristics.

3.2. Introduction

The Fourth National Climate Assessment report (NCA4) confirmed that the climate-driven changes in the United States are already tangible in different aspects of aquatic and terrestrial life (USGCRP 2018). In the Northern Great Plains, for example, the fast springtime warming has led to earlier snowmelt events (USGCRP 2018). Among the numerous impacts of snowmelt on aquatic life and biodiversity, snowmelt can significantly disturb communities by contributing to spring floods. For example, parts of the Missouri River Basin (MRB) and Red River of the North Basin (RRB) in Dakotas and Minnesota underwent a record-breaking snowfall during water year 2009 followed by a historical flood in March and April of 2009, in which 48 record stages were logged at the U.S. Geological Survey streamflow gauging stations in both basins (Macek-Rowland and Gross 2011). Fortunately, no flooding-related death was reported. However, the costs of flooding-related damages and flood-fighting efforts solely in the RRB were estimated at 55 million U.S. dollars (NOAA Water Resource Services, 2009).

The snow accumulation and ablation processes significantly affect the hydrologic response by storing and releasing water throughout the year (Jansson et al. 2003). In the cold climate basins in the western United States and Canada, for instance, snowmelt is a significant contributor to streamflow, feeding 50% to 80% of the total streamflow (Stewart et al. 2004). Throughout the past decades, different models have been developed to simulate snow accumulation and ablation processes. These models have been honed over time by the addition of cold-climate processes such as refreezing, sublimation, and snow-on-rain. Traditionally, snowmelt models are categorized based on the use of (1) energy balance methods (EBMs) or (2) temperature index methods (TIMs) (Leavesley 1989). EBMs solve the energy balance equation to estimate the available energy for snowmelt generation. An EBM in its original form requires a

variety of meteorological data such as solar radiation, temperature, vapor pressure, and wind speed, which might or might not be available depending on the locations of study areas. Due to the data-intensive nature of EBMs, a variety of modified/simplified methods have been developed, in which different energy balance terms are estimated based on certain simplifying assumptions and empirical relationships (e.g., Fuka et al. 2012). In contrast, TIMs simulate the amount of snowmelt on a given time step solely based on daily average temperature and a melting factor. In TIMs, different elements of the snowmelt process (i.e., components of the energy balance equation), except for temperature, are lumped together into the melting factor (Hock 2005; Leavesley 1989). Hock (2005) provided a comprehensive review of EBMs and TIMs and suggested that due to the availability of air temperature data, TIMs will remain the most widely used method to estimate snowmelt for different purposes. Simplicity and practicality of the TIMs are the main reasons for their frequent use in several macro-scale hydrologic models such as Spatial Processes in Hydrology (SPHY) (Terink et al. 2015), Hydrologiska Byråns Vattenbalansavdelning (HBV) (Bergström 1992), Hydrological Predictions for the Environment (HYPE) (Lindström et al. 2010), and Water Global Assessment and Prognosis (WaterGAP) (Alcamo et al. 2003).

TIMs have been subject to various improvements to ensure reliable snowmelt simulations for regions with different hydroclimatic characteristics. The majority of these improvements have been achieved by employing two approaches: (1) modifying the melting factor to account for spatial and temporal variations and (2) adding the lumped effects of other energy balance terms to the original TIMs. Several studies employed the first approach to enhance snowmelt simulations. Hock (2003) reviewed the TIM snowmelt modeling and different attempts to account for the spatiotemporal variations of the melting factor and concluded that the majority of modifications to the TIM were mainly targeted to the seasonal variations of the melting factor. For example, Rango and Martinec (1995) developed the seasonally variable melting factor, which led to the development of snowmelt routines

accounting for the seasonal variability of the melting factor based on maximum and minimum melting factors (Fontaine et al. 2002). Singh et al. (2005) adjusted the melting factor to include the impacts of both near-surface soil temperature and air temperature on the snowmelt process. Many other studies employed the second approach. For example, Zuzel and Cox (1975) highlighted the importance of other energy balance terms. They evaluated the relative significance of different meteorological variables in the snowmelt process and found that addition of vapor pressure, net radiation, and wind in the TIMs improved snowmelt simulations by 13% in comparison with the single temperature index method. Also, Brubaker et al. (1996) and Hock (1999) included a radiation term in the original TIM to improve snowmelt simulations. Specifically, Hock (1999) developed a grid-based spatially distributed model to capture the diurnal snowmelt cycles by including potential clear-sky direct solar radiation, which has the advantage of requiring the same input data as the original TIM (i.e., only temperature data) and a digital elevation model of the study area.

Macro-scale hydrologic models are customarily associated with regional, continental, or even global scales (Chu et al. 2019) and are used to investigate the impacts of climate-driven changes on hydrologic processes. Reasonably, macro-scale hydrologic models cannot take advantage of the methods that are specific to point- or micro-scale modeling. Hence, before selecting a simulation method, different aspects of macro-scale modeling such as input data requirements and flexibility in resolution need to be considered. The fact that TIMs provide comparable results to EBMs at a macro scale (WMO 1986) allows macro-scale hydrologic models to incorporate different versions of TIMs without significant loss of information (Zuzel and Cox 1975). The temporal resolution adopted in TIMs is of equal importance in the snowmelt simulation. Several studies have indicated that the performance of TIMs significantly decreases when finer temporal resolutions (smaller than a couple of days) are used (Hock 1999, 2005). For example, Rango and Martinec (1995) suggested that TIMs provide reliable simulations of

snowmelt when they are used for weekly to seasonal time steps; however, they also can be used for daily simulations when linked to hydrologic models (Rango and Martinec 1995).

One of the critical simplifying assumptions behind TIMs that restricts their use for daily simulations is that each time step is represented by a single temperature (i.e., the daily average temperature). This assumption is reasonable when sub-daily temperatures are all either above or below the freezing temperature. However, when sub-daily temperatures fluctuate above or below the freezing temperature, the single-temperature TIM cannot provide realistic snowmelt simulations (Hock 1999; Žaknić-Ćatović et al. 2018). Different attempts have been made to capture the sub-daily snowmelt fluctuations at point-scale or subbasin-scale (e.g., Dunn and Colohan, 1999; Tobin et al., 2013; Žaknić-Ćatović et al., 2018). Tobin et al. (2013) developed a modified TIM that utilized the difference between the daily maximum and minimum temperatures (i.e., temperature range) to account for the diurnal snowmelt cycles at a subbasin scale. Specifically, they proposed a new method to compute a time-varying melting factor using a quasi-sinusoidal function, assuming that the daily cycle of incoming radiation can be represented by the temperature amplitude (Tobin et al. 2013). The simulations from the original and modified TIMs were evaluated for both point and subbasin scales, and the results indicated that the modified TIM significantly improved the sub-daily variability of snowmelt (Tobin et al. 2013). Moreover, to account for the impacts of temperature fluctuations around the freezing temperature, Žaknić-Ćatović et al. (2018) proposed a modified TIM that shifted the reliance of snowmelt simulations away from one temperature towards maximum and minimum temperatures. The performance of the modified TIM was evaluated using the observed data from two weather stations in Alberta and Toronto, Canada (Žaknić-Ćatović et al. 2018). The evaluation results confirmed that considering temperature variations around the freezing temperature improved the physical representation of snowmelt at a point scale (i.e., at the weather stations) (Žaknić-Ćatović et al. 2018). Although different studies indicated better snowmelt results at a point scale and/or small basin scale when sub-daily temperatures were

incorporated into the TIM, few studies have addressed snowmelt simulation issues in macro-scale basins. For example, Tobin et al. (2013) simulated snowmelt for the Cotton Creek Experimental Watershed (CCEW) in British Columbia, Canada, which had an area of only 17 km^2. Therefore, the impacts of sub-daily temperature variations around the freezing temperature on snowmelt simulations in macro-scale basins (> a few thousand km^2) are still unknown.

Given the importance of macro-scale hydrologic modeling and the significance of snowmelt in hydrologic modeling, the objective of this study is to evaluate the impacts of sub-daily temperature fluctuations around the freezing temperature on macro-scale snowmelt simulations. Particularly, this study uses a macro-scale approach that incorporates sub-daily temperature variations in a standard TIM to investigate the influences of sub-daily temperature variations on the snowmelt simulations over large spatiotemporal scales (i.e., monthly or annual scales in macro-scale basins). To accomplish the objective of this study, a new macro-scale snow accumulation and ablation model (MSM) is developed, in which sub-daily temperature variations around the freezing temperature are included by incorporating maximum and minimum temperatures and their occurrence timing in a hybrid TIM (HTIM). HTIM has the advantage of retaining the simplicity of the standard TIM by using widely available temperature datasets. In addition, the developed MSM utilizes only eight parameters that are defined based on the specific characteristics of different study areas, and it can be easily incorporated into macro-scale hydrologic models for simulations in the areas with limited data. The model is applied to the MRB, and the simulation results are compared with the snowmelt data from the National Oceanic and Atmospheric Administration (NOAA) National Operational Hydrologic Remote Sensing Center (NOHRSC) SNOw Data Assimilation System (SNODAS). Moreover, the modeling results are also compared with those simulated by a standard TIM. This study identifies the impact of sub-daily temperature fluctuations above and below freezing temperatures and their occurrence timing on macro-scale snowmelt simulations.

3.3. Study Area

Stretching from western Montana to St. Louis, MO, the MRB (Figure 3.1a) has a drainage area of 1.37 M km^2, covering parts of 10 U.S. States (~98% of the MRB's drainage area) and 2 Canadian provinces. The MRB is an important global agricultural region and produces nearly half (46%) of the U.S wheat (Mehta et al. 2013). According to the Cropland Data Layer (CDL) classifications (Boryan et al. 2011), grassland/pasture and cropland are the dominant land-use types (Figure 3.1b), and corn and soybeans are the two leading crops in the MRB. Also, different types of forests (i.e., evergreen and deciduous) are mostly scattered on the western side of the basin (Figure 3.1b), accounting for ~10% of the basin's land. The MRB encompasses a wide variety of hydroclimatic, geologic, and topographic conditions. For example, the basin has an elevation drop of more than 4 km from the western side to the eastern side of the basin (Figure 3.1c).

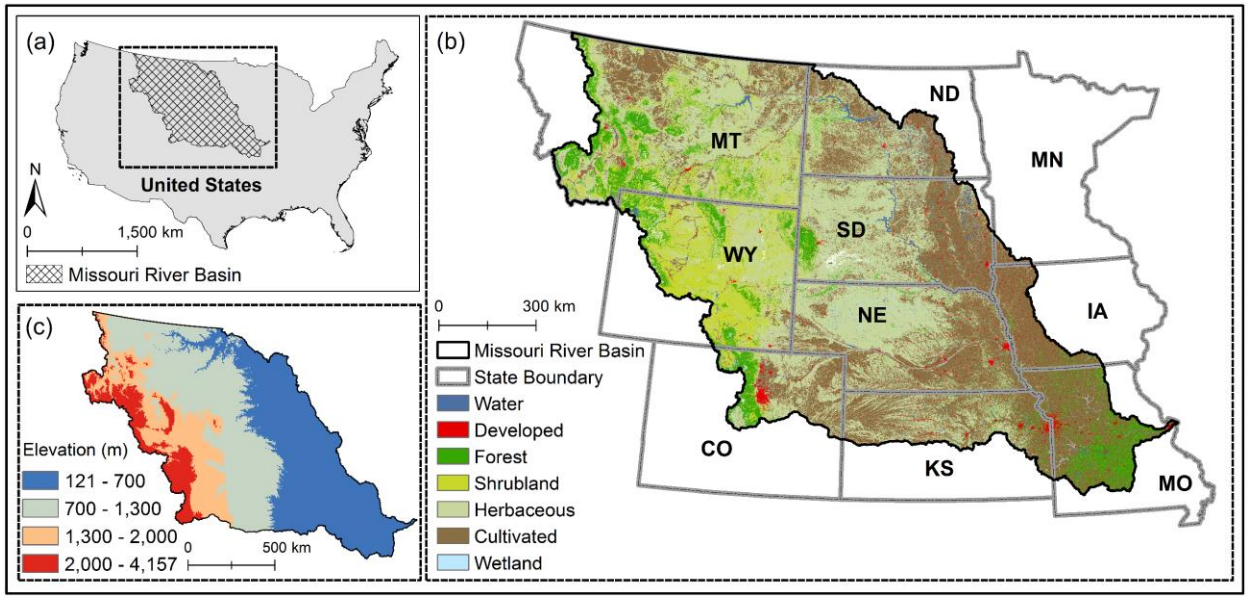

Figure 3.1. Missouri River Basin: (a) domain, (b) land use distribution, and (c) elevation variations.

Several studies have highlighted the current and future hydroclimatic variations of the MRB caused by the climate-driven changes (Livneh et al. 2016; U.S. Bureau of Reclamation 2016; Wise et al. 2018). The 2016 SECURE Water Act Report projected a 2.78°C to 3.34°C

increase in MRB's temperature throughout the 21st century (U.S. Bureau of Reclamation 2016). By prompting earlier snowmelt and reducing streamflow during summer months, this warming trend impacts many aspects of the basin such as biodiversity, agriculture, and navigation (Wise et al. 2018). Since temperature is projected to continue its increasing trend throughout the 21st century (U.S. Bureau of Reclamation 2016), understanding the snowmelt process and improving its representation in hydrologic models can lead to more realistic modeling results for the MRB.

The 2011 record-breaking flood in the MRB, which was immediately followed by the 2012 drought, is a typical example of expected hydroclimatic variations in the basin. The extents of wetness and dryness of these representative years (i.e., 2011 and 2012) are more evident when they are compared to the long-term average precipitation. The average 30-year (1981-2010) precipitation in the basin is 538 mm. In contrast, the annual precipitation in 2011 was 623 mm, which is approximately 15% higher than the 30-year average. Particularly, the cold-season precipitation in the upper MRB increased by 36.7% relative to the basin's normal climatic condition (Badger et al. 2018), which led to a historic flood across the basin. On the other hand, the annual precipitation in 2012 was only 403 mm, which is about 25% lower than the average. Therefore, immediately after the 2011 flood throughout the Plains and Midwest, the 2012 drought occurred and highly stressed the food-producing regions of the MRB (Fuchs et al. 2012).

3.4. Methodology

3.4.1. Design of the Study and Data Acquisition

The MSM is used to simulate snow accumulation and ablation processes in the MRB for consecutive WYs 2011 and 2012 (731 days from October 1st, 2010, to September 30th, 2012). As previously mentioned, WYs 2011 and 2012 are characterized by their hydroclimatic conditions, where WY 2011 represents a wet year and WY 2012 represents a dry year. The study area is discretized into 54,144 grids of 5×5 km^2, and snow accumulation and ablation processes are simulated separately for each cell. Since the spatially distributed macro-scale measured

snowmelt data are not available, the simulated snowmelt results from the HTIM are compared with the snowmelt data from the NOAA's National Operational Hydrologic Remote Sensing Center (NOHRSC) SNOw Data Assimilation System (SNODAS) (hereafter SNODAS data). SNODAS is a modeling system that provides estimates of snow-related variables for hydrologic modeling and analysis. SNODAS employs physically-based, spatially-distributed energy- and mass-balance methods to assimilate satellite-derived, airborne and ground-based observations of snow-covered areas and snow water equivalent (Barrett 2003). The simulation results from the HTIM are further compared with those from the TIM to underline the impacts of sub-daily temperature fluctuations around the freezing temperature on the macro-scale snowmelt modeling. The spatiotemporal results from HTIM and TIM are compared against the SNODAS data using different graphical and statistical methods to provide a holistic picture of snowmelt variations over MRB. For example, the coefficient of determination (R^2) and percent bias (PBIAS) are two statistics that are used to determine the goodness of fit and the average tendency of the simulations to overestimate (PBIAS>0) or underestimate (PBIAS<0) snowmelt. The MSM uses eight pre-defined model parameters to simulate different snow accumulation and ablation processes. These modeling parameters and their values are listed in Table 3.1.

Table 3.1. Parameters and their values in the macro-scale snow model (MSM)

Parameter	Unit	Description	Value	Source
C_{SN}	-	Snowfall correction factor	0.96	Anderson (2002)
TT_{MAX}	^oC	Upper bound of TTR	5	Calibrated
TT_{MIN}	^oC	Lower bound of TTR	1	Calibrated
C_{CU}	-	Forest canopy unloading coefficient	0.7	Pomeroy et al. (1998)
C_{WR}	-	Water retention storage coefficient	0.1	Bergström (1992)
C_{MX}	mm $^oC^{-1}$ day^{-1}	Maximum melting factor	Varies	See Table 3
C_{MN}	mm $^oC^{-1}$ day^{-1}	Minimum melting factor	Varies	See Table 3
C_F	mm $^oC^{-1}$ day^{-1}	Freezing factor	0.05	Terink et al. (2015)

Table 3.2 lists the sources of data used in the MSM. The SNODAS snowmelt data provide the estimates of snowmelt for hydrologic modeling and analysis (NOHRSC 2004). The SNODAS digital images were first clipped to the boundaries of the MRB and then resampled from the original 1-km resolution to 5-km resolution digital images to facilitate the comparison between the simulated snowmelt and the SNODAS snowmelt data. The land use and land cover dataset was downloaded from the CDL dataset (Boryan et al. 2011) and was clipped to the boundaries of the study area.

Table 3.2. Input data and their sources utilized in the macro-scale snow model (MSM) (NOHRSC-SNODAS: NOAA's National Operational Hydrologic Remote Sensing Center SNOw Data Assimilation System, CDL: Cropland Data Layer, PRISM: Parameter-elevation Regressions on Independent Slopes Model, TopoWx: Topography Weather, and NCEI-LCD: National Climatic Data Center Local Climatological Data)

Dataset	Source	Reference	Spatial Resolution	Temporal Resolution
Snowmelt	SNODAS	NOHRSC (2004)	1 km	Daily
Land Use and Land Cover	CDL	Boryan et al. (2011)	30 m	Yearly
Precipitation	PRISM	PRISM Climate Group (2004)	4 km	Daily
Min. and max. temp.	TopoWx	Oyler et al. (2015a)	800 m	Daily
Hourly temperatures	NCEI-LCD	NCEI (2018)	-	Hourly

The precipitation data for the study area were obtained from the Parameter-elevation Regressions on Independent Slopes Model (PRISM Climate Group 2004) that generates grid-based estimates of annual, monthly, and daily climatic data such as precipitation by incorporating point-scale weather-station observations, the digital elevation model (DEM) of the basin, and other spatial datasets (Daly et al. 1994). Since there have been concerns about the potential biases in the PRISM temperature products (Oyler et al. 2015b; Wise et al. 2018), the grid-based maximum and minimum temperatures (T_{MIN} and T_{MAX}) data were retrieved from the Topography Weather (TopoWx) dataset (Oyler et al. 2015a). In addition to incorporating the weather-station observations and topographic variables, TopoWx uses atmospheric reanalysis data, and the Moderate Resolution Imaging Spectroradiometer (MODIS) land skin temperature

to provide 800-m resolution daily T_{MIN} and T_{MAX} data (Oyler et al. 2015a). Both the PRISM precipitation data and the TopoWx temperatures were resampled to 5-km resolution grids to be incorporated in the MSM.

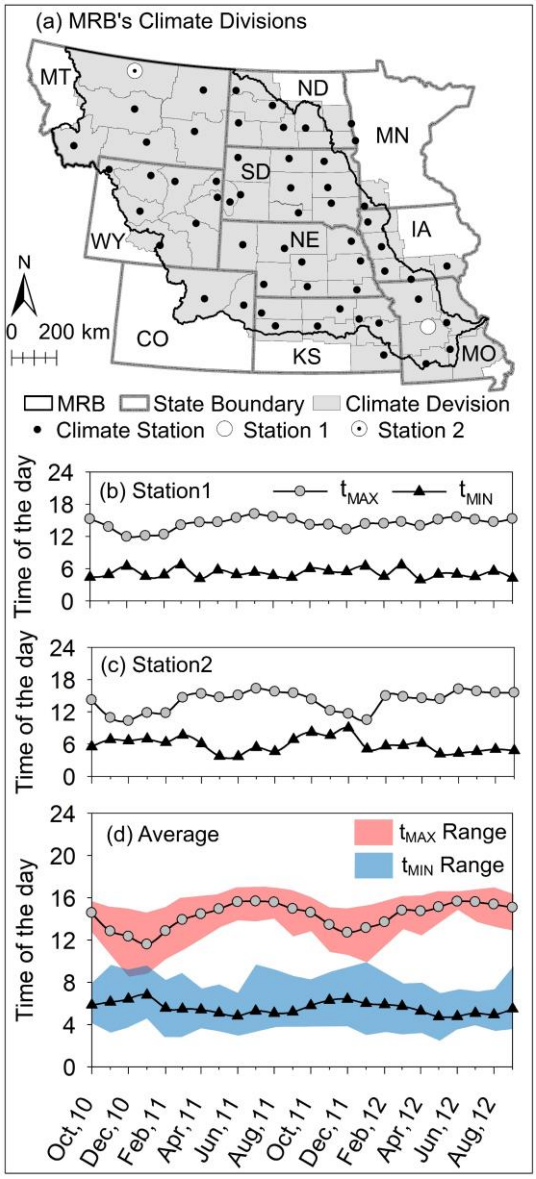

Figure 3.2. (a) Climate divisions of the Missouri River Basin (MRB); time of occurrence of minimum and maximum temperatures at (b) Stations 1, (c) station 2; and (d) average time of occurrence of minimum and maximum temperatures for all stations in MRB.

To find the time of occurrence of T_{MIN} and T_{MAX} (i.e., t_{MIN} and t_{MAX}), the MRB was divided into 58 NOAA climate divisions (Figure 3.2a). Within each climate division, a weather station was selected, and hourly temperature variations were obtained from the National Climatic Data

Center (NCDC) Local Climatological Data (LCD) for all 58 selected stations (NCDC 2018). Based on the hourly temperature variations, t_{MIN} and t_{MAX} were extracted for each day and used to calculate the average monthly t_{MIN} and t_{MAX} from October 2010 to September 2012. All grids within each climate division share the same t_{MIN} and t_{MAX}, assuming similar monthly variations of t_{MIN} and t_{MAX}. The analysis of hourly temperature variations showed that t_{MIN} and t_{MAX} followed an expected general trend, indicating that T_{MIN} occurred around sunrise and T_{MAX} took place right after midday. Figure 3.2b and Figure 3.2c show the seasonal variations of t_{MIN} and t_{MAX} for two selected stations in southern and northern MRB (Station 1 and Station 2, respectively). Station 1 tends to show less variability in t_{MIN} and t_{MAX} (Figure 3.2b), whereas Station 2 shows significant variability between warm and cold months (Figure 3.2c). This general trend was observed for all other southern and northern stations. Figure 3.2d depicts the average t_{MIN} and t_{MAX} and their ranges for all 58 stations, in which the variability between cold and warm months is evident.

3.4.2. Standard vs. Hybrid Temperature Index Method

A standard TIM is commonly expressed as:

$$M = \begin{cases} C_M T_{AVE} \Delta t & T_{AVE} > 0 \\ 0 & T_{AVE} \leq 0 \end{cases} \quad (3.1)$$

where M is the snowmelt (mm), C_M is the melting factor (mm $^oC^{-1}$ day^{-1}), and T_{AVE} is the average temperature (^oC) during time step Δt (day).

Despite its popularity, the standard TIM has the potential to underestimate or overestimate daily snowmelt noticeably. Figure 3.3a depicts hourly temperature variations for two hypothetical consecutive days, which reveal how the TIM can miscalculate snowmelt. The daily average temperatures for Day 1 and Day 2 in Figure 3.3a are -0.8 ^oC and 1.6 ^oC, respectively. According to the TIM, Day 1 does not generate any snowmelt since its average temperature is less than the assumed freezing temperature (i.e., 0^oC). However, nearly half of Day 1 has greater than 0^oC temperatures (Figure 3.3a). In other words, the TIM does not yield

any snowmelt, even though half of Day 1 can potentially generate snowmelt. The case illustrated in Figure 3.3a occurs only when sub-daily temperatures fluctuate around the freezing temperature, and it is not the case when temperatures are all above/below the freezing temperature (Day 2 in Figure 3.3a). To alleviate this issue, a hybrid TIM is used to take advantage of the standard TIM and meanwhile consider daily maximum and minimum temperatures at known occurrence times (Žaknić-Ćatović et al. 2018). This hybrid approach provides sub-daily simulations of snowmelt and refreezing and also is simple enough to be incorporated into macro-scale hydrologic models.

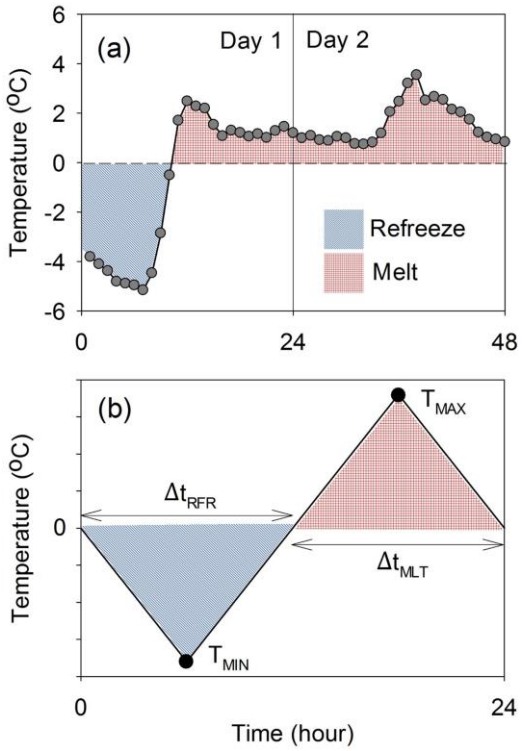

Figure 3.3. Hourly temperature variations above and below 0 °C for (a) two sample days and (b) a conceptual representation of temperature variations around the freezing temperature based on the daily minimum and maximum temperatures.

It is worth mentioning that although different studies have suggested a strong correlation between snowmelt and air temperature (e.g., Braithwaite and Olesen, 1989), snowmelt is also a function of other terms in the energy balance equation (Leavesley 1989; Ohmura 2001). For example, snowpack temperature can play an essential role in the generation

of snowmelt. However, different TIMs do not explicitly account for snowpack temperature. The amount of snowmelt depends on the contributions of different factors or energy balance terms that vary with geographic and hydroclimatic conditions (Hock 2005). Thus, the related studies suggest that the TIM results should be interpreted for "average conditions" (Hock 2005).

The HTIM incorporates the daily minimum and maximum temperatures (i.e., T_{MIN} and T_{MAX}, respectively) for simulating snowmelt when T_{MIN} is lower than 0°C and T_{MAX} is higher than 0°C (Figure 3.3b). Calculating snowmelt and refreezing using the HTIM requires sub-daily temperature variations. Either measured or synthetic sub-daily temperatures can be utilized to obtain these variations. For example, Žaknić-Ćatović et al. (2018) tested two approaches to estimate hourly temperature variations based on (1) a linear relationship and (2) a double cosine trigonometric relationship between T_{MIN} and T_{MAX}. In this study, a simple geometric method was used to approximate the sub-daily defacto melting and freezing periods based on the area of two triangles (Figure 3.3b). The HTIM establishes a linear relationship between T_{MIN} and T_{MAX} at their known times of occurrence to simulate the sub-daily snowmelt and refreezing processes (Figure 3.3b). In this method, snowmelt and refreezing are calculated for a fraction of the day with temperatures higher and lower than 0°C, respectively. For the days, in which T_{MIN} is lower than 0°C and T_{MAX} is higher than 0°C, snowmelt and refreezing are approximated using the two triangles, representing melt and refreeze processes (Figure 3.3b). The linear relationship between T_{MIN} and $T_{MAX,}$ for each day, is written as:

$$T = at + b, \tag{3.2}$$

where T is the temperature (°C) at time t (hour), and a and b are the slope and the intercept of the line, respectively. These two coefficients (i.e., a and b) are calculated for each day based on the following general forms:

$$a = \frac{T_{MAX} - T_{MIN}}{t_{MAX} - t_{MIN}} \tag{3.3}$$

$$b = \frac{T_{MIN} t_{MAX} - T_{MAX} t_{MIN}}{t_{MAX} - t_{MIN}} \tag{3.4}$$

in which t_{MAX} and t_{MIN} are the occurrence times of T_{MAX} and T_{MIN}, respectively, that determine the location of the triangles in Figure 3.3b within each day. If T_{MAX} occurs earlier than T_{MIN} in a day, the order of the triangles in Figure 3.3b switches. In this case, the same set of equations are applicable, but the slope of the line in Equation 2 becomes negative. Although every day in a year may have different t_{MAX} and t_{MIN}, T_{MAX} mostly occurs after midday and T_{MIN} occurs shortly after sunrise (Guo et al. 2014; Izquierdo et al. 2002). The time series of average monthly t_{MAX} and t_{MIN} are utilized as the model input data to account for the monthly variations of t_{MAX} and t_{MIN} for all grids within a climate division.

Δt_{MLT} and Δt_{RFR} are the bases of the two triangles in Figure 3.3b and are calculated based on the time-intercept of the line between T_{MIN} and T_{MAX} with 0°C (Equation 2). Eventually, snowmelt and refreezing for each day are computed using the areas of the two triangles. The HTIM also incorporates the standard TIM for days, in which both T_{MIN} and T_{MAX} are above/below 0°C. According to the HTIM, the snowmelt and refreezing for different T_{MIN} and T_{MAX} values are written as:

$$M = \begin{cases} C_M T_{AVE} \Delta t & T_{MIN} > 0 \;\&\; T_{MAX} > 0 \\ C_M \dfrac{T_{MAX}}{2} \Delta t_{MLT} & T_{MIN} \leq 0 \;\&\; T_{MAX} > 0 \end{cases} \tag{3.5}$$

$$R = \begin{cases} C_F T_{AVE} \Delta t & T_{MIN} \leq 0 \;\&\; T_{MAX} \leq 0 \\ C_F \dfrac{T_{MIN}}{2} \Delta t_{RFR} & T_{MIN} \leq 0 \;\&\; T_{MAX} > 0 \end{cases} \tag{3.6}$$

where R is the potential refrozen meltwater (mm), C_F is a freezing factor (mm $^{o}C^{-1}$ day^{-1}), and Δt_{MLT} and Δt_{RFR} represent the defacto melting and freezing periods (day). The Δt_{MLT} and Δt_{RFR} required to compute snowmelt for a sample day with fluctuations in T_{MIN} and T_{MAX} on either side of 0°C are depicted in Figure 3.3b.

3.4.3. Development of a Macro-scale Snow Accumulation and Ablation Model

A macro-scale snow model (MSM) is developed to simulate the dynamics of snow accumulation and ablation. The MSM is a grid-based daily model that discretizes the land surface into user-defined square grids. The model utilizes a user-defined transitional temperature range (TTR) to distinguish three different precipitation forms (i.e., rainfall, snowfall, and mixed rainfall and snowfall). The TTR provides the flexibility of selecting a proper temperature range based on the characteristics of specific regions. When T_{AVE} is lower than or equal to the lower bound of the TTR (TT_{MIN}), precipitation is assumed to be snowfall. When T_{AVE} is higher than or equal to the upper bound of the TTR (TT_{MAX}), precipitation is considered in the form of rainfall. If T_{AVE} falls within the TTR, a mixed form of rainfall and snowfall is considered; assuming that snowfall decreases linearly from TT_{MIN} to TT_{MAX}.

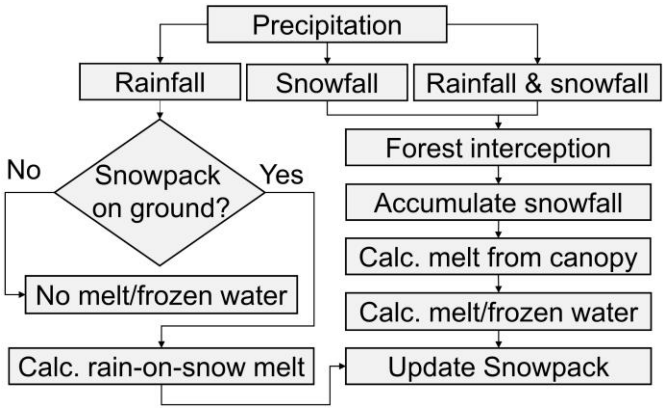

Figure 3.4. Flowchart of the macro-scale snow model (MSM).

Figure 3.4 shows the flowchart of the MSM and the three different precipitation forms. The MSM simulates dynamic snowpack storage, snowmelt, rain-on-snow, and refrozen meltwater. If precipitation is in the form of snowfall or a combination of rainfall and snowfall, the snowpack water equivalent is updated based on the forest canopy snow interception, snowfall accumulation, and melting/refreezing processes (Figure 3.4). If precipitation is solely in the form of rainfall, the simulated processes vary depending on the availability of snowpack on the ground (Figure 3.4).

Snowpack water equivalent is updated based on the amount of snow reaching the ground surface, SNO_S (mm), actual snowmelt, and snowpack water equivalent of the previous time step:

$$SWE(t,g) = SWE(t-1,g) - M_A(t-1,g) + C_{SN} \times SNO_S(t,g) \quad (3.7)$$

where SWE (mm) is the snowpack water equivalent, M_A is the actual snowmelt (mm), and C_{SN} is a snowfall correction factor and accounts for the losses from sublimation and redistribution (Anderson 2006). C_{SN} can be ignored for cold-climate regions with a significant amount of snow and multiple snowfall events. However, it cannot be neglected for areas with a small number of snowfall events, since the losses for these regions are typically higher (Anderson 2006). C_{SN} is suggested to vary between 0.7-1.6 (Anderson 2002).

The actual snowmelt, M_A (mm), is calculated based on the available water for melt, AWM (mm), and a maximum snowpack water retention storage (SPR_{MX}):

$$M_A(t,g) = Max[0, (AWM(t,g) - SPR_{MX}(t,g))] \quad (3.8)$$

in which SPR_{MX} acts as a threshold for the snowmelt generation process. The snowpack water retention storage (SPR) retains meltwater until reaching SPR_{MX}. In other words, SPR_{MX} is a threshold to delay the generation of snowmelt. The water stored in SPR can refreeze when the temperature is below 0°C, and the amount of SPR_{MX} is simulated as a fraction of SWE:

$$SPR_{MX}(t,g) = C_{WR} \times SWE(t,g) \quad (3.9)$$

where C_{WR} is the coefficient of water retention storage, generally equal to 0.1 suggested by Bergström (1992).

In Equation 8, the available water for melt is the summation of meltwater from different sources minus the refrozen meltwater:

$$AWM(t,g) = M_F + M_R + M - R \quad (3.10)$$

where M_F is the snowmelt from forest canopy (mm), M_R is the rain-on-snow melt (mm), and M and R are the surface snowmelt and refreezing (mm) described in Section 3.2.

To calculate the amount of snowmelt from the forest canopy, the MSM uses a simple bucket approach to estimate snow interception by the forest canopy. The amount of snow reaching the ground surface, SNO_S (mm), for grid g and time step t is calculated by:

$$SNO_S(t,g) = SNO(t,g) - INT_{SN}(t,g) \tag{3.11}$$

where SNO is the total snowfall (mm) and INT_{SN} is the snow canopy interception (mm), which can be estimated by (Hedstrom and Pomeroy, 1998; Pomeroy et al., 1998):

$$INT_{SN}(t,g) = C_{CU} \times [FCS_{MX}(g) - SWE_F(t-1,g)] \times \left(1 - e^{-\frac{FVC \times SNO(t,g)}{FCS_{MX}(g)}}\right) \tag{3.12}$$

in which C_{CU} is a canopy unloading coefficient (~0.7), SWE_F is the snow storage water equivalent of the forest canopy (mm), FCS_{MX} is the maximum forest canopy snow storage (mm), and FVC is the fractional vegetation cover. FCS_{MX} and FVC are estimated by using the leaf area index (LAI) and snow density (Pomeroy et al. 1998; Schmidt and Gluns 1991).

Daily snowmelt from the forest canopy, M_F (mm), is calculated by incorporating a simple TIM (Liston et al. 2006), assuming that the amount of refreezing is negligible:

$$M_F(t,g) = \begin{cases} C_{FM} T_{AVE}(t,g) & T_{AVE} > 0 \\ 0 & T_{AVE} \leq 0 \end{cases} \tag{3.13}$$

where C_{FM} is the forest melting factor (C_{FM}). It should be noted that since the snowmelt from the forest canopy is much lower than the surface snowmelt, the original TIM was used for simulating snowmelt from the forest canopy.

The amount of meltwater from a rain-on-snow event, M_R (mm), is calculated when precipitation is in the form of rainfall and there is snowpack on the ground. Assuming that the rainfall temperature is equal to T_{AVE} and the snow surface temperature is 0°C, the amount of M_R is simulated by using the following equation (Qi et al. 2017), in which RNF is rainfall (mm):

$$M_R(t,g) = 0.0126 \times T_{AVE}(t,g) \times RNF(t,g) \tag{3.14}$$

As discussed in the previous section, the MSM uses the HTIM to simulate the surface snowmelt and refreezing processes. Different studies suggested that C_M varies over time and space (e.g., Fontaine et al. 2002; Rango and Martinec 1995). To calculate the seasonally variable

melting factor, MSM incorporates the approach proposed by Fontaine et al. (2002) and Neitsch et al. (2011):

$$C_M = \frac{C_{MX} + C_{MN}}{2} + \sin\left[\frac{2\pi(D_N - 81)}{365}\right] \times \frac{C_{MX} - C_{MN}}{2} \quad (3.15)$$

where C_{MX} is the maximum melting factor, C_{MN} is the minimum melting factor, and D_N is the number of days in the year. In cold climate regions where snow accumulation may continue until mid or late spring, C_{MX} is of greater importance while C_{MX} and C_{MN} are both equally important in the areas with frequent snowmelt events during winter (Anderson 2006). In addition to the temporal variations of C_M, the spatial distribution of C_M for different grids is taken into account based on the land-use types. The values of the maximum and minimum melting factors for different land-use types are listed in Table 3.3. It is notable that forest covers typically have a small melting factor, whereas urban areas have larger melting factors (Table 3.3).

Table 3.3. Maximum and minimum melting factors (C_{MX} and C_{MN}) suggested for different land use types (Anderson 2006; Neitsch et al. 2011)

Land use description	**C_{MX}**	**C_{MN}**
Dense conifer forest	0.5-0.7	0.2-0.4
Mostly deciduous	1.0-1.4	0.2-0.6
Mostly open flat terrain	1.5-2.2	0.2-0.6
Mostly open mountainous terrain	0.9-0.3	0.1-0.3
Mixed cover	0.8-1.2	0.1-0.3
Rural areas	6.9	1.4
Urban areas	8.0	3.0

3.5. Results

3.5.1. Temporal Analysis of HTIM and TIM Simulations vs. SNODAS Snowmelt

The snowmelt results simulated by the HTIM and TIM are compared with the SNODAS snowmelt data to ensure that both methods provide acceptable simulations. Figures 3.5a-c depict the monthly/annual snowmelt over the MRB as well as a monthly graphical comparison

between the HTIM and TIM simulations and the SNODAS snowmelt data. Figure 3.5a highlights an extreme hydroclimatic discrepancy between WYs 2011 and 2012. WY 2011, as a wet year, accounted for higher snowmelt peaks and a longer extended snowmelt period, whereas WY 2012, as a dry year, had smaller peaks and a shorter snowmelt period. Reasonably, the magnitude of snowmelt peaks in both WYs highly depends on the amount of winter precipitation. Figure 3.5a indicates that the snowmelt peaks for both WYs occurred in March and April; however, as a direct result of higher winter precipitation in WY 2011, snowmelt peaks in WY 2011 were nearly two times larger than those in WY 2012. Comparing the simulation results by HTIM and TIM in Fig 5a reveals that both methods followed a similar simulation pattern.

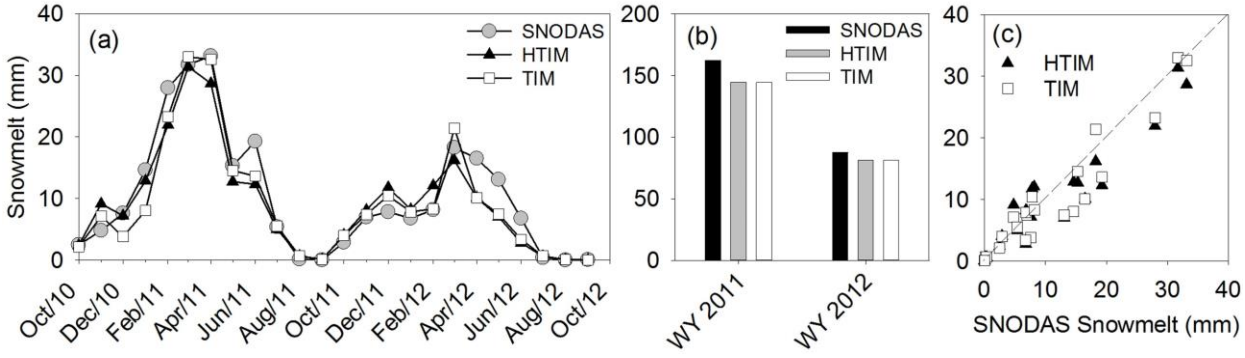

Figure 3.5. Snow Data Assimilation System (SNODAS) snowmelt data versus (a) monthly and (b) yearly snowmelt simulated by the hybrid temperature index method (HTIM) and the standard TIM for water years (WYs) 2011 and 2012; (c) graphical comparison between the HTIM and TIM simulations and the SNODAS snowmelt data.

Although there were discrepancies between the HTIM and TIM simulations in different months, the largest discrepancies occurred in December 2010, April 2011, and March 2012. Due to their temperature fluctuations, these three months play an important role in the variations of snowmelt in the MRB. For example, the results showed that the average snowmelt over the basin simulated by HTIM in December 2010 (i.e., 7.2 mm, which is closer to the SNODAS estimate of 7.6 mm) was 1.9 times higher than the snowmelt simulated by TIM (i.e., 3.8 mm). A statistical analysis of the simulated results showed that the coefficient of determination (R^2) for the monthly comparison was higher than 0.90 for both methods, indicating a good agreement

between the simulated snowmelt and the SNODAS data. The yearly comparison depicted in Figure 3.5b shows that the MRB in WY 2012 had an average snowmelt value of 87.69 mm, which is roughly half of the average snowmelt in WY 2011 (162.45 mm). The PBIAS analyses of the HTIM and TIM simulations against the SNODAS data revealed an average tendency that the simulated values were smaller than the corresponding SNODAS values. That is, both HTIM and TIM had negative PBIAS values (-9.77 and -9.78, respectively), indicating underestimation biases. Although HTIM and TIM demonstrated certain discrepancies in the monthly results, the differences between their annual averages were 1.2 Mm^3 and 23,011 m^3 in WY 2011 and WY 2012, respectively, corresponding to less than one millimeter of water over the basin area. Overall, Figures 3.5a and 5b indicate that HTIM and TIM snowmelt simulations are comparable to the SNODAS snowmelt estimates. The annual comparison also shows that the absolute errors between the simulated average snowmelt over the MRB and the SNODAS data in WYs 2011 and 2012 are less than 12%. The graphical comparison between the SNODAS and simulated snowmelt (Figure 3.5c) indicates that when snowmelt was less than 10 mm, both methods slightly overestimated the snowmelt. On the other hand, when snowmelt was greater than 10 mm, HTIM and TIM underestimated the snowmelt, which is in accordance with the PBIAS analyses for the simulated snowmelt results.

The variations between the SNODAS snowmelt and the simulated snowmelt by using MSM can be attributed to the underlying methodologies in formulating snowmelt in the two snow models. Specifically, MSM is a simple daily bucket model that only requires eight pre-defined parameters, while SNODAS is a multi-layered (three snow layers and two soil layers), spatially-distributed, energy and mass balance model which simulates snowmelt at hourly time steps based on the thermal dynamics of different layers (Barrett 2003). In addition to the differences in the methodologies, the variations between the SNODAS and simulated snowmelt values also stem from the inclusion of detailed meteorological datasets such as surface zonal wind, surface meridional wind, relative humidity, solar radiation, and many other variables in

SNODAS (Barrett 2003), whereas HTIM only utilizes widely available daily temperature datasets.

3.5.2. Spatial Analysis of HTIM and TIM Simulations vs. SNODAS Snowmelt Data

To understand the snowmelt variations over MRB, spatially distributed results are presented in three classes (i.e., low, moderate, and high) to facilitate the comparison between the simulated and SNODAS snowmelt results (Figures 3.6a-l). The classification was performed based on the Jenks natural breaks classification method (Jenks 1967) that finds the best arrangement of values in a given dataset. In order to pinpoint the differences between HTIM and TIM, three sample months were selected in which the largest discrepancy between the two methods occurred throughout the simulation period. Figures 3.6a-c indicate that the spatial distribution of snowmelt classes in HTIM resembled SNODAS better than TIM results. In comparison with TIM results, HTIM simulated larger Class 2 and Class 3 snowmelt in December 2010, which was attributed to the sub-daily temperature fluctuations around the freezing temperature throughout December 2010 when on average 53.25% of the basin experienced $T_{MIN}<0$ and $T_{MAX}>0$. Figure 3.6d highlights the differences in the three snowmelt classes simulated by HTIM, TIM, and SNODAS. Specifically, the coverage percentage of Class 3 (i.e., high) snowmelt by HTIM was 3.5 times larger than the coverage percentage of the Class 3 snowmelt by TIM which led to the generation of 3.38 mm more snowmelt over the basin, specifically in high elevation western parts of MRB.

Although HTIM simulated more snowmelt in December 2010, TIM simulated 32.2% more snowmelt than the HTIM in March 2012. Particularly, HTIM resulted in an average of 16.20 mm of snowmelt over the basin, whereas TIM simulated 21.42 mm of snowmelt. The spatial coverages of three classes of snowmelt in March 2012 (Figures 3.6e-h) show a general resemblance between the HTIM and TIM simulated distributed results. However, there are nuances in the spatial distributions of snowmelt which are due to the temperature variations. On average, 88.30% of the basin was covered by areas with $T_{MIN}<0$ and $T_{MAX}>0$ in March 2012.

The average T_{MIN} over the basin was -2.83°C and the average T_{MAX} was 15.98°C, which led to different class coverages between HTIM and TIM (Figure 3.6h). The discrepancy ratios between the two methods for Classes 1, 2, and 3 in March 2012 were 1.2, 0.72, and 0.76, respectively. Snowmelt results in March 2012 indicated that both magnitude and distribution of the simulated snowmelt by HTIM were closer to SNODAS snowmelt. While TIM overestimated snowmelt by 17.4%, HTIM underestimated snowmelt only by 11% in March 2012.

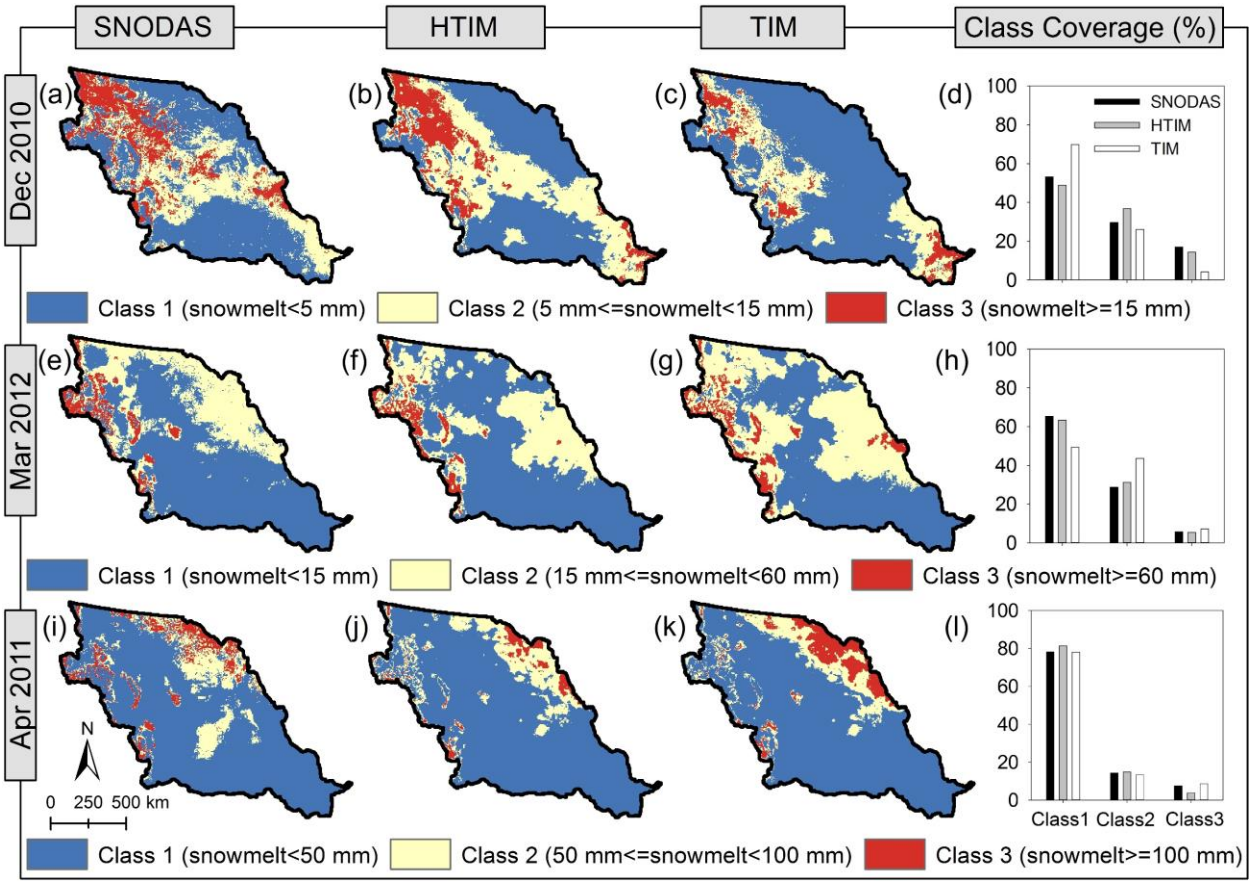

Figure 3.6. Monthly comparisons of the snowmelt coverages simulated by using the hybrid temperature index method (HTIM), the standard temperature index method (TIM), and the Snow Data Assimilation System (SNODAS) based on three classes of snowmelt (Class 1: low, Class 2: moderate, and Class 3: high) in December 2010 (a, b, c, and d), March 2012 (e, f, g, and h), and April 2011 (I, j, k, and l).

December 2010 and March 2012 were two months, in which the HTIM results were better than those from TIM and closer to the SNODAS snowmelt data. In some months, however, TIM provided better simulations than HTIM. For example, the difference between the

SNODAS and TIM snowmelt results in April 2011 was only 0.6 mm, which is much smaller than that of HTIM (4.46 mm). A closer look at the spatial distribution of the simulated snowmelt by SNODAS, HTM, and TIM reveals that TIM simulated more Class 3 snowmelt that was more comparable to the SNODAS data (Figures 3.6i-l). Specifically, 7.5%, 3.8%, and 8.6% of the basin was covered by Class 3 snowmelt simulated by SNODAS, HTIM, and TIM, respectively. The overall monthly results suggest that although there are some differences in both magnitude and spatial coverage of the snowmelt simulated by HTIM and TIM, these differences are only pronounced in the months when the majority of the basin experienced temperature fluctuations around the freezing temperature.

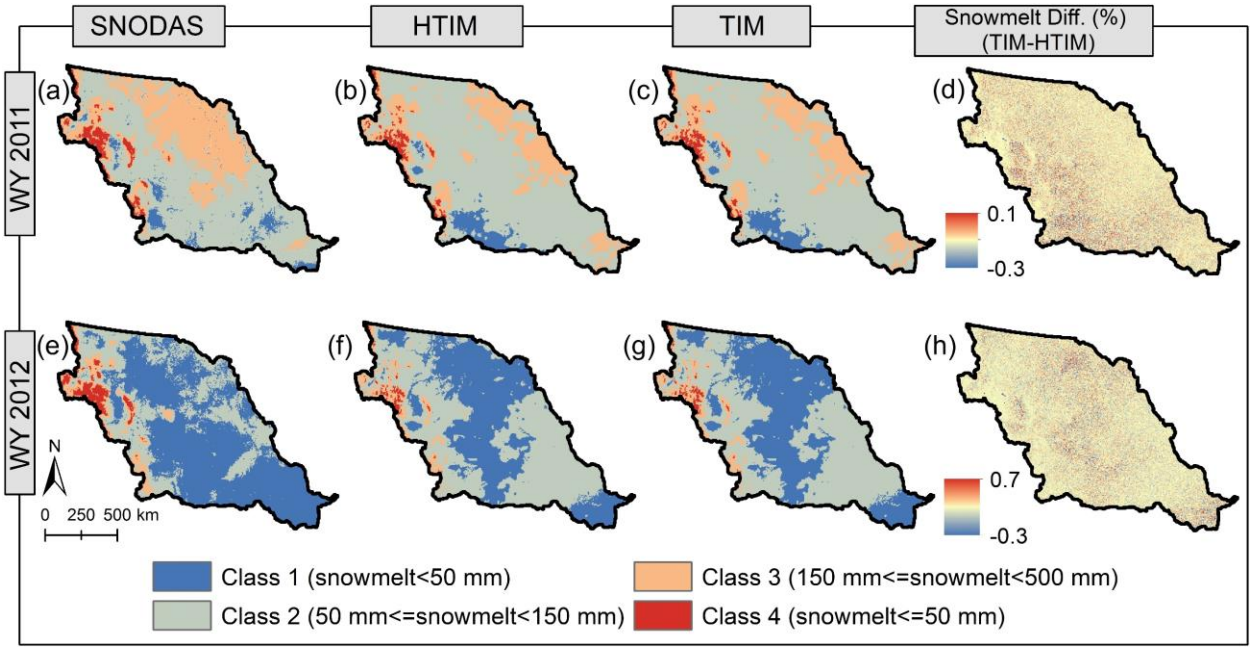

Figure 3.7. Yearly comparisons of the snowmelt coverages simulated by using the hybrid temperature index method (HTIM) and the standard temperature index method (TIM) based on three classes of snowmelt (Class 1: low, Class 2: moderate, and Class 3: high) in WY 2011 (a, b, and c) and WY 2012 (d, e, and f).

Figures 3.7a-h provide a comparison between the spatial distribution of snowmelt in WYs 211 and 2012 by SNODAS, HTIM, and TIM. Figures 3.7a-h highlight the relationship between the topography of the MRB and the snowmelt magnitude. Notably, the western side of the MRB, which is characterized by high altitudes (Figure 3.1c), accounts for a considerable

amount of snowmelt in both wet and dry years. WY 2011, as a wet year, accounted for more snowmelt mainly on the western and eastern sides of the basin (Figure 3.7a). Although the majority of the basin was covered by Class 2 snowmelt, Class 3 covered more than 33% of the basin and directly contributed to high snowmelt specifically in the upper MRB (Figure 3.7a). Both HTIM and TIM followed the general expected pattern of more snowmelt in the western and eastern parts in WY 2011, which is also in accordance with SNODAS (Figures 3.7a-c). However, spatial discrepancies are more pronounced specifically in Class 3 snowmelt, where the Class 3 in SNODAS results covered 11% more area than HTIM and TIM. Also, Figure 3.7b and Figure 3.7c suggest that there are only marginal differences in the class coverages of snowmelt between the HTIM and TIM which led to less than a millimeter difference in the annual snowmelt between the two methods (Figure 3.5b). Figure 3.7d depicts the difference percentage between the TIM and HTIM snowmelt simulations. From Figure 3.7d it can be observed that both methods resulted in very similar annual results, having the difference of less than 1% mostly concentrated in the western parts of the basin in WY 2011.

On the other hand, WY 2012, as a dry year, experienced lower snowmelt than WY 2011 (Figures 3.7e-g). Although Classes 1 and 2 covered more than 90% of the basin, the high-altitude western side of the basin was responsible for the majority of the snowmelt throughout the year (Figure 3.7e). Similar to WY 2011, a quantitative comparison of the three snowmelt coverage classes between the HTIM and TIM indicated that the discrepancy in the spatial distributions between the two methods was marginal (Figure 3.7f and Figure 3.7g). Similarly, the snowmelt values simulated over the basin by the two methods were close to each other, having an error of less than 1% (Figure 3.7h). Analyzing monthly, and yearly snowmelt simulations reveals that sub-daily temperature fluctuations around the freezing temperature play a role in monthly macro-scale snowmelt simulations, especially for the months in which a vast majority of the basin experiences $T_{MAX} > 0^{o}C$ and $T_{MIN} < 0^{o}C$. However, the impacts of sub-daily temperature fluctuations around the freezing temperature are marginal for the annual timescale.

3.6. Discussion

The differences between the monthly HTIM and TIM snowmelt results stemmed from the temperature variations in different months. In other words, T_{MAX} and T_{MIN} fluctuations around the freezing temperature led to higher/lower snowmelt simulated by HTIM than TIM in different months. Figure 3.8 depicts the variations of T_{MAX}, T_{MIN}, and T_{AVE} throughout the simulation period and two selected months (i.e., December 2010 and April 2011), in which contrasting temperature attributes occurred. Specifically, HTIM provided simulations closer to the SNODAS data in December 2010, while TIM yielded simulations closer to the SNODAS data in April 2011. The results indicated that the average T_{MAX} and T_{MIN} were respectively greater and smaller than 0°C in the MRB in 241 days (out of 731 days). Reasonably, the majority of these days (74%) occurred in the 5-month period from December to April (Figure 3.8a).

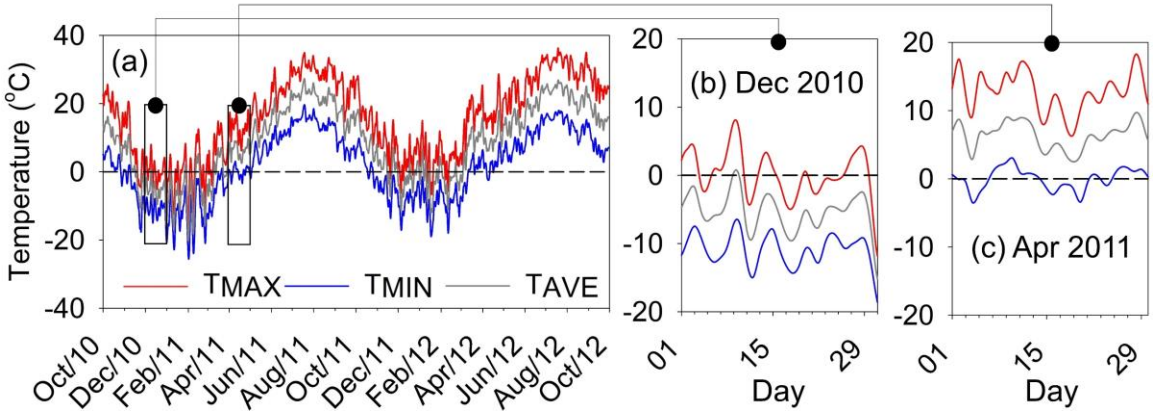

Figure 3.8. Variations of maximum, minimum, and average temperatures (T_{MAX}, T_{MIN}, and T_{AVE}) in (a) the simulation period, (b) December 2010, and (c) April 2011.

Figure 3.8b depicts the temperature variations in December 2010, in which the basin T_{AVE} was consistently lower than the freezing temperature except for one day (i.e., December 9th, 2010). The average T_{MAX} over the basin, however, repeatedly fluctuated above and below 0°C (16 days above and 15 days below 0°C). As a direct result of these fluctuations, the amount of snowmelt simulated by HTIM in December 2010 was 1.9 times greater than that from TIM (Figure 3.5a). In addition to the magnitude of the snowmelt generated in December 2010, the spatial distribution of the HTIM-simulated snowmelt in the MRB was closer to that of the

SNODAS snowmelt (Figures 3.6a-c). On the other hand, while T_{AVE} in the MRB was higher than 0°C in all days of April 2011, T_{MIN} fluctuated around the freezing temperature (15 days above and 15 days below 0°C) (Figure 3.8c). Reasonably, since HTIM incorporated T_{MIN} in its simulations, it resulted in 13.52% lower snowmelt (corresponding to 3.9 mm snowmelt over the basin) in comparison with the snowmelt from TIM in April 2011 (Figure 3.5a). Therefore, the TIM results were closer to the SNODAS snowmelt data, in both magnitude and spatial distribution (Figures 3.6i-k).

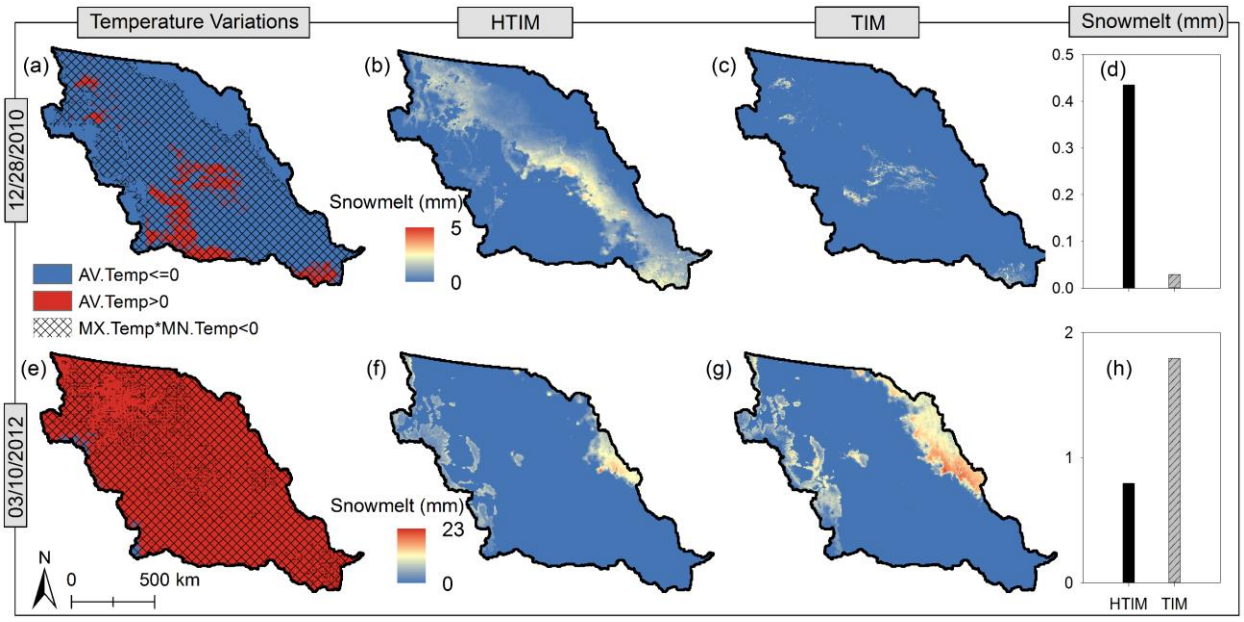

Figure 3.9. Daily comparisons of the temperature variations and snowmelt simulations by the hybrid temperature index method (HTIM) and the standard temperature index method (TIM) on December 28, 2010 (a, b, c, d); and March 10, 2012 (e, f, g, h) (AV. Temp: average temperature, MX. Temp: maximum temperature, and MN Temp: minimum temperature).

To better understand the differences between HTIM and TIM, two sample days (12/28/2010 and 3/10/2012) with contrasting temperature attributes were selected to showcase the impacts of sub-daily temperature fluctuations around the freezing temperature on daily snowmelt simulations. Figure 3.9 compares the temperature variations, quantity, and spatial distribution of the snowmelt simulated by the HTIM and TIM. The average temperature for 89.12% of the basin on December 28, 2010 was lower than 0°C, whereas the remaining 10.88% of the basin had temperatures higher than 0°C (Figure 3.9a). Figure 3.9a also indicates that

80.41% of the basin went through temperature fluctuations around 0°C, where T_{MAX} was higher and T_{MIN} was lower than the freezing temperature. These fluctuations significantly influenced the quantity and distribution of the simulated snowmelt. A visual comparison between Figure 3.9b and Figure 3.9c reveals that while snowmelt was solely limited to the areas with $T_{AVE} > 0°C$ in TIM, the HTIM generated snowmelt not only in the regions where T_{AVE} was greater than 0°C but also in the regions where T_{AVE} was lower than or equal to 0°C. In other words, the HTIM utilized the two extreme temperature variables (T_{MAX} and T_{MIN}) to recognize the days, in which snowmelt occurred only in a portion of the days. In such days, the HTIM had a higher potential to generate snowmelt in comparison to the TIM. Figure 3.9d confirms that the HTIM generated more snowmelt than the TIM. Specifically, the average amount of snowmelt simulated by the HTIM was 0.44 mm, whereas the TIM generated only 0.03 mm of snowmelt (93.18% lower than the HTIM value) on December 28, 2010.

The results differ for March 10, 2012. The average temperature for the majority of the basin on March 10, 2012 was higher than 0°C, and only 1.04% of the basin experienced temperatures lower than 0°C. The spatial analysis of T_{MAX} and T_{MIN} showed that T_{MAX} was higher than 0°C, and T_{MIN} was lower than the freezing temperature in 84.72% of the basin (Figure 3.9e). These temperature variations gave rise to a discrepancy in the snowmelt patterns between the two methods. A quantitative comparison of the spatial distributions of the snowmelt simulated by the HTIM and TIM shows that the HTIM generated snowmelt only over 16.33% of the basin (Figure 3.9f), while the TIM generated snowmelt over 24.48% of the basin (Figure 3.9g). This spatial differences in the snowmelt results directly translate to a difference in the magnitudes of the snowmelt simulated by the two methods. The TIM generated 1.80 mm of snowmelt, whereas the HTIM generated 0.79 mm of snowmelt on March 10, 2012, which is 43.89% lower than the TIM value (Figure 3.9h). Unlike December 28, 2010, the discrepancy between the snowmelt values simulated by the two methods for March 10, 2012, is due to the refreezing potential, which reduces the snowmelt generation potential over the basin in the

HTIM. Reasonably, the standard TIM cannot capture these variations in snowmelt and refreezing as the majority of the basin had temperatures higher than 0°C.

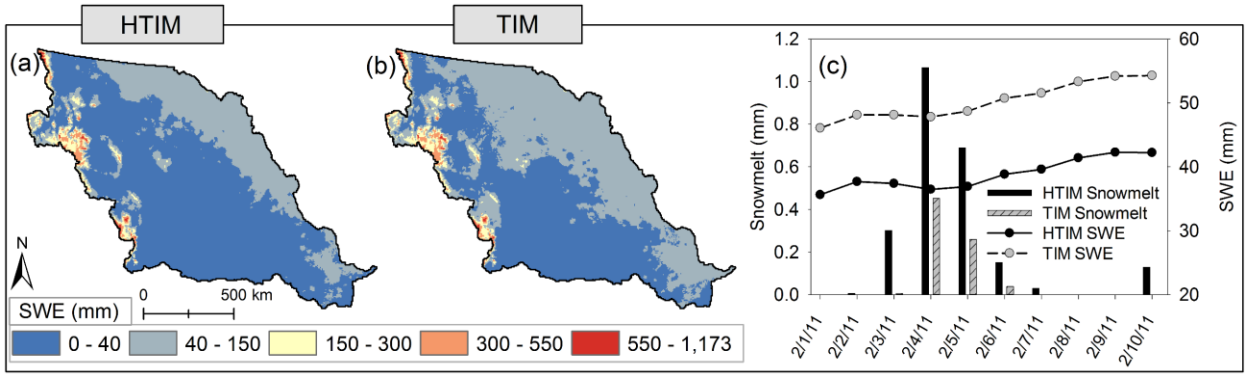

Figure 3.10. Snowpack water equivalent (SWE) simulations on 2/10/2011 using (a) the hybrid temperature index method (HTIM) and (b) standard temperature index method (TIM); and (c) a 10-day period comparison of the simulated snowpack and SWE using the two methods

The daily SWE was also affected by the temperature variations. Figure 3.10a and Figure 3.10b depict the SWE distribution over the basin on February 10, 2011, which had the maximum SWE during the simulation period. The spatial distribution of SWE indicates that regardless of the use of the HTIM or TIM, the high- and low-SWE regions were similar. However, the differences are pronounced when the magnitude of SWE is considered. For example, when the TIM was used as the snowmelt method, the average SWE over the basin on February 10, 2011 was 54.26 mm. On the other hand, the average SWE over MRB declined by 22.20% to 42.21 mm when the HTIM was used. Figure 3.10c depicts the snowmelt and SWE variations simulated by the HTIM and TIM for a 10-day period from 2/1/2011 to 2/10/2011. In this 10-day period, the HTIM simulated snowmelt was consistently higher than the TIM simulated snowmelt. The most substantial difference in the simulated snowmelt values by the two methods occurred on 2/4/2011 when the HTIM yielded 1.06 mm of snowmelt over the basin and the TIM simulated snowmelt was 57.55% lower than this value. Also, on 2/10/2011 the average temperature in the entire basin was lower than 0°C, which translates to no snowmelt based on the TIM method. However, since 38.71% of the basin experienced $T_{MAX}>0$, the HTIM resulted in 0.13 mm of snowmelt across the basin. The variations in the snowmelt patterns of the two methods during

the simulation period led to the variations of the SWE. Figure 3.10c indicates that because of the higher snowmelt simulated by the HTIM, SWE was consistently lower during the 10-day period when the HTIM was used.

TIMs have been traditionally compared to EBMs to evaluate their performances in hydrologic applications. Results from different studies indicate that the proper use of a snowmelt model is more significant than the model complexity (Mutzner et al. 2015). Therefore, efforts have been made to modify TIMs to achieve more accurate simulations by incorporating diurnal temperature variations, including shortwave or net radiation term, and using statistical distributions (e.g., Cazorzi and Dalla Fontana, 1996; Hock, 1999; Jost et al., 2012; Kane et al., 1997; Simoni et al., 2011; Tobin et al., 2013; Webb et al., 2017). For example, Simoni et al. (2011) modified the standard TIM taking into account both daily and hourly average temperatures in snowmelt simulations. The modified TIM was tested in a small (20 km^2) snowmelt-dominated alpine basin of the Swiss Alps, indicating that while the volume of snowmelt was highly correlated to the daily average temperature, hourly average temperatures were responsible for the shape of the snowmelt waves (Simoni et al. 2011). In another effort to capture diurnal variations of snowmelt simulations, Webb et al. (2017) utilized a two-parameter beta distribution function to imitate the diurnal snowmelt variations. The model was tested by using eight Snow Telemetry (SNOTEL) stations and the results fitted the diurnal snowmelt pattern with a root mean square error of 0.008 (Webb et al. 2017). Although different studies have improved the simulations of diurnal snowmelt variations at a point scale and small-scale basins by incorporating sub-daily temperature variations (e.g., Simoni et al., 2011; Tobin et al., 2013; Webb et al., 2017; Zaknic-Catovic et al., 2018), the impacts of temperature fluctuations around the freezing temperature at macro scales have not been well assessed.

Parallel to the results from small-scale studies, the results from this study also showed that daily macro-scale snowmelt and snowpack variations could be directly attributed to the sub-daily temperature variations. However, larger temporal resolutions (i.e., monthly or annual)

indicated less sensitivity to sub-daily temperature variations. Specifically, the comparisons of monthly simulated snowmelt by HTIM and TIM revealed that HTIM can generate either more or less snowmelt than the standard TIM, depending on the T_{MAX} and T_{MIN} distributions for certain months. The temperature variations in different months that led to the fluctuations in the snowmelt simulated by the two models can be observed in Figure 3.8a-c. The comparison between the annual HTIM and TIM simulations, however, revealed that both methods resulted in nearly identical snowmelt simulations. A question that remains unanswered is which method could provide more accurate macro-scale snowmelt results. The daily snowmelt analysis demonstrated that the HTIM is able to capture the temperature fluctuations and their impacts on the snowmelt and refreezing processes based on T_{MAX} and T_{MIN}, which can lead to a better understanding of other hydrologic processes. However, it should be noted that snowmelt is a complex process that, in addition to temperature, is subject to other terms of the energy balance equation and spatial variations (Hock 1999, 2003). Although the addition of T_{MAX} and T_{MIN} to the standard TIM can assist capturing the sub-daily temperature variations, it does not necessarily result in more realistic snowmelt simulations than the original TIM (e.g., April 2011). Therefore, since there are no other factors involved in HTIM than temperature, it can potentially overestimate or underestimate snowmelt, depending on the temperature distribution (e.g., Figure 3.9).

3.7. Summary and Conclusions

The objective of this study was to assess the impacts of sub-daily temperature fluctuations around the freezing temperature on the quantity and spatial distribution of macro-scale snowmelt simulations. A new daily macro-scale grid-based snow model was developed to simulate the dynamics of snow accumulation and ablation processes. Unlike other macro-scale models that rely upon a single daily average temperature, the developed model takes into account sub-daily temperature fluctuations by considering minimum and maximum temperatures and their occurrence timing. The model was applied to the Missouri River Basin

for water years 2011 and 2012, which represent two contrasting wet and dry years, respectively. The results were compared with those from the SNODAS snowmelt data to ensure that the HTIM provided comparable snowmelt results. Further, the HTIM snowmelt simulations were compared with those from a standard TIM to highlight the significance of the sub-daily temperature variations in macro-scale snowmelt simulations.

The HTIM snowmelt results were in a good agreement with the SNODAS data, having the coefficient of determination (R^2) and percent bias (PBIAS) of 0.90 and -9.7%, respectively. The absolute errors between the HTIM average snowmelt over the MRB and the SNODAS data in WYs 2011 and 2012 were less than 12%. The impacts of the sub-daily temperature fluctuations around the freezing temperature on snowmelt simulations were evaluated for two contrasting days to highlight the differences between HTIM and TIM. The daily results indicated that both magnitude and spatial distribution of the simulated snowmelt were significantly affected on the days in which the temperature fluctuates above and below the freezing temperature. The monthly comparisons between the HTIM and TIM showed that depending on the specific temperature variations in each month, the HTIM could yield either higher or lower snowmelt values. However, the discrepancy of the monthly results between the two methods was smaller than that of the daily simulation results. Analyzing the maximum, minimum, and average temperatures indicated that temperature fluctuated around the freezing temperature in almost two-thirds of the days in a five-month period from December to April. It was found that the average annual snowmelt results were not susceptible to the sub-daily temperature variations. The difference between the annual average snowmelt values in WYs 2011 and 2012 simulated by the HTIM and TIM was less than 1%, indicating the insensitivity of the annual results to sub-daily temperature fluctuations around the freezing temperature.

In summary, the modeling results from this study suggest that the daily snowmelt simulations were highly affected by the sub-daily temperature fluctuations, while the monthly and annual snowmelt results were less prone to such changes. The results from this study

indicate that although incorporating sub-daily temperature variations in a standard TIM can improve the physical-based representation of temperature in snow accumulation and ablation models, further investigation is required to thoroughly evaluate the performance of HTIM. Since snowmelt depends on different energy balance terms, in addition to temperature, HTIM has the potential to overestimate or underestimate snowmelt. Therefore, there is an opportunity for future efforts to incorporate widely available satellite datasets to improve the HTIM simulations.

3.8. References

Alcamo, J., Döll, P., Henrichs, T., Kaspar, F., Lehner, B., Rösch, T., and Siebert, S. (2003). "Development and testing of the WaterGAP 2 global model of water use and availability." *Hydrological Sciences Journal*, Taylor & Francis, 48(3), 317–337.

Anderson, E. (2002). *Calibration of Conceptual Hydrologic Models for Use in River Forecasting*. National Oceanic and Atmospheric Administration, National Weather Service Hydrology Laboratory, Silver Spring, MD.

Anderson, E. (2006). *Snow accumulation and ablation model—SNOW-17*. National Oceanic and Atmospheric Administration, National Weather Service Hydrology Laboratory, Silver Spring, MD.

Badger, A. M., Livneh, B., Hoerling, M. P., and Eischeid, J. K. (2018). "Understanding the 2011 Upper Missouri River Basin floods in the context of a changing climate." *Journal of Hydrology: Regional Studies*, Elsevier, 19, 110–123.

Barrett, A. P. (2003). *National Operational Hydrologic Remote Sensing Center SNOw Data Assimilation System (SNODAS) Products at NSIDC*. Special Report #11, Boulder, CO, USA: National Snow and Ice Data Center.

Bergström, S. (1992). *The HBV model: Its structure and applications*. Swedish Meteorological and Hydrological Institute, Norrköping, Sweden.

Boryan, C., Yang, Z., Mueller, R., and Craig, M. (2011). “Monitoring US agriculture: the US Department of Agriculture, National Agricultural Statistics Service, Cropland Data Layer Program.” *Geocarto International*, Taylor & Francis , 26(5), 341–358.

Braithwaite, R. J., and Olesen, O. B. (1989). “Calculation of Glacier Ablation from Air Temperature, West Greenland.” Springer, Dordrecht, 219–233.

Brubaker, K., Rango, A., and Kustas, W. (1996). “Incorporating radiation inputs into the snowmelt runoff model.” *Hydrological Processes*, John Wiley & Sons, Ltd, 10(10), 1329–1343.

Cazorzi, F., and Dalla Fontana, G. (1996). “Snowmelt modelling by combining air temperature and a distributed radiation index.” *Journal of Hydrology*, Elsevier, 181(1–4), 169–187.

Chu, X., Lin, Z., Tahmasebi Nasab, M., Zeng, L., Grimm, K., Bazrkar, M. H., Wang, N., Liu, X., Zhang, X., and Zheng, H. (2019). “Macro-scale grid-based and subbasin-based hydrologic modeling: joint simulation and cross-calibration.” *Journal of Hydroinformatics*, 21(1), 77–91.

Daly, C., Neilson, R. P., Phillips, D. L., Daly, C., Neilson, R. P., and Phillips, D. L. (1994). “A Statistical-Topographic Model for Mapping Climatological Precipitation over Mountainous Terrain.” *Journal of Applied Meteorology*, 33(2), 140–158.

Dunn, S. M., and Colohan, R. J. E. (1999). “Developing the snow component of a distributed hydrological model: a step-wise approach based on multi-objective analysis.” *Journal of Hydrology*, Elsevier, 223(1–2), 1–16.

Fontaine, T. A., Cruickshank, T. S., Arnold, J. G., and Hotchkiss, R. H. (2002). “Development of a snowfall–snowmelt routine for mountainous terrain for the soil water assessment tool (SWAT).” *Journal of Hydrology*, Elsevier, 262(1–4), 209–223.

Fuchs, B., Wood, D., and Ebbeka, D. (2012). “From Too Much to Too Little: How the Central US Drought of 2012 Evolved Out of One of the Most Devastating Floods on Record in 2011.”

National Integrated Drought Information System, <https://www.drought.gov/drought/node/439> (Nov. 29, 2018).

Fuka, D. R., Easton, Z. M., Brooks, E. S., Boll, J., Steenhuis, T. S., and Walter, M. T. (2012). "A Simple Process-Based Snowmelt Routine to Model Spatially Distributed Snow Depth and Snowmelt in the SWAT Model [1]." *JAWRA Journal of the American Water Resources Association*, Wiley/Blackwell (10.1111), 48(6), 1151–1161.

Guo, C.-Y., Pan, W.-C., Chen, M.-J., Tsai, C.-W., Chen, N.-T., and Su, H.-J. (2014). "When Are We Most Vulnerable to Temperature Variations in a Day?" *PLoS ONE*, 9(12), e113195.

Hedstrom, N. R., and Pomeroy, J. W. (1998). "Measurements and modelling of snow interception in the boreal forest." *Hydrological Processes*, Wiley-Blackwell, 12(10–11), 1611–1625.

Hock, R. (1999). "A distributed temperature-index ice- and snowmelt model including potential direct solar radiation." *Journal of Glaciology*, Cambridge University Press, 45(149), 101–111.

Hock, R. (2003). "Temperature index melt modelling in mountain areas." *Journal of Hydrology*, 282(1–4), 104–115.

Hock, R. (2005). "Glacier melt: a review of processes and their modelling." *Progress in Physical Geography*, Sage PublicationsSage CA: Thousand Oaks, CA, 29(3), 362–391.

Izquierdo, N., Aguirrezábal, L., Andrade, F., and Pereyra, V. (2002). "Night temperature affects fatty acid composition in sunflower oil depending on the hybrid and the phenological stage." *Field Crops Research*, 77(2–3), 115–126.

Jansson, P., Hock, R., and Schneider, T. (2003). "The concept of glacier storage: a review." *Journal of Hydrology*, Elsevier, 282(1–4), 116–129.

Jenks, G. (1967). "The Data Model Concept in Statistical Mapping." *International Yearbook of Cartography*, 7, 186–190.

Jost, G., Dan Moore, R., Smith, R., and Gluns, D. R. (2012). “Distributed temperature-index snowmelt modelling for forested catchments.” *Journal of Hydrology*, 420–421, 87–101.

Kane, D. L., Gieck, R. E., and Hinzman, L. D. (1997). “Snowmelt modeling at small Alaskan Arctic watershed.” *Journal of Hydrologic Engineering*, American Society of Civil Engineers (ASCE), 2(4), 204–210.

Leavesley, G. H. (1989). “Problems of snowmelt runoff modelling for a variety of physiographic and climatic conditions.” *Hydrological Sciences Journal*, 34(6), 617–634.

Lindström, G., Pers, C., Rosberg, J., Strömqvist, J., and Arheimer, B. (2010). “Development and testing of the HYPE (Hydrological Predictions for the Environment) water quality model for different spatial scales.” *Hydrology Research*, 41(3–4).

Liston, G. E., Elder, K., Liston, G. E., and Elder, K. (2006). “A Distributed Snow-Evolution Modeling System (SnowModel).” *Journal of Hydrometeorology*, 7(6), 1259–1276.

Livneh, B., Hoerling, M., Badger, A., and Eischeid, J. (2016). *Causes for hydrologic extremes in the upper Missouri River basin*. National Oceanic and Atmospheric Administration.

Macek-Rowland, K. M., and Gross, T. A. (2011). *2009 Spring floods in North Dakota, western Minnesota, and northeastern South Dakota. USGS Scientific Investigations Report 2010-5225*, Reston, VA.

Mehta, V. M., Knutson, C. L., Rosenberg, N. J., Olsen, J. R., Wall, N. A., Bernadt, T. K., Hayes, M. J., Mehta, V. M., Knutson, C. L., Rosenberg, N. J., Olsen, J. R., Wall, N. A., Bernadt, T. K., and Hayes, M. J. (2013). “Decadal Climate Information Needs of Stakeholders for Decision Support in Water and Agriculture Production Sectors: A Case Study in the Missouri River Basin.” *Weather, Climate, and Society*, 5(1), 27–42.

Mutzner, R., Weijs, S. V., Tarolli, P., Calaf, M., Oldroyd, H. J., and Parlange, M. B. (2015). “Controls on the diurnal streamflow cycles in two subbasins of an alpine headwater catchment.” *Water Resources Research*, Blackwell Publishing Ltd, 51(5), 3403–3418.

National Centers for Environmental Information. (2018). “Land-Based Station Data.” <https://www.ncdc.noaa.gov/data-access/land-based-station-data> (Dec. 6, 2018).

National Operational Hydrologic Remote Sensing Center. (2004). “Snow Data Assimilation System (SNODAS) Data Products at NSIDC, Version 1. Snow Melt Runoff at the Base of the Snow Pack.” *NSIDC: National Snow and Ice Data Center, Boulder, Colorado, USA*, <https://nsidc.org/data/G02158> (Sep. 6, 2018).

Neitsch, S., Arnold, J., Kiniry, J., and Williams, J. (2011). *Soil and Water Assessment Tool (SWAT) theoretical documentation version 2009*. Texas Water Resources Institute, College Station, Texas.

NOAA’s Water Resource Services. (2009). “Annual Flood Loss Summary Reports To U.S. Army Corps of Engineers: Water year 2009.” <http://www.nws.noaa.gov/om/water/> (Nov. 13, 2018).

Ohmura, A. (2001). “Physical Basis for the Temperature-Based Melt-Index Method.” *Journal of Applied Meteorology*, 40(4), 753–761.

Oyler, J. W., Ballantyne, A., Jencso, K., Sweet, M., and Running, S. W. (2015a). “Creating a topoclimatic daily air temperature dataset for the conterminous United States using homogenized station data and remotely sensed land skin temperature.” *International Journal of Climatology*, Wiley-Blackwell, 35(9), 2258–2279.

Oyler, J. W., Dobrowski, S. Z., Ballantyne, A. P., Klene, A. E., and Running, S. W. (2015b). “Artificial amplification of warming trends across the mountains of the western United States.” *Geophysical Research Letters*, John Wiley & Sons, Ltd, 42(1), 153–161.

Pomeroy, J. W., Parviainen, J., Hedstrom, N., and Gray, D. M. (1998). “Coupled modelling of forest snow interception and sublimation.” *Hydrological Processes*, Wiley-Blackwell, 12(15), 2317–2337.

PRISM Climate Group. (2004). “Parameter-elevation Regressions on Independent Slopes Model: Precipitation Time Series Dataset.” *Oregon State University*, <http://www.prism.oregonstate.edu> (Sep. 6, 2018).

Qi, J., Li, S., Jamieson, R., Hebb, D., Xing, Z., and Meng, F.-R. (2017). “Modifying SWAT with an energy balance module to simulate snowmelt for maritime regions.” *Environmental Modelling & Software*, Elsevier, 93, 146–160.

Rango, A., and Martinec, J. (1995). “Revisiting the Degree-day Method for Snowmelt Computations.” *Journal of the American Water Resources Association*, Wiley/Blackwell (10.1111), 31(4), 657–669.

Schmidt, R. A., and Gluns, D. R. (1991). “Snowfall interception on branches of three conifer species.” *Canadian Journal of Forest Research*, NRC Research Press Ottawa, Canada, 21(8), 1262–1269.

Simoni, S., Padoan, S., Nadeau, D. F., Diebold, M., Porporato, A., Barrenetxea, G., Ingelrest, F., Vetterli, M., and Parlange, M. B. (2011). “Hydrologic response of an alpine watershed: Application of a meteorological wireless sensor network to understand streamflow generation.” *Water Resources Research*, 47(10).

Singh, P. R., Gan, T. Y., and Gobena, A. K. (2005). “Modified Temperature Index Method Using Near-Surface Soil and Air Temperatures for Modeling Snowmelt in the Canadian Prairies.” *Journal of Hydrologic Engineering*, 10(5), 405–419.

Stewart, I. T., Cayan, D. R., and Dettinger, M. D. (2004). “Changes in Snowmelt Runoff Timing in Western North America under a `Business as Usual’ Climate Change Scenario.” *Climatic Change*, Kluwer Academic Publishers, 62(1–3), 217–232.

Terink, W., Lutz, A. F., Simons, G. W. H., Immerzeel, W. W., and Droogers, P. (2015). “SPHY v2.0: Spatial Processes in HYdrology.” *Geoscientific Model Development*, 8(7), 2009–2034.

Tobin, C., Schaefli, B., Nicótina, L., Simoni, S., Barrenetxea, G., Smith, R., Parlange, M., and Rinaldo, A. (2013). “Improving the degree-day method for sub-daily melt simulations with physically-based diurnal variations.” *Advances in Water Resources*, Elsevier, 55, 149–164.

U.S. Bureau of Reclamation. (2016). *SECURE Water Act Section 9503(c)-Reclamation Climate Change and Water*. United States Bureau of Reclamation, Denver, Colorado.

USGCRP. (2018). *Impacts, Risks, and Adaptation in the United States: The Fourth National Climate Assessment, Volume II*. (D. R. Reidmiller, C. W. Avery, D. R. Easterling, K. E. Kunkel, K. L. M. Lewis, T. K. Maycock, and B. C. Stewart, eds.), Washington, DC.

Webb, R. W., Fassnacht, S. R., and Gooseff, M. N. (2017). “Defining the Diurnal Pattern of Snowmelt Using a Beta Distribution Function.” *Journal of the American Water Resources Association*, Blackwell Publishing Inc., 53(3), 684–696.

Wise, E. K., Woodhouse, C. A., McCabe, G. J., Pederson, G. T., and St-Jacques, J.-M. (2018). “Hydroclimatology of the Missouri River Basin.” *Journal of Hydrometeorology*, 19(1), 161–182.

World Meteorological Organization (WMO). (1986). *Intercomparison of models of snowmelt-runoff*. Operational Hydrology, Rep. 23, Geneva.

Žaknić-Ćatović, A., Howard, K. W. F., and Ćatović, Z. (2018). “Modification of the degree-day formula for diurnal meltwater generation and refreezing.” *Theoretical and Applied Climatology*, 131(3–4), 1157–1171.

Zuzel, J. F., and Cox, L. M. (1975). “Relative importance of meteorological variables in snowmelt.” *Water Resources Research*, 11(1), 174–176.

4. IMPACTS OF HIGH-RESOLUTION GRIDDED TEMPERATURE DATASETS ON MACRO-SCALE SNOWMELT SIMULATIONS IN MISSOURI RIVER BASIN[1]

4.1. Abstract

The objective of this study is to evaluate the impacts of two commonly used temperature databases, Parameter-elevation Relationships on Independent Slopes Model (PRISM) and Topography Weather (TopoWx), on the quantity and distribution of snowmelt in the Missouri River basin simulated by a new macro-scale grid-based model for two representative flood and drought years. The model incorporates a unique LEGO-fashion framework to account for within-grid heterogeneity. The snowmelt simulations were compared with the SNOw Data Assimilation System (SNODAS) estimates, indicating that both datasets provided comparable snowmelt to the SNODAS data ($R^2 > 0.91$). Comparing the simulated snowmelt between the two datasets also revealed that the average snowmelt varied up to 16.9% and the snowmelt variations were more pronounced in the areas with complex topography. The simulations suggested that even nuances in the snowmelt coverage led to significant changes in the quantity of simulated snowmelt.

4.2. Introduction

Climate models have projected a rising-temperature trend in the United States towards the mid-twenty-first century, irrespective of the selected Representative Concentration Pathway (RCP) scenarios (USGCRP 2018). The rising temperatures significantly affect the Missouri River basin (MRB), which covers the majority of the Northern Great Plains and is the home to distinct cultural, topographical, and agricultural regions in Montana, Dakotas, Wyoming, and Nebraska. The projected rising-temperature trend alters the snow accumulation and ablation processes in

[1] The material in this chapter was co-authored by Mohsen Tahmasebi Nasab and Dr. Xuefeng Chu. Mohsen Tahmasebi Nasab had primary responsibility for developing the new analysis procedure and modeling of the system. Mohsen Tahmasebi Nasab was the primary developer of the conclusions that are advanced here. Mohsen Tahmasebi Nasab also drafted and revised all versions of this chapter. Dr. Xuefeng Chu served as proofreader and checked analysis conducted by Mohsen Tahmasebi Nasab.

the Northern Great Plains and leads to a high degree of variability in terms of extreme wet and dry years such as the flood event in 2011 and the drought in 2012 (USGCRP 2018).

The 2011 water year experienced a near-record-breaking snowfall across the Rocky Mountains and eastward into the Northern Great Plains states (i.e., Montana, North Dakota, Wyoming, South Dakota, and Nebraska). A combination of cooler-than-normal temperatures persisting to the Spring and historic rainfalls in May and early June over Montana and North Dakota coinciding with rapid snowmelt in the region led to a devastating flood in the MRB (Badger et al. 2018; Livneh et al. 2016; U.S. Army Corps of Engineers 2012; van der Wiel et al. 2018). The 2011 flood resulted in widespread damages in several cities in the Northern Great Plains states with an estimated cost of over $2 billion U.S. dollars and 5 fatalities (National Weather Service 2012). Solely in Minot, North Dakota, one-third of homes were directly impacted by the flood, and nearly 11,000 people were forced to evacuate their homes (National Weather Service 2012). The 2011 flood was followed by the historic 2012 flash drought, which occurred as a result of the above-normal-temperatures and reduced the corn yield by 26% (Rippey 2015; U.S. Government Accountability Office 2014). According to the 2016 SECURE Water Act Report, temperature and precipitation will remain highly variable in the MRB during the twenty-first century (U.S. Bureau of Reclamation 2016). Since the temperature and precipitation variability will persist throughout the twenty-first century, understanding the snowmelt-related processes and improving their representation in hydrologic models can provide realistic modeling results in the MRB, which are vital to the regional agriculture and food production.

Quantity, distribution, and timing of snowmelt are intrinsically connected to climate variability and temperature variations (Stewart 2009). Different methods with varying levels of complexity are commonly used to simulate daily snowmelt as a result of temperature variations. Specifically, the temperature index methods (TIMs) deem the temperature variations as the most influential factor in snowmelt generation (Martinec 1960), whereas the energy balance

methods (EBMs) consider the impacts of other influential terms and account for the energy balance of a snowpack (Anderson 1968). Although EBMs improve the physical representation of the snowmelt processes and perform better than TIMs under specific conditions such as high humidity or for the areas with high wind speed (Debele et al. 2010), most macro-scale hydrologic models adopt a TIM to simulate snowmelt (Alcamo et al. 2003; Bergström 1992; Chu et al. 2019; Lindström et al. 2010; Terink et al. 2015). This is partly attributed to the intensive data requirements of EBMs, which require a wide range of data that must be either measured or estimated including air temperature, dew-point temperature, solar radiation, atmospheric pressure, wind speed, snow density, and precipitation and its temperature. Since TIMs provide comparable results to EBMs by employing only temperature datasets (World Meteorological Organization (WMO) 1986), macro-scale hydrologic models incorporate different versions of TIMs without significant loss of information.

Gridded temperature datasets provide spatially distributed temperature variations and are commonly used in macro-scale hydrologic models. These temperature variations are essential for simulating different hydrologic processes such as evapotranspiration and snowmelt. The gridded temperature datasets can be classified into (1) station-based datasets and (2) reanalysis datasets (Walton et al. 2018). The station-based datasets are created by interpolating the data obtained at individual stations and generating high-resolution gridded datasets that can be used as input data for hydrologic models. Although the station-based datasets are easy to implement, they are bound to the number of available stations. Moreover, the nuances in the type of instrumentation and the time of observations can impact the gridded results (Menne et al. 2009). The reanalysis datasets are generated by employing atmospheric models. Since the original resolution of the reanalysis datasets is too coarse (0.3^{o} to 5.0^{o} or approximately 33 km to 550 km, respectively) to be directly used for hydrologic applications, they are commonly downscaled to finer resolutions (Walton et al. 2018). For example, the North American Regional Reanalysis (NARR) temperature dataset (Mesinger et al. 2006) is

downscaled to 1/8^{o} resolution grids, resulting in the North American Land Data Assimilation System (NLDAS-2) dataset (Xia et al. 2012).

Several studies have used different approaches to compare various station-based and reanalysis datasets and assess their realism (Behnke et al. 2016; Daly et al. 2008; Newman et al. 2015; Oyler et al. 2015; Walton et al. 2018). For example, Behnke et al. (Behnke et al. 2016) evaluated the accuracy of eight commonly used downscaled reanalysis datasets in terms of their regional differences and mean values. The gridded datasets were compared to the station data, and the results highlighted that the interpolation methods influenced the downscaled data, even for stations located inside a grid (Behnke et al. 2016). To evaluate both station-based and reanalysis datasets, Walton *et al.* (2018) compared five station-based, two reanalysis, and one hybrid datasets with the daily station data in California. They also measured the accuracy of the datasets away from the stations in complex terrains and near the coastal regions and concluded that although the station-based datasets were in accordance with the station data, some datasets were very likely biased especially in the coastal areas and the areas with complex topography (Walton et al. 2018).

While there is a wealth of evidence from several studies on the differences among temperature datasets, there are limited details on the impacts and implications of different temperature datasets on macro-scale hydrologic modeling applications such as snowmelt simulations. The main objective of this study is to fill this gap by evaluating the impacts of two temperature datasets from the Parameter-elevation Relationships on Independent Slopes Model (PRISM) and Topography Weather (TopoWx) on the quantity and distribution of snowmelt over the MRB, which possesses a complex topography. Snow accumulation and ablation processes are simulated for two representative wet and dry years in the MRB (i.e., 2011 and 2012) by using a new macro-scale snow model that accounts for the effects of different land uses and employs a TIM for snowmelt modeling.

4.3. Methodology

4.3.1. Missouri River Basin Characteristics

The MRB is the largest United States Geological Survey (USGS) Water Resources Region covering about one-sixth of the total continental area of the United States (Figure 4.1a) and parts of two Canadian provinces. The basin plays a significant role in the agricultural economy of the Northern Great Plains and produces nearly 46% of wheat, 22% of grain corn, and 34% of cattle in the United States (Mehta et al. 2013). The Missouri River extends over 4,215 km (National Weather Service 2012) from its origins in the Rocky Mountains, Montana, and Wyoming and flows into the Mississippi River upstream in St. Louis, MO (Figure 4.1b). It is estimated that 25% to 34% of the basin's flow is generated from the upper snow-driven portion of the basin (Norton et al. 2014; Qiao et al. 2014) and the lower portion of the basin is driven by rainfall mainly in late spring and summer.

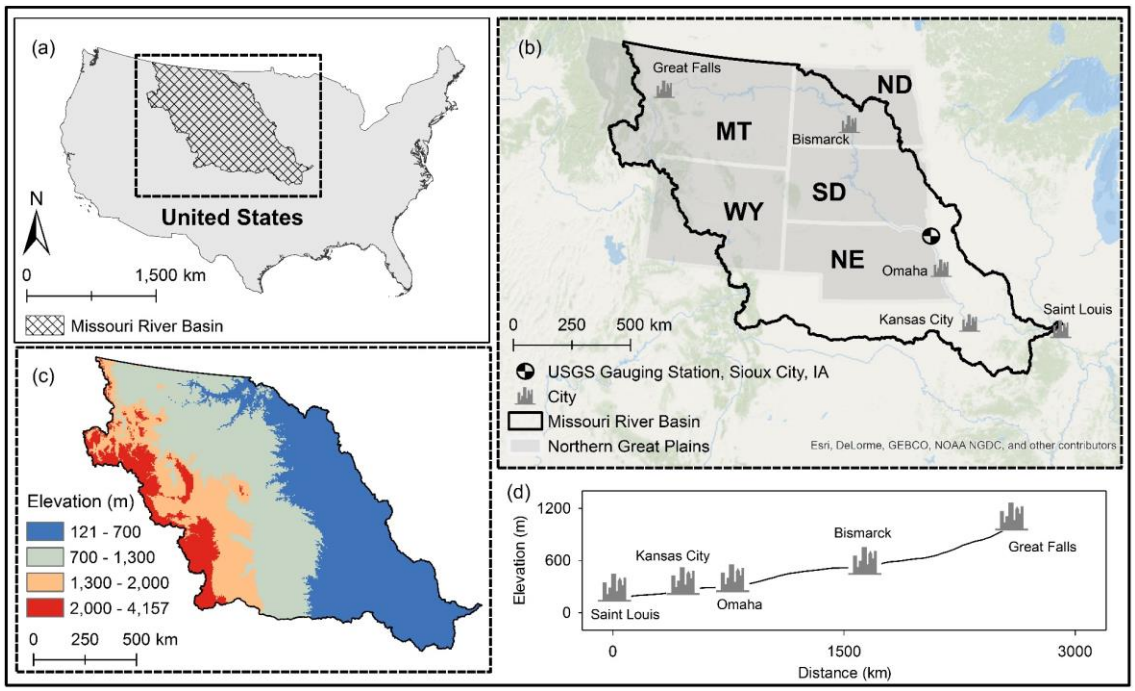

Figure 4.1. Missouri River Basin: (a) domain, (b) location with respect to the Northern Great Plains, (c) elevation variations within the basin, and (d) elevation drop from Great Falls, MT to Saint Louis, MO.

The MRB possesses unique hydro-topographical characteristics where the elevation drop from the highest points of the basin in the Rocky Mountains to its lowest points in the south-eastern side of the basin is more than 4 km. This significant elevation drop leads to substantial temperature variations and affects different hydrologic processes such as snowfall and snowmelt. For example, the elevation drop from Great Falls, MT to St. Louis, MO is more than 800 m (Figure 4.1d) and a decadal analysis of average temperatures (2009-2018) for two stations near Great Falls, MT and St. Louis, MO (Station IDs USC00248021 and USC00110137, respectively) indicates that the average temperature difference between the two stations is more than 5 ^{o}C (National Centers for Environmental Information, 2018).

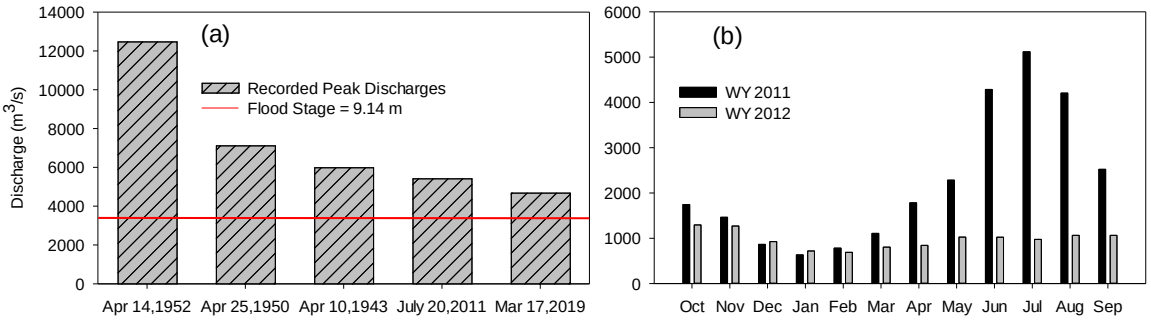

Figure 4.2. (a) recorded peak discharges as well as the flood stage and (b) the discrepancy between the observed streamflow discharges of the Missouri River at the Sioux City Station in water years (WYs) 2011 and 2012 (data from the United States Geological Survey).

Over the course of the last decades, the MRB has experienced several major floods and droughts with varying degrees of severity. Figure 4.2a depicts the five highest recorded peak discharges at the Sioux City Station (Figure 4.1b), in which the 2011 flood is the fourth largest flood. In March 2019, the flood stage (9.14 m) was overtopped again, which can be attributed to the high amount of snowfall received in the upper portion of the basin during the winter of 2018 and the subsequent snowmelt in the spring of 2019. In addition to frequent floods, the MRB has also experienced significant droughts such as a near-decadal drought in the first decade of the twenty-first century (Mehta et al. 2013). Figure 4.2b highlights the substantial discrepancy between the monthly discharges of the Missouri River at the Sioux City Station in water years

(WYs) 2011 and 2012. The observed discrepancy in spring and summer months pinpoints the critical role of snowmelt in the basin (Figure 4.2b).

4.3.2. Developing a Macro-scale Snow Accumulation and Ablation Model

Snow accumulation and ablation models simulate different processes, including the losses due to snow redistribution and sublimation, refrozen water, and snowmelt. Macro-scale hydrologic models usually have (1) subbasin-based or (2) grid-based modeling structures, in which different hydrologic processes are simulated within individual subbasins/grids (Chu et al. 2019). The grid-based structure has been adopted in several macro-scale models such as the variable infiltration capacity (VIC) model (Liang et al. 1994). One of the advantages of the grid-based structure is that it facilitates the incorporation of spatially distributed meteorological and hydrologic datasets (e.g., temperature) into hydrologic models (Chu et al. 2019).

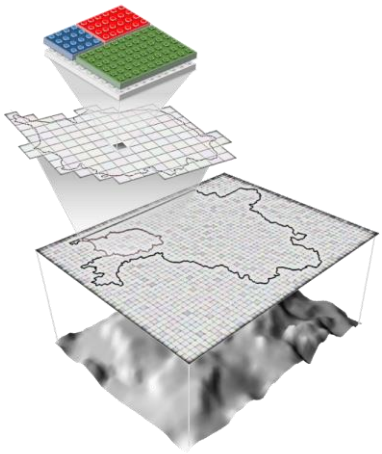

Figure 4.3. Horizontal structure of the developed snow accumulation and ablation model by considering a LEGO-fashion RGB (Red, Green, and Blue) block layout, in which the Blue Block represents open water, the Green Block represents forests and woods, and the Red Block represents other land uses.

In this study, a grid-based macro-scale snow accumulation and ablation model is developed in which a LEGO-fashion layout is employed to account for within-grid land use heterogeneities and variations (Figure 4.3). A land surface is discretized into a number of user-defined square grids where the grid resolution is determined based on the availability and resolution of the input data. First, each grid is deemed as a uniform LEGO plate, and then the

land use and land cover distribution of the study area is used to extract within-grid heterogeneities for each LEGO plate. Eventually, an RGB (Red, Green, and Blue) block layout is adapted to consider the land use variations within a plate, where the Blue Block represents open water, the Green Block represents forests and woods, and the Red Block represents other land uses (Figure 4.3). Similar to the SNODAS snowmelt dataset, the developed model does not simulate snowmelt processes in the Blue Block (i.e., open water) and a TIM is incorporated to estimate snowmelt generated from Red and Green Blocks. In addition, the model accounts for the impacts of forest interception and snowmelt in its Green Block. The simulated snowmelt for each grid is calculated based on the weighted average of the simulated snowmelt for each block and its coverage percentage.

The first step in the snow modeling is to separate precipitation into rainfall and snowfall. The majority of the hydrologic models use a single temperature threshold to separate rainfall and snowfall (e.g., Neitsch *et al.*, 2011). In this study, a transitional temperature range (TTR) is utilized to distinguish three different precipitation forms (i.e., rainfall, snowfall, and mixed rainfall and snowfall). If the average temperature is lower than or equal to the lower threshold of the TTR (TT_{MIN}), precipitation is in the form of snowfall. On the other hand, if the average temperature is higher than or equal to the upper threshold of the TTR (TT_{MAX}), precipitation is considered in the form of rainfall. When the average temperature falls within the TTR, a mixed rainfall and snowfall is considered by assuming a linear relationship between the upper and the lower thresholds of the TTR.

The snow interception from forest canopies is simulated solely for the Green Block, which represents forests and woods (Figure 4.3). The water equivalent depth of snow reaching the ground surface, SNO_S (mm), for grid g at time step t is expressed as:

$$SNO_S(t,g) = \begin{cases} SNO(t,g) - INT_{SN}(t,g) & Green\ Block \\ SNO(t,g) & Other\ Blocks \end{cases} \quad (4.1)$$

where SNO is snowfall (mm), and INT_{SN} is the snow interception (mm). For the Green Block, INT_{SN} is simulated by (Hedstrom and Pomeroy 1998; Pomeroy et al. 1998):

$$INT_{SN}(t,g) = C_{CU}[FCS_{MX}(g) - SWE_F(t-1,g)]\left(1 - e^{-\frac{FVC \times SNO(t,g)}{FCS_{MX}(g)}}\right) \quad (4.2)$$

in which C_{CU} is a canopy unloading coefficient (~ 0.7), SWE_F is the snow storage water equivalent of the forest canopy (mm), FCS_{MX} is the maximum forest canopy snow storage (mm), and FVC is the fractional vegetation cover. FCS_{MX} and FVC are usually estimated by using the leaf area index (LAI) and snow density (Pomeroy et al. 1998; Schmidt and Gluns 1991). Snowmelt from the canopy storage is then simulated by using a TIM (Liston et al. 2006), incorporating daily average temperature and a constant melting factor (C_{FM}).

The snowpack water equivalent is updated based on SNO_S, and snowpack water equivalent of the previous time step as follows:

$$SWE(t,g) = SWE(t-1,g) + C_{SN} \times SNO_S(t,g) \quad (4.3)$$

where SWE (mm) is the snowpack water equivalent, M_A is the actual snowmelt (mm), and C_{SN} is a snowfall correction factor that accounts for the losses from sublimation and redistribution (Anderson 2006) and is suggested to vary between 0.7-1.6 (Anderson 2002).

In addition to the canopy snowmelt, the model incorporates the TIM to simulate daily surface snowmelt and refreezing as follows:

$$M(t,g) = \begin{cases} C_M(t,g,k)T_{AVE}(t,g)\Delta t & T_{AVE} > 0 \\ 0 & T_{AVE} \leq 0 \end{cases} \quad (4.4)$$

$$R(t,g) = \begin{cases} C_F(t,g)T_{AVE}(t,g)\Delta t & T_{AVE} < 0 \\ 0 & T_{AVE} \geq 0 \end{cases} \quad (4.5)$$

where M and R are the snowmelt (mm) and refreezing (mm), respectively; C_M and C_F are the melting and freezing factors (mm $^oC^{-1}$ day^{-1}); and T_{AVE} is the daily average temperature (^oC) over time step Δt (day).

The seasonal variability of C_M is considered in the model by using a sinusoidal function as well as the maximum and minimum melt factors (C_{MX} and C_{MN}, respectively) for different land use types (Fontaine et al. 2002; Neitsch et al. 2011):

$$C_M = \frac{C_{MX} + C_{MN}}{2} + \sin\left[\frac{2\pi(D_N - 81)}{365}\right] \times \frac{C_{MX} - C_{MN}}{2} \quad (4.6)$$

where D_N is the number of days in the year. In addition to the seasonal variability, C_{MX} and C_{MN} vary for different blocks (i.e., land-use types). For example, C_{MX} and C_{MN} values for dense conifer forests vary between 0.5-0.7 and 0.2-0.4, respectively (Anderson 2006).

Rain-on-snow is another source of meltwater that is considered in the developed model. The amount of meltwater from a rain-on-snow event, M_R (mm), is only calculated when precipitation is in the form of rainfall and there is a snowpack on the ground. Assuming that the rainfall temperature is equal to T_{AVE} and the snow surface temperature is 0 ^oC, M_R is estimated by using the following equation (Qi et al. 2017), in which RNF is rainfall (mm):

$$M_R(t,g) = 0.0126 \times T_{AVE}(t,g) \times RNF(t,g) \quad (4.7)$$

The actual snowmelt is calculated based on the available water for melt, AWM (mm), and the maximum snowpack water retention storage, SPR_{MX} (mm), as follows:

$$M_A(t,g) = Max[0, (AWM(t,g) - SPR_{MX}(t,g))] \quad (4.8)$$

where AWM is the summation of meltwater from different sources (M_F, M_R, and M) minus the refrozen meltwater (R); SPR_{MX} is a threshold for the snowmelt generation process. The snowpack water retention storage (SPR) retains meltwater until reaching SPR_{MX}. In other words, SPR_{MX} is a threshold to delay the generation of snowmelt. The water stored in SPR can refreeze when the temperature is below 0 ^oC, and SPR_{MX} is computed as a fraction of snowpack water equivalent, SWE (mm):

$$SPR_{MX}(t,g) = C_{WR} \times SWE(t,g) \quad (4.9)$$

where C_{WR} is the coefficient of water retention storage, with the suggested value of 0.1 (Bergström 1992). Eventually, SWE is updated at the end of each time step based on the estimated amount of actual meltwater (M_A).

4.3.3. Design of the Study

The study area was divided into 54,144 grids of 5×5 km², and the land use data from the Cropland Data Layer (CDL) (Boryan et al. 2011) were used to estimate the RGB blocks for all grids. Moreover, daily precipitation data were obtained from the PRISM dataset (Daly et al. 2008) and were re-gridded to 5×5 km² grids. Two representative WYs 2011 and 2012 (October 1, 2010, to September 30, 2012) were selected to simulate the dynamic snowmelt processes in the MRB. WYs 2011 and 2012 were selected due to their unique hydroclimatic characteristics, representing two extreme conditions in the MRB: WY 2011 as a wet/flood year and WY 2012 as a dry/drought year. The PRISM and TopoWx temperature datasets (Daly et al. 2008; Oyler et al. 2015) were separately incorporated into the snow accumulation and ablation model to simulate snowpack and snowmelt for WYs 2011 and 2012.

Table 4.1. Parameters and their values in the snow accumulation and ablation model

Parameter	Unit	Description	Value
C_{SN}	-	Snowfall correction factor	0.96
TT_{MAX}	^oC	Upper threshold of TTR	5
TT_{MIN}	^oC	Lower threshold of TTR	1
C_{CU}	-	Forest canopy unloading coefficient	0.7
C_{WR}	-	Water retention storage coefficient	0.1
C_{MX}	mm $^oC^{-1}$ day^{-1}	Maximum melting factor	Varies
C_{MN}	mm $^oC^{-1}$ day^{-1}	Minimum melting factor	Varies
C_F	mm $^oC^{-1}$ day^{-1}	Freezing factor	0.05

The parameters used in the model and their values are listed in Table 4.1. The temporal and spatial distributions of the simulated snowmelt from both temperature datasets were compared against each other to evaluate the impacts of incorporating the two temperature datasets on snowmelt generation in the MRB. Moreover, the snowmelt results were compared

with the snowmelt data from the National Oceanic and Atmospheric Administration (NOAA) National Operational Hydrologic Remote Sensing Center (NOHRSC) SNOw Data Assimilation System (SNODAS) (National Operational Hydrologic Remote Sensing Center 2004).

4.3.4. PRISM vs. TopoWx

PRISM (Daly et al. 1994, 2008) is a station-based modeling system that provides estimates of eight climate elements including precipitation, maximum temperature, minimum temperature, mean temperature, mean dew point temperature, maximum and minimum vapor pressure deficit, and vapor pressure. Out of these elements, mean temperature and vapor pressure are derived from the maximum and minimum temperatures and mean dew point temperature, respectively. PRISM offers multiple datasets for the conterminous U.S. with a spatial resolution of 30 sec (~4 km) and different temporal resolutions. For example, AN81d dataset provides daily time series of different elements, and AN81m dataset offers monthly and annual time series. In this study, daily mean temperature dataset from AN81d was utilized in the snow accumulation and the ablation model. The mean temperature dataset in PRISM is derived by taking the arithmetic mean of the maximum and minimum temperature datasets. PRISM incorporates more than twenty station networks such as National Weather Service Cooperative Observer Program (COOP) in a Climatologically-Aided Interpolation (CAI) method, in which long-term average datasets are the predictor grids. PRISM uses a climate-elevation regression model, in which weights are assigned to stations based on different physiographic features such as elevation, coastal proximity, and the vertical atmospheric layer that are most significant at scales from 1-50 km (Daly et al. 2008). However, there is no adjustment to ensure temporal homogeneity of the time series and the generated gridded datasets may possess non-climatic variations which are attributed to the changes in station equipment and location (Walton et al. 2018).

TopoWx (Oyler et al. 2015) is another station-based modeling system that only provides grid-based daily and monthly minimum and maximum temperature datasets with a spatial

resolution of 30 arcsec (~800 m) for the conterminous U.S. from 1948 to 2016. All stations included in three networks with more than five years of data for each month are used in the TopoWx interpolation method. The three station networks used by TopoWx are the daily Global Historical Climatology Network (GHCN-D), the Remote Automatic Weather Stations (RAWS) network, and the Snowpack Telemetry (SNOTEL) network. Unlike PRISM, TopoWx takes into account the inhomogeneities of the input station data and applies a homogenization procedure by Menne and Williams (Menne et al. 2009). The interpolation process employs a moving window kriging and a geographically weighted regression. The grid-based temperatures are estimated based on the station observation data. In addition to several major topo-climatic factors, TopoWx incorporates remotely sensed observations of Land Skin Temperature (LST) obtained from the Moderate Resolution Imaging Spectroradiometer (MODIS), 8-day, 1-km LST product (Wan 2008). Since LST spatiotemporal variability is correlated with air temperature, LST is used as an auxiliary predictor to assist temperature interpolations where station observations are not available or sparse (Oyler et al. 2015).

Although both PRISM and TopoWx provide grid-based temperature datasets by using station networks, they may result in different spatiotemporal temperature variations. One of the key differences between the two datasets stems from the fact that TopoWx uses LST as an auxiliary predictor whereas PRISM incorporates a station weighting scheme based on several physiographical features such as coastal proximity. Oyler *et al.* (2015) found that LST has a strong relationship with minimum temperature and can explain the spatial variations between TopoWx and PRISM datasets. Their results for the northeastern climate division of Nevada suggested that PRISM generally showed a tendency towards warmer minimum temperatures for valleys and cooler minimum temperatures for mountains in comparison with TopoWx (Oyler et al. 2015). In this study, the downloaded PRISM and TopoWx datasets were re-gridded to 5×5 km^2 grids to evaluate the impacts of the two datasets on macro-scale snowmelt simulations.

4.4. Results and Discussion

4.4.1. Understanding the Differences in Temperature Datasets

Figure 4.4 depicts a comparison of the simulated snowmelt over the MRB by using the two different temperature datasets (i.e., PRISM and TopoWx) against SNODAS snowmelt estimates. The simulated snowmelt showed a comparable temporal variation to the SNODAS estimates (Figure 4.4a). The values of the coefficient of determination (i.e., R^2) for PRISM and TopoWx were 0.92 and 0.93, respectively. Although the simulated snowmelt results from the two datasets were close for smaller snowmelt values (Figure 4.4b), larger snowmelt values indicated more significant discrepancies between the PRISM and TopoWx snowmelt results. These discrepancies were more pronounced in March and April 2011 and 2012, signifying the peak snowmelt period in the MRB (Figure 4.4a). For example, while the average snowmelt generated in April 2011 using the TopoWx dataset was 32.49 mm, snowmelt generated by using the PRISM dataset was 35.97 mm. This 3.48-mm difference (equivalent to 4713.23 M m^3 in the MRB) in the simulated snowmelt can be directly attributed to the spatiotemporal variations in the two temperature datasets and the extent of these changes in critical months for snowmelt generation (i.e., March, April, and May) is higher than that in other months (Figure 4.4a).

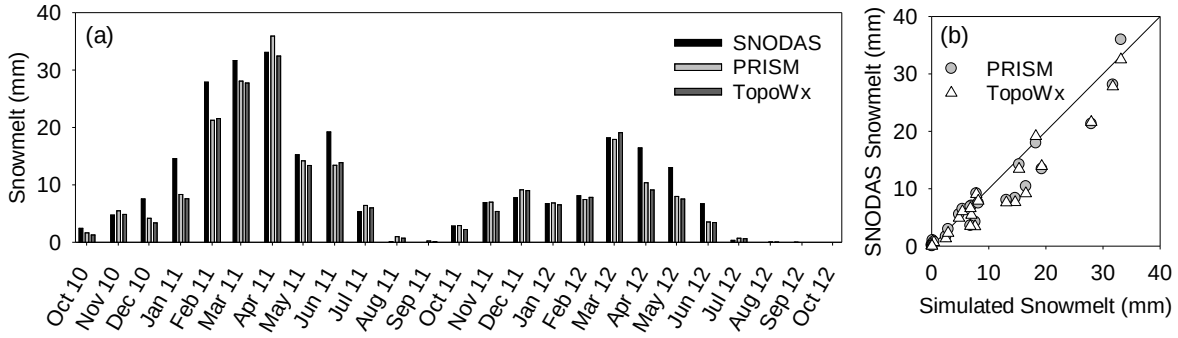

Figure 4.4. Snow Data Assimilation System (SNODAS) snowmelt estimates versus (a) simulated snowmelt using PRISM and TopoWx datasets for water years (WYs) 2011 and 2012; (b) graphical comparison between the simulations and the SNODAS snowmelt data.

Figure 4.5 shows the temperature variations across the MRB and the differences between the two temperature datasets in April 2011 and 2012. Both datasets indicated that the average

temperature variations in April 2011 followed a logical and expected trend where the northern and western parts of the basin were exposed to cooler temperatures, and warmer temperatures occurred in the southern parts of the basin (Figure 4.5a and Figure 4.5b). A visual comparison between TopoWx and PRISM temperature variations (i.e., Figure 4.5a and Figure 4.5b) reveals that TopoWx provided more spatial details, whereas PRISM variations were smoother and clear-cut. The observed smoothing pattern can be attributed to the different spatial resolution of the two datasets. Since PRISM original resolution (~4 km) is coarser than the TopoWx resolution (~800 m), it did not provide the detailed variations in average temperatures caused by the micro-scale variations. The accumulation of these micro-variations led to noticeable changes in the distribution of the average temperatures, specifically in the northwestern parts of the basin. For example, according to the TopoWx dataset, only 22.2% of the MRB was covered by < 4 ^{o}C temperatures, whereas the PRISM datasets accounted for 23.6% of the basin covered by < 4 ^{o}C temperatures. A grid-by-grid comparison between the two datasets reveals that 77.43% of the MRB experienced marginal temperature differences between -0.5 ^{o}C and 0.5 ^{o}C, mostly in the central and southern parts of the basin (Figure 4.5c). The comparison in Figure 4.5c shows that PRISM accounted for higher temperatures in 5.8% of the basin, mostly concentrated in the western side of the basin, typified by high elevations and complex topography. On the other hand, the TopoWx temperatures were higher, mostly in the central part of the basin. Similar to the findings by Oyler *et al.* (2015), the results from this comparison also suggest that the PRISM temperatures are generally warmer in valleys but cooler in the mountains in comparison with those of TopoWx in the complex topography of the western MRB.

Although 2011 and 2012 have different hydro-climatic characteristics, they share a similar temperature distribution with higher temperatures in the southern part and cooler temperatures in the northern and western parts of the basin (Figure 4.5d and Figure 4.5e). Both datasets provide a comparable average temperature distribution over the basin; however, the smoothing effect of the PRISM dataset is noticeable in the northern part of the basin (Figure

4.5e). The results from the spatial analysis of the TopoWx temperature dataset in April 2012 indicated that 18.2% of the basin was covered by temperatures between 4 °C and 8 °C. On the other hand, the PRISM temperature dataset indicated that 21.85% of the basin was covered with temperatures between 4 °C and 8 °C. Similar to the results of April 2011, the grid-by-grid temperature analysis for April 2012 revealed that the PRISM dataset accounted for warmer temperatures in the western part of the basin whereas the TopoWx temperatures were warmer in the central part of the basin (Figure 4.5f). Specifically, although 72% of the basin experienced marginal temperature differences (i.e., between -0.5 °C and 0.5 °C), the difference between the PRISM and TopoWx temperatures was higher than 0.5 °C in 5.2% of the basin, mainly in the western part, a critical snowmelt-driven region of the basin.

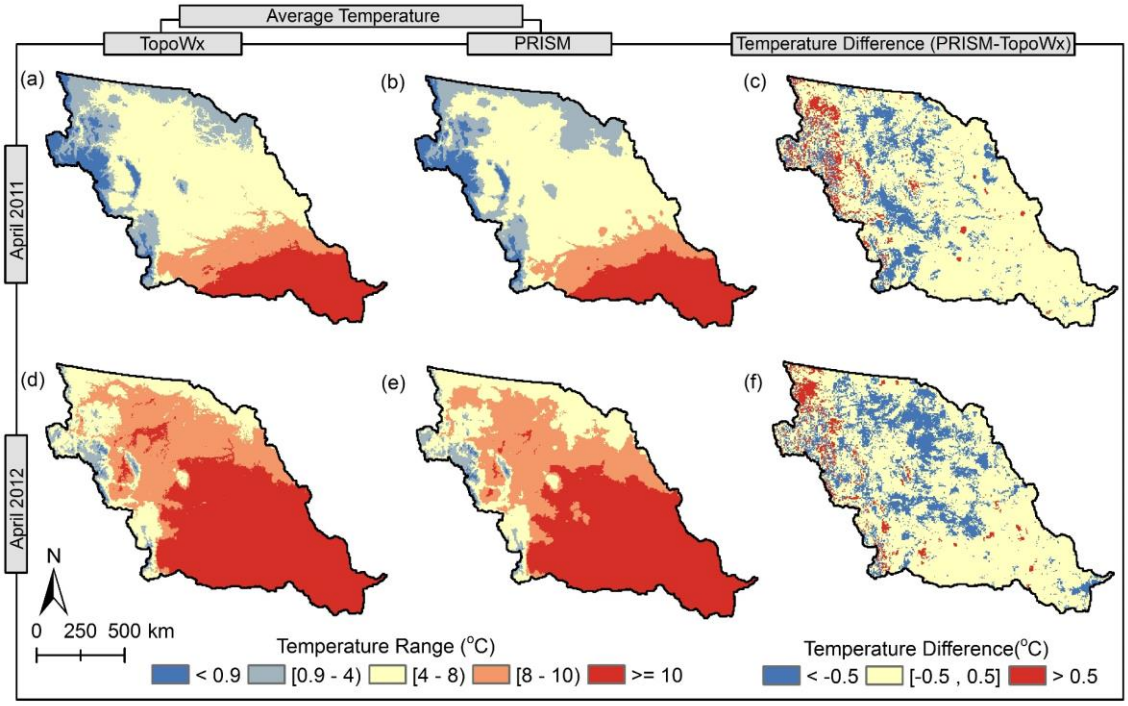

Figure 4.5. Average temperature distributions in the Missouri River Basin based on (a) TopoWx and (b) PRISM datasets; (c) average temperature differences between the two datasets in April 2011; average temperature variations based on (d) TopoWx and (e) PRISM datasets; and (f) average temperature differences between the two datasets in April 2012.

4.4.2. Impacts of Temperature Datasets on Snowmelt Simulations

The snowmelt analysis indicated that even subtle temperature variations between the two datasets could lead to notable snowmelt variations, particularly during spring months. For example, Figure 4.6 depicts the temperature and snowmelt variations for a sample day in March (i.e., 3/17/2011). Based on the PRISM temperatures, the majority of the basin had temperatures higher than 1 ^{o}C, and cooler temperatures were mostly concentrated on the high-elevation western side of the basin (Figure 4.6a). Specifically, the average temperatures in 43.98% of the basin varied between 1 ^{o}C and 8 ^{o}C, which played a crucial role in snowmelt generation on March 17, 2011. The simulated snowmelt was divided into three classes: low (Class 1), moderate (Class 2), and high (Class 3) snowmelt based on the Jenks natural breaks classification method (Jenks 1967) to facilitate the spatially distributed comparison of the generated snowmelt. The simulated snowmelt based on the PRISM temperature dataset suggested that the majority of snowmelt occurred in the eastern side of the basin (i.e., higher temperatures) and extended to the northern part (Figure 4.6b). The average snowmelt of the MRB on March 17, 2011 was 2.9 mm, and 70.7%, 19.2%, and 10.1% of the basin were covered by snowmelt Classes 1, 2, and 3, respectively (Figure 4.6c).

According to the TopoWx temperatures in the MRB on March 17, 46.30% of the basin was exposed to the average temperatures between 1 ^{o}C and 8 ^{o}C (Figure 4.6d), which was 2.32% (i.e., 31,403.5 km^{2}) greater than the percent area of the PRISM temperatures (Figure 4.6a). In addition to the dissimilar spatial variations between the two datasets, the results also revealed that the TopoWx grids with the average temperatures between 1 ^{o}C and 8 ^{o}C were on average 0.5 ^{o}C warmer than those of PRISM. A combination of the nuances in the spatial distribution and magnitude of the average temperatures led to a noticeable difference in the simulated snowmelt. A visual comparison between Figures 4.6e and 6b shows that when the TopoWx temperature dataset was used, Class 3 snowmelt (i.e., high snowmelt) covered more grids than those covered by the same class snowmelt simulated by using the PRISM dataset. Specifically, the simulated

Class 3 snowmelt covered 14.5% and 10.1% of the MRB when the TopoWx and PRISM datasets were used, respectively. These changes led to a 16.9% increase in the average snowmelt, which corresponds to 0.49 mm across the entire basin.

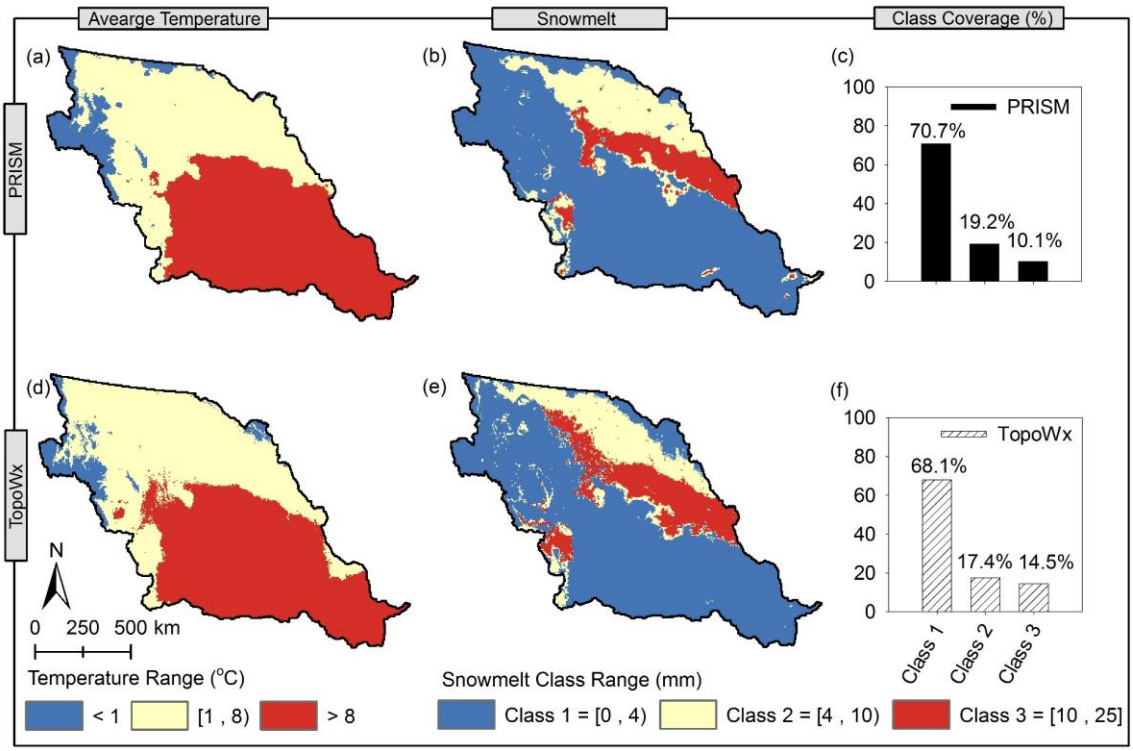

Figure 4.6. Average temperature distributions and the simulated snowmelt variations in the Missouri River basin on March 17th, 2011 for three classes: low (Class 1), moderate (Class 2), and high (Class 3) snowmelt based on the Jenks natural breaks classification method by using PRISM (a, b, and c) and TopoWx (d, e, and f).

Another noticeable trend in the simulated snowmelt using the two datasets was evident in complex topography. The snowmelt simulation results for the western side of the basin, which is characterized by complex topography, indicated that when TopoWx was used, more snowmelt was simulated (Figure 4.6b and Figure 4.6e). Figure 4.7 depicts the MRB's elevation distribution (Figure 4.7a) with a specific focus on a sample topographical feature on the western side of the basin (Figure 4.7b). The simulated snowmelt results showed that TopoWx snowmelt results imitated the topographical feature of the basin. The peak region accounted for lower snowmelt, and the base region accounted for higher snowmelt (Figure 4.7c). Although the PRISM snowmelt results provide the gist of the snowmelt variations with the topographical feature, the

differences between the TopoWx and PRISM snowmelt for the selected topographical feature are noticeable (Figure 4.7d). These variations between the generated snowmelt can be attributed to (1) the differences in the original spatial resolutions of the two datasets and (2) consideration of the auxiliary LST parameter in TopoWx.

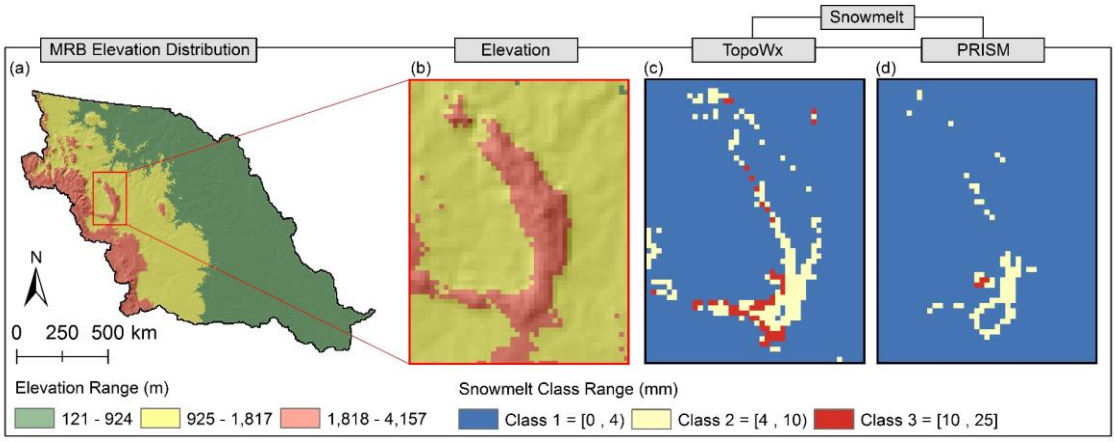

Figure 4.7. The Missouri River Basin's (a) elevation distribution, (b) a sample topographical feature on the western side of the basin, (c) TopoWx snowmelt classes, and (d) PRISM snowmelt classes.

The spatial variations of snowmelt in the MRB for different months in 2011 are shown in Figure 4.8. The snowmelt process began in February stretching from southeastern part to the northwestern part of the basin, regardless of the employed temperature dataset (Figure 4.8a and Figure 4.8b). The simulated snowmelt indicated that high snowmelt values were concentrated in the southeastern edges of the basin, which were exposed to warmer temperatures. The PRISM and TopoWx snowmelt simulations provided comparable distributions of low, moderate, and high snowmelt classes (Figure 4.8c). The PRISM snowmelt indicated that more than 50.4% of the basin was covered by Class 1 (i.e., low) snowmelt, which was 2% more than that of the TopoWx snowmelt results. On the other hand, both moderate and high snowmelt classes (i.e., Classes 2 and 3) had a slightly higher coverage percentage in the TopoWx snowmelt results (1.2% and 0.8% higher, respectively). The average snowmelt values in the MRB using the PRISM and TopoWx datasets were 21.6 mm and 21.3 mm, respectively, indicating that both

temperature datasets provided similar magnitude and distribution of snowmelt in February 2011.

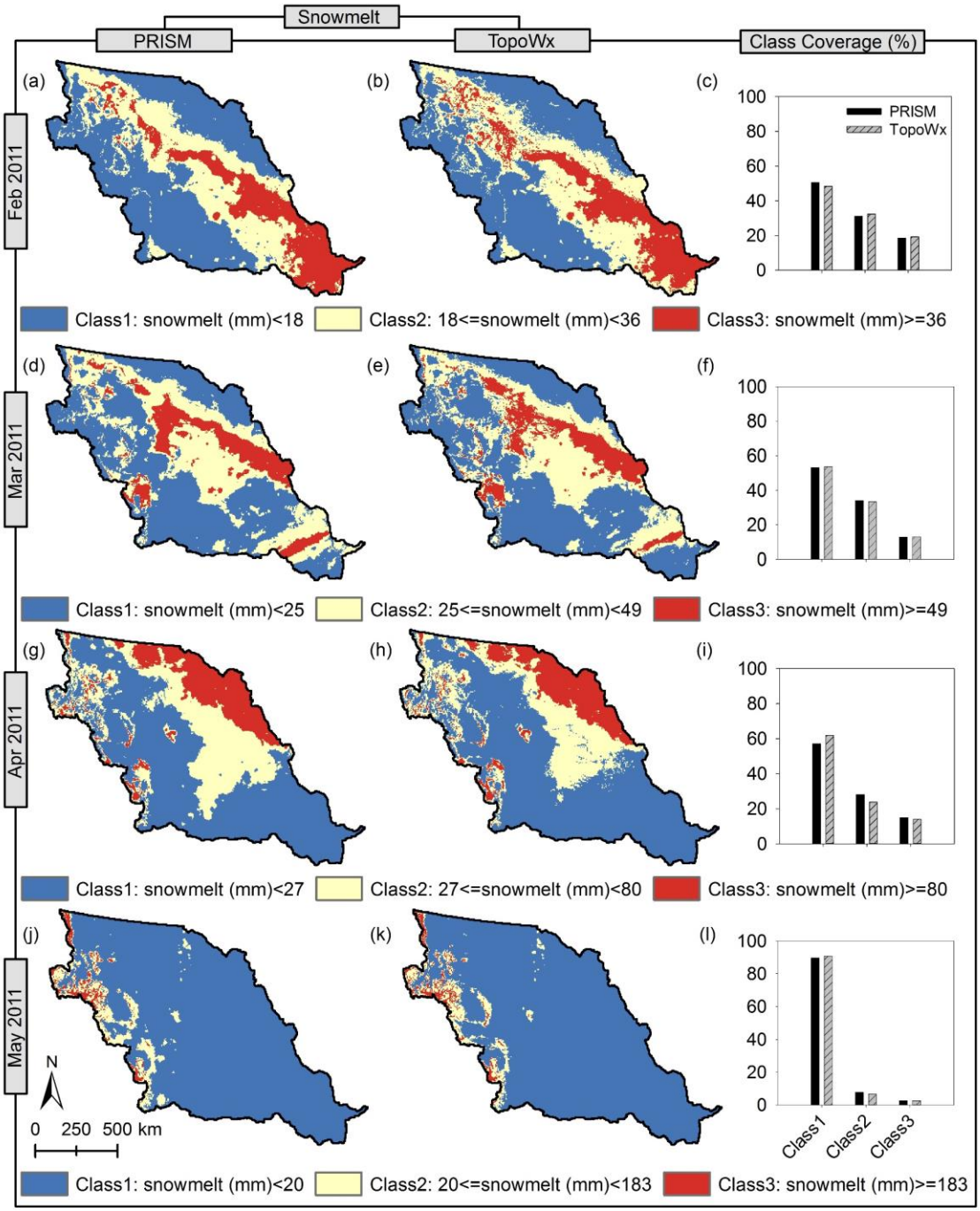

Figure 4.8. Monthly comparisons of the snowmelt coverage between the PRISM and TopoWx snowmelt results based on three classes of snowmelt (Class 1: low, Class 2: moderate, and Class 3: high) in February (a, b, and c), March (d, e, and f), April (g, h, and i), and May (j, k, and l) 2011.

A trend similar to that in February 2011 was observed for March 2011. Although high snowmelt values were slightly shifted towards the north, the overall distribution of the simulated snowmelt (Figure 4.8d and Figure 4.8e) resembled the snowmelt distribution in February 2011. The snowmelt class coverages had marginal nuances (less than 1%), which led to a marginal difference of 0.3 mm in the average snowmelt over the MRB (Figure 4.8f). Noticeable changes in the distribution and magnitude of the simulated snowmelt results appeared in April 2011 when the high-elevation western edges of the basin began contributing to the generated snowmelt in the MRB. Figures 4.8g and 8h depict that the high snowmelt regions of the basin shifted from the eastern part to the northeastern and western parts of the basin. In April 2011, more than 14% of the MRB generated high values of snowmelt (Class 3) and played a key role in the high streamflow in the Missouri River. Based on the TopoWx snowmelt results, only 23.9% of the basin was covered by Class 2 or moderate snowmelt, whereas the PRISM snowmelt results indicated the coverage percentage of 28.1% for Class 2 snowmelt. This 4.2% difference in the distribution of the moderate snowmelt values gave rise to a significant 3.5-mm difference in the average snowmelt over the entire basin in April 2011 when the PRISM snowmelt values were higher than those of TopoWx.

The snowmelt results in May 2011 highlighted the concentration of high snowmelt in the western part of the MRB (Figure 4.8j and Figure 4.8k). A visual comparison of the snowmelt distributions in February, March, April, and May 2011 shows that in the first three selected months (i.e., February, March, and April) snowmelt was mostly generated in the eastern and central parts of the basin. However, the snowmelt generated in May was mainly originated from the high-elevation western edges of the basin. Consequently, even subtle changes in Class 2 and Class 3 snowmelt coverages led to noticeable differences in the amount of generated snowmelt. The largest change in the distribution of snowmelt occurred in the Class 2 coverage where the PRISM snowmelt accounted for 7.7% of the basin, while the TopoWx snowmelt accounted for 6.5% (Figure 4.8l). This variation in the Class 2 snowmelt coverages caused a 0.8-mm difference

(equivalent to 1,082 Mm^3) in the average simulated snowmelt over the basin between the PRISM and TopoWx snowmelt results.

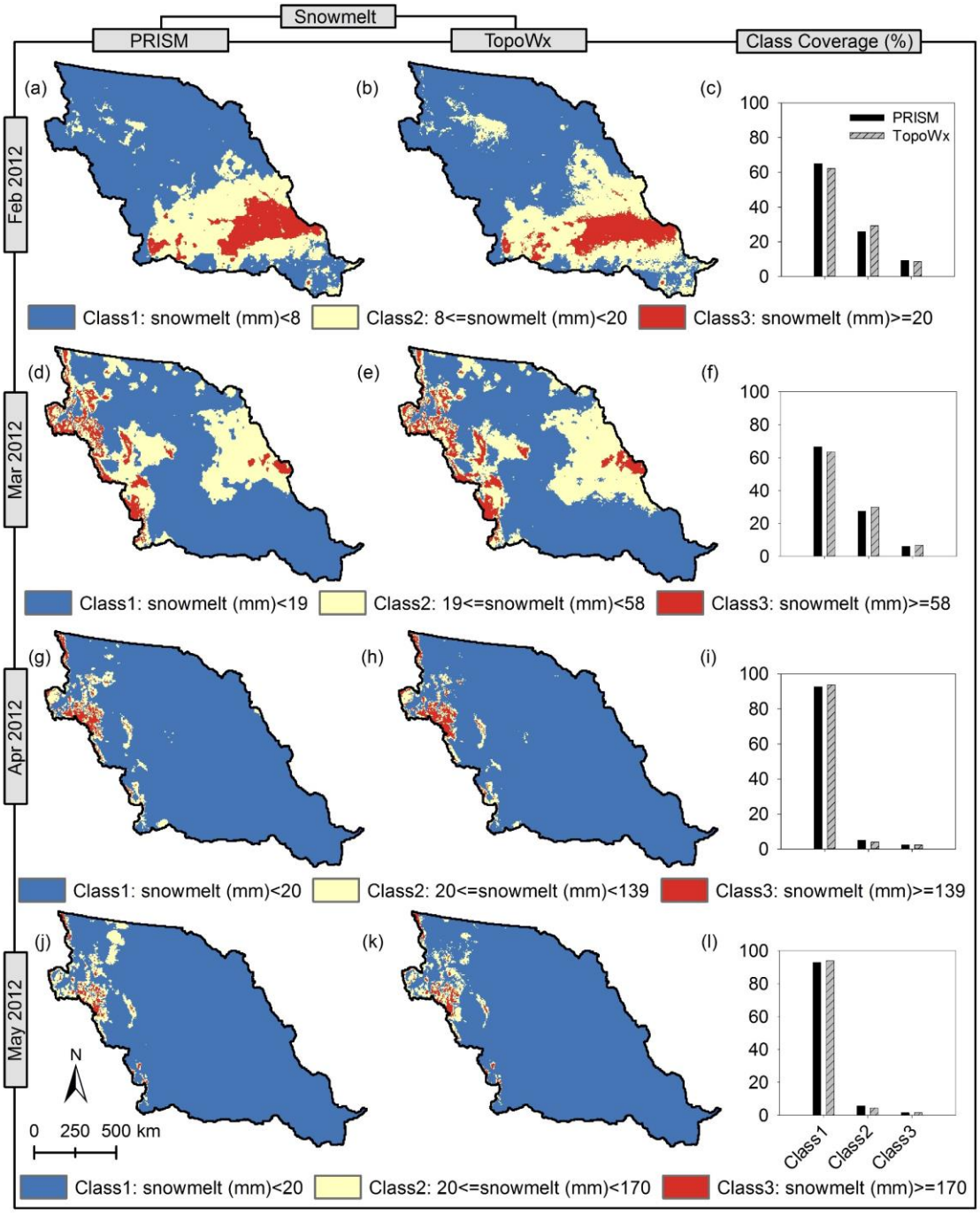

Figure 4.9. Monthly comparisons of the snowmelt coverages between the PRISM and TopoWx snowmelt results based on three classes of snowmelt (Class 1: low, Class 2: moderate, and Class 3: high) in February (a, b, and c), March (d, e, and f), April (g, h, and i), and May (j, k, and l) 2012.

The results from both datasets indicated that the quantity of snowmelt in WY 2012 was lower than that in WY 2011 for all months. This pattern was expected due to the hydroclimatic differences between the 2011 wet/flood year and the 2012 dry/drought year. For example, the simulated snowmelt results in March 2012 using the TopoWx and PRISM datasets showed sharp decreases of 45% and 56%, respectively, in comparison with those in March 2011. Figure 4.9 shows the comparisons of the snowmelt simulations and their class coverages in WY 2012. WY 2012 experienced higher temperatures than WY 2011, which directly led to an earlier generation of snowmelt in the central and southern parts of the basin in December and January 2012. Consequently, the high snowmelt concentration region of the basin shifted to the western edges in March 2012, as opposed to April in WY 2011. In April and May 2012, when the western edges of the basin were the main source of snowmelt, the PRISM snowmelt values were higher than those of TopoWx (Figure 4.9). The average PRISM snowmelt values over the MRB in April and May 2012 were 12% and 5.5% higher than the average TopoWx snowmelt values. This trend is similar to that for WY 2011 where the PRISM snowmelt values were higher in the months when the western edges of the basin were the major contributor to the generated snowmelt.

4.5. Summary and Conclusions

Macro-scale hydrologic models have been widely used to provide a holistic understanding of different hydrologic processes over large basins. In this study, we evaluated and compared the impacts of two high-resolution gridded temperature datasets (PRISM and TopoWx) on macro-scale snowmelt simulations in the MRB. A grid-based snow model was developed to simulate snowmelt based on the obtained temperature datasets. The snow model used a unique LEGO-fashion layout to account for the within-grid land use heterogeneity. Each grid was discretized into three RGB (Red, Green, and Blue) blocks, in which the Blue, Green, and Red Blocks respectively represent open water, forests and woods, and other land uses. In addition to the snowmelt generated on the ground, the model simulated snow interception and melt by forest canopies and rain-on-snow snowmelt to portray a more accurate picture of

snowmelt-related processes. Snowmelt simulations were compared with the SNODAS snowmelt data, which provided the closest estimates of snowmelt to the observations. The quantity and spatial distributions of snowmelt simulations from the two datasets were also compared to evaluate the impacts of using the two datasets for two representative WYs (i.e., 2011 wet/flood year and 2012 dry/drought year).

Comparing the simulated results with the SNODAS snowmelt data showed that both PRISM and TopoWx datasets resulted in comparable snowmelt simulations. The R^2 values for the simulated snowmelt using PRISM and TopoWx were 0.92 and 0.93, respectively. The discrepancy between the simulated results from the two datasets was small for low snowmelt; however, higher snowmelt values indicated higher discrepancy. Although the temperature distributions from the two datasets were similar for the majority of the basin, PRISM accounted for relatively higher temperatures than TopoWx for the western side of the MRB, characterized by high elevations and complex topography. The snowmelt results suggested that even small nuances in the quantity and distribution of temperatures between the two datasets led to notable changes in the simulated snowmelt. On March 17th, 2011, for example, the variations in the distributions of temperatures caused a 16.9% difference in the average simulated snowmelt over the MRB. The results highlighted that the discrepancies between the simulated snowmelt values using the two datasets were more pronounced in the western side of the MRB with complex topographical features. The snowmelt analysis for four selected months (i.e., February, March, April, and May) indicated that although both datasets captured the spatial and temporal patterns of snowmelt in the MRB, the quantities of the simulated snowmelt were different in the months when high snowmelt values were concentrated on the western edges of the basin.

4.6. References

Alcamo, J., Döll, P., Henrichs, T., Kaspar, F., Lehner, B., Rösch, T., and Siebert, S. (2003). "Development and testing of the WaterGAP 2 global model of water use and availability." *Hydrological Sciences Journal*, Taylor & Francis, 48(3), 317–337.

Anderson, E. (1968). “Development and testing of snow pack energy balance equations.” *Water Resources Research*, 4(1), 19–37.

Anderson, E. (2002). *Calibration of Conceptual Hydrologic Models for Use in River Forecasting*. National Oceanic and Atmospheric Administration, National Weather Service Hydrology Laboratory, Silver Spring, MD.

Anderson, E. (2006). *Snow accumulation and ablation model—SNOW-17*. National Oceanic and Atmospheric Administration, National Weather Service Hydrology Laboratory, Silver Spring, MD.

Badger, A. M., Livneh, B., Hoerling, M. P., and Eischeid, J. K. (2018). “Understanding the 2011 Upper Missouri River Basin floods in the context of a changing climate.” *Journal of Hydrology: Regional Studies*, Elsevier, 19, 110–123.

Behnke, R., Vavrus, S., Allstadt, A., Albright, T., Thogmartin, W. E., and Radeloff, V. C. (2016). “Evaluation of downscaled, gridded climate data for the conterminous United States.” *Ecological Applications*, John Wiley & Sons, Ltd, 26(5), 1338–1351.

Bergström, S. (1992). *The HBV model: Its structure and applications*. Swedish Meteorological and Hydrological Institute, Norrköping, Sweden.

Boryan, C., Yang, Z., Mueller, R., and Craig, M. (2011). “Monitoring US agriculture: the US Department of Agriculture, National Agricultural Statistics Service, Cropland Data Layer Program.” *Geocarto International*, Taylor & Francis , 26(5), 341–358.

Chu, X., Lin, Z., Tahmasebi Nasab, M., Zeng, L., Grimm, K., Bazrkar, M. H., Wang, N., Liu, X., Zhang, X., and Zheng, H. (2019). “Macro-scale grid-based and subbasin-based hydrologic modeling: joint simulation and cross-calibration.” *Journal of Hydroinformatics*, 21(1), 77–91.

Daly, C., Halbleib, M., Smith, J. I., Gibson, W. P., Doggett, M. K., Taylor, G. H., Curtis, J., and Pasteris, P. P. (2008). “Physiographically sensitive mapping of climatological

temperature and precipitation across the conterminous United States." *International Journal of Climatology*, John Wiley & Sons, Ltd, 28(15), 2031–2064.

Daly, C., Neilson, R. P., Phillips, D. L., Daly, C., Neilson, R. P., and Phillips, D. L. (1994). "A Statistical-Topographic Model for Mapping Climatological Precipitation over Mountainous Terrain." *Journal of Applied Meteorology*, 33(2), 140–158.

Debele, B., Srinivasan, R., and Gosain, A. K. (2010). "Comparison of Process-Based and Temperature-Index Snowmelt Modeling in SWAT." *Water Resources Management*, Springer Netherlands, 24(6), 1065–1088.

Fontaine, T. A., Cruickshank, T. S., Arnold, J. G., and Hotchkiss, R. H. (2002). "Development of a snowfall–snowmelt routine for mountainous terrain for the soil water assessment tool (SWAT)." *Journal of Hydrology*, Elsevier, 262(1–4), 209–223.

Hedstrom, N. R., and Pomeroy, J. W. (1998). "Measurements and modelling of snow interception in the boreal forest." *Hydrological Processes*, Wiley-Blackwell, 12(10–11), 1611–1625.

Jenks, G. (1967). "The Data Model Concept in Statistical Mapping." *International Yearbook of Cartography*, 7, 186–190.

Liang, X., Lettenmaier, D. P., Wood, E. F., and Burges, S. J. (1994). "A simple hydrologically based model of land surface water and energy fluxes for general circulation models." *Journal of Geophysical Research*, 99(D7), 14415.

Lindström, G., Pers, C., Rosberg, J., Strömqvist, J., and Arheimer, B. (2010). "Development and testing of the HYPE (Hydrological Predictions for the Environment) water quality model for different spatial scales." *Hydrology Research*, 41(3–4).

Liston, G. E., Elder, K., Liston, G. E., and Elder, K. (2006). "A Distributed Snow-Evolution Modeling System (SnowModel)." *Journal of Hydrometeorology*, 7(6), 1259–1276.

Livneh, B., Hoerling, M., Badger, A., and Eischeid, J. (2016). *Causes for hydrologic extremes in the upper Missouri River basin*. National Oceanic and Atmospheric Administration.

Martinec, J. (1960). "The degree-day factor for snowmelt runoff forecasting." *IUGG General Assembly of Helsinki, IAHS Commission of Surface Waters*, IAHS Wallingford, 51, 468–477.

Mehta, V. M., Knutson, C. L., Rosenberg, N. J., Olsen, J. R., Wall, N. A., Bernadt, T. K., Hayes, M. J., Mehta, V. M., Knutson, C. L., Rosenberg, N. J., Olsen, J. R., Wall, N. A., Bernadt, T. K., and Hayes, M. J. (2013). "Decadal Climate Information Needs of Stakeholders for Decision Support in Water and Agriculture Production Sectors: A Case Study in the Missouri River Basin." *Weather, Climate, and Society*, 5(1), 27–42.

Menne, M. J., Williams, C. N., Menne, M. J., and Jr., C. N. W. (2009). "Homogenization of Temperature Series via Pairwise Comparisons." *Journal of Climate*, 22(7), 1700–1717.

Mesinger, F., DiMego, G., Kalnay, E., Mitchell, K., Shafran, P. C., Ebisuzaki, W., Jović, D., Woollen, J., Rogers, E., Berbery, E. H., Ek, M. B., Fan, Y., Grumbine, R., Higgins, W., Li, H., Lin, Y., Manikin, G., Parrish, D., Shi, W., Mesinger, F., DiMego, G., Kalnay, E., Mitchell, K., Shafran, P. C., Ebisuzaki, W., Jović, D., Woollen, J., Rogers, E., Berbery, E. H., Ek, M. B., Fan, Y., Grumbine, R., Higgins, W., Li, H., Lin, Y., Manikin, G., Parrish, D., and Shi, W. (2006). "North American Regional Reanalysis." *Bulletin of the American Meteorological Society*, American Meteorological Society , 87(3), 343–360.

National Centers for Environmental Information. (2018). "Land-Based Station Data." <https://www.ncdc.noaa.gov/data-access/land-based-station-data> (Dec. 6, 2018).

National Operational Hydrologic Remote Sensing Center. (2004). "Snow Data Assimilation System (SNODAS) Data Products at NSIDC, Version 1." *National Snow and Ice Data Center*, <https://nsidc.org/data/G02158> (Jun. 20, 2019).

National Weather Service. (2012). *The Missouri/Souris River Floods of May-August 2011*.

Neitsch, S., Arnold, J., Kiniry, J., and Williams, J. (2011). *Soil and Water Assessment Tool (SWAT) theoretical documentation version 2009*. Texas Water Resources Institute, College Station, Texas.

Newman, A. J., Clark, M. P., Craig, J., Nijssen, B., Wood, A., Gutmann, E., Mizukami, N., Brekke, L., Arnold, J. R., Newman, A. J., Clark, M. P., Craig, J., Nijssen, B., Wood, A., Gutmann, E., Mizukami, N., Brekke, L., and Arnold, J. R. (2015). "Gridded Ensemble Precipitation and Temperature Estimates for the Contiguous United States." *Journal of Hydrometeorology*, 16(6), 2481–2500.

Norton, P. A., Anderson, M. T., and Stamm, J. F. (2014). *Trends in Annual, Seasonal, and Monthly Streamflow Characteristics at 227 Streamgages in the Missouri River Watershed, Water Years 1960–2011*.

Oyler, J. W., Ballantyne, A., Jencso, K., Sweet, M., and Running, S. W. (2015). "Creating a topoclimatic daily air temperature dataset for the conterminous United States using homogenized station data and remotely sensed land skin temperature." *International Journal of Climatology*, Wiley-Blackwell, 35(9), 2258–2279.

Pomeroy, J. W., Parviainen, J., Hedstrom, N., and Gray, D. M. (1998). "Coupled modelling of forest snow interception and sublimation." *Hydrological Processes*, Wiley-Blackwell, 12(15), 2317–2337.

Qi, J., Li, S., Jamieson, R., Hebb, D., Xing, Z., and Meng, F.-R. (2017). "Modifying SWAT with an energy balance module to simulate snowmelt for maritime regions." *Environmental Modelling & Software*, Elsevier, 93, 146–160.

Qiao, L., Pan, Z., Herrmann, R. B., and Hong, Y. (2014). "Hydrological Variability and Uncertainty of Lower Missouri River Basin Under Changing Climate." *JAWRA Journal of the American Water Resources Association*, John Wiley & Sons, Ltd (10.1111), 50(1), 246–260.

Rippey, B. R. (2015). "The U.S. drought of 2012." *Weather and Climate Extremes*, Elsevier, 10, 57–64.

Schmidt, R. A., and Gluns, D. R. (1991). “Snowfall interception on branches of three conifer species.” *Canadian Journal of Forest Research*, NRC Research Press Ottawa, Canada, 21(8), 1262–1269.

Stewart, I. T. (2009). “Changes in snowpack and snowmelt runoff for key mountain regions.” *Hydrological Processes*, John Wiley & Sons, Ltd, 23(1), 78–94.

Terink, W., Lutz, A. F., Simons, G. W. H., Immerzeel, W. W., and Droogers, P. (2015). “SPHY v2.0: Spatial Processes in HYdrology.” *Geoscientific Model Development*, 8(7), 2009–2034.

U.S. Army Corps of Engineers. (2012). *Post 2011 Flood Event Analysis of Missouri River Mainstem Flood Control Storage*. Omaha, Nebraska.

U.S. Bureau of Reclamation. (2016). *SECURE Water Act Section 9503(c)-Reclamation Climate Change and Water*. United States Bureau of Reclamation, Denver, Colorado.

U.S. Government Accountability Office. (2014). *Missouri River Flood and Drought*.

USGCRP. (2018). *Impacts, Risks, and Adaptation in the United States: The Fourth National Climate Assessment, Volume II*. (D. R. Reidmiller, C. W. Avery, D. R. Easterling, K. E. Kunkel, K. L. M. Lewis, T. K. Maycock, and B. C. Stewart, eds.), Washington, DC.

Walton, D., Hall, A., Walton, D., and Hall, A. (2018). “An Assessment of High-Resolution Gridded Temperature Datasets over California.” *Journal of Climate*, 31(10), 3789–3810.

Wan, Z. (2008). “New refinements and validation of the MODIS Land-Surface Temperature/Emissivity products.” *Remote Sensing of Environment*, Elsevier, 112(1), 59–74.

van der Wiel, K., Kapnick, S. B., Vecchi, G. A., Smith, J. A., Milly, P. C. D., Jia, L., Wiel, K. van der, Kapnick, S. B., Vecchi, G. A., Smith, J. A., Milly, P. C. D., and Jia, L. (2018). “100-Year Lower Mississippi Floods in a Global Climate Model: Characteristics and Future Changes.” *Journal of Hydrometeorology*, 19(10), 1547–1563.

World Meteorological Organization (WMO). (1986). *Intercomparison of models of snowmelt-runoff*. Operational Hydrology, Rep. 23, Geneva.

Xia, Y., Mitchell, K., Ek, M., Sheffield, J., Cosgrove, B., Wood, E., Luo, L., Alonge, C., Wei, H., Meng, J., Livneh, B., Lettenmaier, D., Koren, V., Duan, Q., Mo, K., Fan, Y., and Mocko, D. (2012). "Continental-scale water and energy flux analysis and validation for the North American Land Data Assimilation System project phase 2 (NLDAS-2): 1. Intercomparison and application of model products." *Journal of Geophysical Research: Atmospheres*, John Wiley & Sons, Ltd, 117(D3).

5. OVERALL SUMMARY AND CONCLUSIONS

The objectives of this research were to (1) improve the understanding of macro-scale hydrologic processes in cold climate regions, (2) improve macro-scale representation and modeling of depression-dominated regions, and (3) improve land use and land cover representation in macro-scale hydrologic models. To accomplish these specific objectives, a Macro-Scale Hydrologic Processes Simulator (Macro-HyProS), tailored for the cold climate conditions and depression-dominated areas; was developed and tested by coupling it with downscaled satellite-based meteorological datasets. Moreover, the impacts of micro-topography and spatiotemporal scales was investigated to facilitate the modeling of macro-scale hydrologic processes.

Chapter 1 reviewed the evolution of hydrologic modeling towards developments of the macro-scale hydrologic models and highlighted the current limitations of macro-scale hydrologic modeling. Specifically, it was outlined that neglecting the role of depressions and cold climate conditions in modeling can result in unrealistic hydrologic simulations.

Chapter 2 introduced the Macro-scale Hydrologic Processes Simulator (Macro-HyProS) with the primary objective of simulating hydrologic processes in cold climate regions and depression-dominated terrains. Macro-HyProS utilizes a LEGO-fashion horizontal layout for each grid to account for within-grid land use heterogeneity. Particularly, a set of RGB (Red, Green, and Blue) building blocks sit on top of a uniform LEGO plate, representing land use variations within a grid. In addition to its unique horizontal structure, Macro-HyProS accounts for five stratified vertical bands (i.e., Atmosphere, Vegetation, Snow, Surface, and Sub-surface Bands), responsible for simulating different hydrologic processes. The model uses improved methodologies that are specifically developed for macro-scale modeling depression-dominated cold climate regions. Eventually, a simple grid-to-grid routing method is used to compute the outlet discharge. The capabilities of the model in simulating different hydrologic processes were tested in the Red River of the North Basin (RRB), which is distinguished by its cold climate and

depression-dominated topography. The simulation results stipulated that RRB encounters frozen or partially frozen ground on an average of 40% of the year. The occurrence of the frozen ground condition was often synchronized with the early spring rainfall and snowmelt events and affected the magnitude and distribution of the generated surface runoff and infiltration. It was also shown that how the coinciding frozen ground, snowmelt events, and rainfalls in the critical period between late March and early April leads to streamflow discharge peaks. In addition, the results revealed that the depression-dominated areas within the RRB acted as surface runoff regulators, specifically in the periods when a high amount of surface runoff was generated (i.e., early Spring).

Chapter 3 assessed the impacts of sub-daily temperature fluctuations around the freezing temperature on the quantity and distribution of macro-scale snowmelt simulations. Specifically, the Macro-HyProS' macro-scale grid-based snow model was used to simulate the dynamics of snow accumulation and ablation processes. Unlike other macro-scale models that take advantage of only a single daily average temperature, the developed model takes into account sub-daily temperature fluctuations by considering minimum and maximum temperatures and their occurrence timing in a hybrid temperature index method (HTIM). The model was applied to the Missouri River Basin (MRB), and the HTIM simulation results were compared with the standard TIM as well as the snowmelt data from the National Oceanic and Atmospheric Administration (NOAA) SNOw Data Assimilation System (SNODAS). Results suggested that the HTIM can improve the physically-based representation of temperature variations in the snowmelt process. Particularly, it was found that although the average annual snowmelt results were not susceptible to the sub-daily temperature variations, monthly snowmelt values depend on the specific temperature variations in each month and the HTIM could yield either higher or lower snowmelt values.

Chapter 4 compared the impacts of two high-resolution gridded temperature datasets on macro-scale snowmelt simulations in the MRB. Temperature datasets from Parameter-elevation

Relationships on Independent Slopes Model (PRISM) and Topography Weather (TopoWx) were used to simulate snow accumulation and ablation processes for two representative wet and dry water years. The quantity and spatial distributions of snowmelt simulations were compared with the SNODAS snowmelt data. The results highlighted that although both PRISM and TopoWx datasets resulted in comparable snowmelt simulations with SNODAS, the discrepancy between the simulated results from the two datasets was larger for high snowmelt values. The spatially distributed results suggested that the discrepancies between the simulated snowmelt values using the two datasets were more pronounced in areas with complex topographical features.

Macro-HyProS paves the way for future research opportunities in depression-dominated cold climate regions. These opportunities lie within the current limitations of methods and availability of input data. The rapid developments in the availability of the satellite-based spatially distributed grid-based products, such as soil moisture maps and snow cover maps, lead the way for multi-variable calibration and validation of macro-scale hydrologic models. In other words, macro-scale hydrologic models can be calibrated and validated not only by using streamflow discharge but also by using other remotely sensed hydrologic processes and variables. In addition, advances in geographic information systems will allow faster and more efficient modeling of hydrologic processes at a macro scale. Therefore, the simplistic approaches in modeling can be replaced by processed-based approaches.

Overall, results and conclusions from this research accentuate the significance of commonly ignored hydrologic processes in depression-dominated areas and cold climate regions in macro-scale hydrologic modeling. The developed macro-scale model in this study (Macro-HyProS) takes a new modular approach in simulating hydrologic processes in different horizontal blocks and vertical bands. This modular approach facilitates the incorporation of other hydrologic processes into the model and provides the opportunity to improve the understanding of different hydrologic processes.